FONDAZIONE ISTITUTO ITALIANO DI TECNOLOGIA (IIT)
UNIVERSITA' DI GENOVA

Doctoral School on "Bioengineering and Robotics"
Curriculum: Bionanotechnology
XXXI Cycle

AFM-STED correlative nanoscopy provides a new view on the formation process of misfolded protein aggregates

Doctor of Philosophy (Ph.D.) Thesis

Ph.D. candidate:
Cosentino Michela

Tutor:
Dr. Claudio Canale
Department of Physics, University of Genova
Nanophysics, Istituto Italiano di Tecnologia

Supervisor:
Prof. Alberto Diaspro
Department of Physics, University of Genova
Nanophysics, Istituto Italiano di Tecnologia

"In loving memory
of my parents"

Contents

Contents 2

Abstract 5

List of Abbreviations 6

List of Tables 8

List of Figures 9

Summary 16

Chapter 1 17

Amyloid diseases 17

- 1.1 Protein folding and misfolding 19
- 1.2 Amyloid structure and aggregation process 21
- 1.3 Alzheimer's disease and related protein 24
  - 1.3.1 Amyloid β_{1-42} and Amyloid β_{1-40} 25
- 1.4 The generic nature of amyloid structure 27
- 1.5 Insulin fibrillogenesis 30
  - 1.5.1 The model system: bovine Insulin 30
  - 1.5.2 Insulin fibril formation 32
- 1.6 Amyloid aggregates and cytotoxicity .... **Error! Bookmark not defined.**

Chapter 2 38

Microscopy techniques 38

- 2.1 Confocal microscope 41
- 2.2 Super-resolution fluorescence techniques 42
  - 2.2.1 Stimulated Emission Depletion Microscopy (STED) 43
- 2.3 Scanning Probe Microscope – the blind microscope 45
  - 2.3.1 Atomic Force Microscopy (AFM) 46
- 2.4 Correlative Nanoscopy 51

2.4.1 AFM/STED techniques 52

Chapter 3 54

AFM/STED correlative on proteins aggregation 54

Materials and Methods 54

3.1 - Insulin labeling 54

3.2 – Labeled and unlabeled Insulin fibrillogenesis 55

3.3 – Fibrillogenesis of unlabeled and labeled A$\beta_{1\text{-}42}$ and A$\beta_{1\text{-}40}$ 56

3.4 – Immunolabeling analysis of A$\beta_{1\text{-}42}$ peptide 57

3.5 - Thioflavin T assay 58

3.6 - Light scattering. 58

3.7 - Atomic Force Microscopy measurements 59

3.8 - Stimulated Emission Depletion Microscope 60

3.9 - Correlative AFM/STED 60

Chapter 4 63

Characterization of misfolded protein aggregates by AFM/STED correlative microscopy 63

4.1 Amyloid fibrils from Insulin 63

4.1.1 – Insulin fibrillation Kinetics 65

4.1.2 – AFM characterization of *label-free* Insulin aggregates 66

4.1.3 - AFM characterization of ATTO 488-Insulin aggregates 68

4.1.4 - AFM/STED on Insulin aggregates 72

4.2 - Characterization of Aβ aggregation 76

4.2.1 – Aβ fibrillation Kinetics 77

4.2.2 - AFM characterization of A$\beta_{1\text{-}42}$ and A$\beta_{1\text{-}40}$ fibrillar aggregates 77

4.2.3 - AFM/STED on A$\beta_{1\text{-}42}$ and A$\beta_{1\text{-}40}$ aggregates 79

4.2.4 - Characterization of immunolabeled A$\beta_{1\text{-}42}$ aggregates 81

4.3 - Discussion 82

Chapter 5 86

Interaction between plasma membrane and amyloid protein 86

5.1 - Plasma membrane and membrane model 86

5.2 – Amyloid cytotoxicity .... **Error! Bookmark not defined.**

5.3 – Alpha-synuclein: structure, functions, and interactions 88

5.4 - Materials and Methods 90

5.4.1 - SLB preparation 90

5.4.2 - Peptide preparation 92

5.4.3 – AFM on Supported Lipid Bilayer 92

5.4 - Results 93

Chapter 6 98

General Conclusions 98

References 100

Abstract

The main part of my PhD work focused on the application of an advanced integrated technique, based on the coupling of an atomic force microscope (AFM) and a stimulated emission depletion (STED) microscope in the study of amyloid fibrils formation. This coupled system allows the acquisition of super-resolution fluorescence images, perfectly overlapped with AFM topography. Exploiting the extended capability offered by this technique, I highlighted some important features on the mechanisms followed by the labeled and unlabeled proteins through their aggregation pathway. The results demonstrates that labeled molecules are involved only in selected pathways of aggregation, among the multiple that are present in the aggregation reaction.

In a second part of my work, I investigated the process of interaction between Alpha-synuclein (α-Syn), the pathological peptide associated to the Parkinson's disease, and model lipid membranes. The aim of this study was to identify molecular mechanisms that are indicated as the base of neurodegeneration, not only in Parkinson's disease, but also in a large class of disorders, indicated as protein misfolding diseases.

List of Abbreviations

α-Syn	Alfa-synuclein
Aβ	Amyloid β
AD	Alzheimer's disease
AFM	Atomic Force Microscopy
APP	Amyloid Precursor Protein
BALM	Binding-activated Localization Microscopy
BSA	Bovine serum albumin
Chol	Cholesterol
CW	Continuous wave
DLS	Dynamic Light Scattering
DMSO	Dimethylsulfoxide
DOPC	1,2-dioleoyl-sn-glycero-phosphocholine
DOPE	1,2-diolyeil-phosphatidylethanolamine
EM	Electron Microscope
ER	Endoplasmic Reticulum
FD	Force-Distance
FLIM	Fluorescence Lifetime Imaging
GM1	Monosialotetrahexosylgangliosde
HCl	Hydrochloric acid
HFIP	Hexafluoroisopropanol
LBD	Lewy body diseases
LUV	Large Unilamellar Vesicle
$MgCl_2$	Magnesium chloride
NA	Numerical Aperture
NFT	Neurofibrillary Tangles
NMR	Nuclear Magnetic Resonance
PALM	Photoactivation Localization Microscopy
PC	Phosphatidylcholine
PD	Parkinson disease
PE	Phosphatidylethanolamine
POPS	1-palmitoyl-2-oleoyl-SN-glycero-3-phospho-L-serine
RESOLFT	Reversible Saturated Optical Fluorescence transitions
r.h.	Relative Humidity
RT	Room Temperature
SANS	Small-angle Neutron Scattering
SIM	Structured illumination microscopy
SLB	Supported Lipid Bilayer
SM	Sphingomyelin
SPM	Scanning Probe Microscopy
SR	Super-resolution
STED	Stimulated Emission Depletion
STEM	Scanning Electron Microscopy
STM	Scanning Tunnelling Microscope

STORM	Stochastic Optical Reconstruction Microscopy
TEM	Transmission Electron Microscopy
ThT	Thioflavin T

List of Tables

Table 1.1 | A summary of the main Amyloid diseases and components of their associated fibrillary deposits. (Data from ref. [4])

Table 1.2 | Proteins unrelated to diseases that form amyloid fibrils in vitro (Ref. from [8], data updated at 2003).

Table 2.1 | Comparison of high-resolution imaging techniques in molecular and cell biology. Data from Ref. [186].

Table 4.1 | The ratio of co-localization calculated for the different peptide species and dye to protein ratios.

List of Figures

Figure 1.1 - Regulation pathways of protein folding in the ER. The synthesized proteins, by ribosome, are translocated into the ER, where, with the help of a series of molecular chaperones and folding catalysts (not shown), they fold into their three-dimensional structures. Correctly folded proteins are then transported to the Golgi complex and then delivered to the extracellular environment. However, the incorrectly folded proteins in which they are ubiquitinated and then degraded in the cytoplasm by proteasomes follow another pathway, the unfolded protein response. Modified from *ref.* [9].

Figure 1.2 - (a) X-ray fibril diffraction pattern of insulin fibrils and (b) EM (from *ref.* [32]). (c) AFM image of insulin fibrils desiccated on mica. Scale bar: 200 nm.

Figure 1.3 - Schematic representation of the amyloid aggregation process.

Figure 1.4 - The amyloidogenic and non-amyloidogenic processing of APP. Image from *ref.* [89].

Figure 1.5 - Structure of Insulin. Upper line: From left to right: the monomeric hormone (A and B chains) forms dimers via anti-parallel association of B chain α-helices and C-terminal β-strands; assembly of three dimers to form hexamer. Images from *RCSB Protein Data Bank (PDB) 2ZP6*. Bottom line: primary structure of monomeric human insulin.

Figure 1.6 - Model for nucleus formation and growth from insulin protein in acidic environment (a) Prior to nucleus formation, ‘‘elongation’’ dominates; after nucleus formation, ‘broadening’’ occurs (from *ref.* [130]). (b) (Right) View of fibril model, looking down fibril axis. One layer of fibril model is made by stretching both monomers of native insulin (left) in a horizontal direction converting the deep blue helix of the B chain and the deep red helix of the A chain into extended β-strands. The spine of the fibril consists of a dry steric zipper formed by the mating of the central two strands from the B-chains of the two insulin molecules, plus two outer strands from the A-chains of the two molecules (from *ref.* [280]). (c) Surface representation of 3D maps of the four insulin fibril structures. (From left

to right) Structure of the fibril with a pair of protofilaments twisting around each other. The four-protofilament compact fibril. The six-protofilament fibril. The twisted ribbon. The protofilaments are well resolved in the first three structures, but are less clear in the twisted ribbon (from *ref.* [36]).

Figure 2.1 - Simplified Jablonski energy diagram representing fluorescence. The purple arrow represents the absorption of light. The red arrow represents vibrational relaxation from singlet-excited state, S_2 to S_1. This process is a non-radiative relaxation in which the excitation energy is dispersed as vibrations or heat to the solvent and no photon is emitted. The green arrow represents fluorescence to the singlet ground state, S_o. (Image from *Wikimedia Commons*)

Figure 2.2 - Schematic configuration of laser scanning confocal microscope optical setup. The light coming from the laser passes an (excitation) pinhole, and a dichroic mirror rejects it and focused by a microscope objective to a small spot on the sample. A dichroic mirror reflects one wavelength while transmits the others All the light originating from the in-focus plane will pass freely through the pinhole, whereas the pinhole will mainly block light arising from an out-of-focus plane. (Image from *http://zeiss-campus.magnet.fsu.edu*).

Figure 2.3 - (a) Conventional confocal microscopy compared with Stimulated Emission Depletion (STED) nanoscopy. It uses (in addition to a fluorescence excitation laser) a second, ring-shaped laser to quench fluorescence. (b) Schematic configuration of STED system. (Image from *http://zeiss-campus.magnet.fsu.edu*).

Figure 2.4 - (a) Schematic representation of a Scanning Probe Microscope. b) Different acquisition modes, with (constant signal) or without (constant height) Z-feedback loop.

Figure 2.5 - (a) Lennard-Jones potential (red curve), describes interactions between atoms depending on their distance, d. It results from the sum of two contributions, related to attractive and repulsive interactions (Image from *http://www.uni-leipzig.de*). (b) Simplified scheme of AFM photo-detection system (optical path elements are not shown). Cantilever deflection results in a shift in laser spot position on PSPD. AFM main signal (vertical deflection) is calculated from (A+B)-(C+D), while frictional torsion (lateral deflection) is (A+C)-(B+D).

Figure 2.6 - AFM imaging modes (modified from *ref.* [279])

Figure 2.7 - Schematic representation of a force vs distance curve.

Figure 2.8 - AFM/STED Schematic representation. The confocal and STED images are acquired in reflection, while the AFM probe is reaching the sample from above, providing a 3D topographical view at high resolution.

Figure 3.1 - Schematic representation of Insulin Labeling procedure. In Step 1 labeling of insulin. The following step are: Step 2, purification; step 3, quantification; step 4, final solution of labeled and unlabeled insulin in three dye-to-protein ratio; step 5, fibrillation process.

Figure 3.2 - Molecular structure of dimeric insulin at pH 2.0. (a) Ribbon structure showing the secondary structural motifs, and (b) space filled representation of the same dimer. The length and diameter of the cylinder was estimated to be 42 and 22 Å, respectively[193]. (Image from *ref.* [130])

Figure 3.3 - (a) JPK Nanowizard III with Zeiss inverted optical microscope. (b) Motorized stage with sample holder. (c) Cantilever holder. (d) Description of JPK Nanowizard III. Images modified from *http://www.jpk.com*.

Figure 3.4 - AFM cantilever. (a) Rectangular silicon cantilever for intermittent contact imaging in air. (b) Silicon tip of cantilever in a. (c) Triangular silicon nitride cantilevers for imaging in liquid. (d) Silicon nitride tip of cantilever in c.

Figure 3.5 - Correlative AFM/STED setup (a). NanoWizard II AFM stage and head in the inset. (b) Images of the same area can be acquired in different modes. The excitation and depletion lasers arrive from below (inverted optical microscope). The confocal and STED images are acquired in fluorescence, while the AFM probe is reaching the sample from above, providing a 3D topographical view at high resolution.

Figure 3.6 - Direct overlay procedure. Panel a shows the total overlay procedure. In the first row of this panel, we show a cartoon of the collected optical image with inherent aberrations, AFM and the corrected image (Image modified from *ref.* [191]). Second row depicts the direct overlay software, which calibrates the pictures and makes a grid automatically. The panel b shows the reflection images

made on a 30 µm x 30 µm of optical field of view by moving the tip in 25 µm x25 µm regions in order to calibrate this area using 9 points, as shown.

Figure 3.7 - Insulin fibril 1:19 dye-to-protein ratio. AFM (a), Confocal (b) and STED (c) were analysed by using the Colocalization function by ImageJ (NIH, Bethesda, MD, USA). The ratio of colocalization is the ratio between the number of colocalized pixels (white pixels in d and e) and the total number of pixel that composed the fibrils in the AFM images.

Figure 4.1 - Thioflavin T kinetic. Time course aggregation of a 50 µM solution of insulin at 60 °C, monitored by ThT fluorescence increase (ThT 100 µM). Emission wavelength: range 470-540 nm; excitation wavelength: 450 nm; slit width: 1nm. Aliquots of 50 µL of solution were taken away at different time processes. The points indicate the aliquots extracted in time and the corresponding ThT normalized value.

Figure 4.2 - AFM images of unlabeled insulin aggregated species sampled at different instant of kinetic and desiccated on mica. a: t= 0; b: t= 3 days; c: 4 days; d: t = 6 days; e: t= 12 days f: t= 14 days. Scale bars a-f: 2 µm. Z-range 7 nm (a, b, c), 15nm (d, e, f).

Figure 4.3 - AFM image of mature insulin fibrils. (a) Overview of preformed insulin in water diluted 100 times (scale bar: 500 nm). (b) Details of structure (scale bar: 200 nm) and (c) relative profile. (Z-range: 15 nm).

Figure 4.4 - ATTO 488-Insulin 1:19 dye-to-protein ratio aggregated by AFM. The images sampled at different instant of kinetic: (a) 0 day, (b) 6 days, (c) 12 days (d) 14 days. Scale bar: 2 µm. Z-range: 7 nm (a, b), 15 nm (c, d).

Figure 4.5 - Insulin aggregation in three dye-to-protein ratios. AFM images performed after 10 days incubation in denaturing conditions. (a) 1:19, (b) 1:99, (c) 1:499. Scale bar: 1 µm. Z-range: 10 nm.

Figure 4.6 - AFM image of mature insulin fibrils labeled 1:19. (a) Overview of preformed insulin in water diluted 100 times (scale bar: 1 µm). (b) Details of structure (scale bar: 200 nm) and (c) relative profile. (Z-range: 10 nm).

Figure 4.7 - The lateral broadening effect led by the tip size. (a) AFM image in dry condition of insulin fibrils structure (Scale bar: 100 nm. Z-range: 10 nm). (b)

The profile cross-section indicate a height of 4 nm and a length of 30 nm. (c) Schematization of broadening effect in AFM image due to tip size effect.

Figure 4.8 - Correlative technique on amyloid fibrils from bovine insulin in 1:19 dye-to-protein ratio. The STED and Confocal images are overlaid with AFM topography. Scale bar: 1 µm.

Figure 4.9 - ATTO 488-Insulin fibrils 1:19 images. AFM (a, c), STED microscopy (b, d) and the correlative images obtained by c and d (e). The ratio of colocalization in this particular field of view is indicated by the histogram (inset e). Scale bars: (a, b) 5 µm, (c-e) 2 µm. Z-range: (a, c) 5 nm.

Figure 4.10 - Detail of insulin 1:19 fibrils in AFM (a), STED (b), Confocal (c). (d) AFM profile comparison of the same fibril displayed a not continuous distribution of fluorophore. Optical microscope scale bar 2 µm.

Figure 4.11 - Insulin fibrils obtained from 1:99 (a-c), and 1:499 (d-f) dye-to-protein ratio. AFM images (a, d), STED microscopy images (b, e) and correlative images obtained by the previous (c, f). Several fibrils are totally unlabeled. This result resembles the one obtained at a dye to protein ratio of 1:19. The ratio of colocalization is shown by the blue bar in the inset histograms. Scale bar: 1 µm. Z-range: (a, d) 10 nm.

Figure 4.12 - ThT fluorescence intensity kinetics of Aβ. Time course aggregation of a 25 µM solution of $Aβ_{1-40}$ (a) and $Aβ_{1-42}$ (b), monitored by ThT fluorescence increase (ThT concentration was 50 µM). Emission wavelength: 482 nm; excitation wavelength: 450 nm; slit width: 1nm.

Figure 4.13 - AFM images of amyloid-β peptides just after resuspension of the lyophilized peptide in the aggregation medium. $Aβ_{1-42}$ (a) unlabeled, (b) 1:19, (c) 1:99, (d) 1:499. $Aβ_{1-40}$ (e) unlabeled and (f) 1:19. Scale bar: 1 µm. Z-range: 10 nm. Insets scale bar: 200 nm. Prefibrillar aggregates are not present at the beginning of the aggregation process.

Figure 4.14 - Amyloid β fibrils. AFM was used to follow the aggregation of $Aβ_{1-42}$ and to characterize the morphology of the fibrils. (a) Unlabeled, (b) 1:19, (c) 1:99, (d) 1:499. $Aβ_{1-40}$ (e) unlabeled and (f) 1:19. Scale bar: 1 µm. Z-range: (a) 10 nm, (b, c, d, e, f) 20nm.

Figure 4.15 - Amyloid aggregates from HF488 Aβ_{1-42}. Different concentrations of fluorescent peptides were present. The dye to protein ratios are (a-c) 1:19, (d-f) 1:99, (g-l) 1:499. Also at the higher dye-to-protein ratio (a-c) some fibrils were not displayed by fluorescence images (e.g., see the withe arrows). Scale bar 2 µm. Z-Range (a, g) 10 nm, (d) 5 nm. Overlay graph on the right.

Figure 4.16 - AFM/STED on HF488 Aβ_{1-40} aggregates. Fibril imaged by AFM (a) and STED (b). The overlapped image (c) in which the green color represent STED fibrils, red color AFM fibrils and in white color the ratio of co-localization. The dye to protein ratio is 1:19. Scale bar 2 µm. Z-Range (a) 10 nm.

Figure 4.17 - Amyloid aggregates formed from Aβ_{1-42} in the absence of fluorescent monomers and subsequently labeled via indirect immunolabeling. All the features displayed in the AFM images (a, d) are also visible in the STED images (b, e) and are colocalized (c, f). Interestingly, the fibrils size, measured by AFM, is larger with respect to the unlabeled fibrils, confirming the presence of a large amount of antibody on the fibrillar aggregates. Scale bar (a-c) 2 µm, (d-f) 1 µm. Z-range (a, b) 30 nm. Inset (f) graph of colocalization.

Figure 4.18 - A stochastic aggregation of the labeled/unlabeled peptides should bring to the formation of uniformly labeled fibrils. Our experiments indicate a different scenario where just a fraction of the fibrils has a labeled component. Other fibrils, dark in the STED analysis, are unlabeled. These two products are the results of different aggregation pathways. The correlative technique here employed gives an answer to the above question.

Figure 5.1 - Schematic representation of plasma membrane.

Figure 5.2 - Phase separation in a supported lipid bilayer containing DOPC, Sphingomyelin (SM), Cholesterol and GM1 imaged using AFM. (a) Typical morphology. Scale bar: 1 µm. (b) Cross section was taken along the white line in a (X-axis). The difference in height between the two phases is ~ 2.2 nm. Images and plot profile from *Oropesa et al.*[78]. (c) Particular view of lipid l_α and l_o domains. Scale bar: 200 nm

Figure 5.3 - Electron microscopy image of prefibrillar aggregates. The images refer to the α-syn mutant (A53T) aggregation, involved in Parkinson's

disease. In the first stage of aggregation the protein shows a characteristic pore-like structure[290]. The images show an area of 30.5x30.5 nm.

Figure 5.4 - Primary and secondary structure of α-syn. To right shows the three main domains of α-syn. The N-terminal is an amphipathic domain that contains the three point mutations (white bars) linked to the autosomal dominant form of PD. The central region is a highly hydrophobic domain that was originally identified in patients with AD or LBD, which is the precursor of the non-amyloidogenic component of the extracellular senile plaque (NAC), which promotes the protein aggregation. The C-terminal domain has an acidic character, which possesses anti-amyloidogenic properties.

Figure 5.5 - Schematic representation of the vesicle fusion protocol employed in this work.

Figure 5.6 - Difference in thickness between outer (a) and inner (b) leaflet.

Figure 5.7 - AFM images of SLB sampled before (a-c) and after administration of α-syn aggregates solutions (d-f). After 10 min incubation, α-syn induce destabilization on the defected-free bilayer. Scale bar 2 µm (a, d), 500 nm (b, e) and 200 nm (c, f). Z-range 10nm.

Figure 5.8 - The neural inner plasmatic model membrane (DOPC/DOPE/SM/POPS/ch) by AFM. The profile section (with the dark line) below the image shows the roughness in the initial stage of the scan session. Scale bar 1 µm (a, b), 500 nm (c). Z-range 6 nm (a, b), 10 nm (c).

Figure 5.9 - AFM Images of α-syn interaction with DOPC/DOPE/SM/POPS/ch bilayer. After 10 min incubation time oligomers peptide induced removal of bilayer parts and consequent holes formation. (a) 20 nM and (b) 70 nM concentration of α-syn deposited. The black line indicates a profile section (showed below). Scale bar 1 µm. Z-range 10 nm.

Summary

The main aim of my PhD was to apply a new and original approach in the study of misfolded protein aggregation, a phenomenon related to several diseases (e.g., Alzheimer's and Parkinson's diseases). In particular, I investigated the morphological properties of amyloid fibrils derived by a mixture of labeled and unlabeled peptides by applying an advanced integrated system obtained from the coupling of a standard atomic force microscope (AFM) and a super-resolution optical microscope. This approach is new in the field of misfolded protein aggregation.

In the first chapter of this thesis, I introduce amyloid proteins and related diseases, i.e. amyloidosis. Chapter 2 gives an overview on the microscopy techniques employed (super-resolution fluorescence microscopy and Atomic Force Microscopy, AFM).

In Chapter 3, the different experimental approaches and methods employed in this thesis are reported. A focus on the results obtained by means of correlative AFM-STED microscopy on the aggregation of insulin and two isoform od Amyloid-β peptides have been reported in Chapter 4.

In parallel I carried out a second activity aims to define the molecular mechanism at the base of the interaction between a pathological petide, α-Syn, and lipid membranes. In particular, since α-Syn is present in both the cytosolic and the extracellular environment, I examined the interaction between this peptide and artificial lipid membranes that mimic the composition of both the internal and the external leaflets of the cell membrane. In Chapter 5, I present results related, obtained by AFM technique, investigating the process of interaction between α-syn and solid supported lipid membranes.

Chapter 1
Amyloid diseases

A wide range of human diseases, including Alzheimer's and Parkinson's disease, Spongiform Encephalopathies, systemic amyloidosis and type II diabetes is characterised by uncorrected self-assembly and deposition of proteins material commonly called amyloid fibrils[1,2]. In each of these disease states, peptide passes from its soluble and functional form into an insoluble fibrillar species that deposited and accumulated in the body tissue, displaying a specific tinctorial affinity for Congo red and Thioflavin T (ThT)[3]. These peculiar chemical identities of the amyloid fibril-forming protein allowed the clinical classification of the amyloidosis; some human amyloid-related disorders have been reported in *Table 1.1*[4].

The term amyloid was employed by the German physician scientist Rudolph Virchow in 1854 to describe the cerebral corpora amylacea stained with iodine-sulfuric acid[5]. It was originally thought that amyloid was cellulose by nature (from the old Greek amylon=starch). However, it was Friedreich and Kekulé who dissected the amyloid-rich segments from the spleen of a patient with amyloidosis. In contrast to Virchow, they performed direct chemical analysis of the material extracted and reached the definitive conclusion that the main substance was protein[6].

During the 19th and early 20th centuries, investigations on the nature of amyloid evolved from the macroscopic observations of the tissues to the study of amyloid structure. The availability of light microscope technology and histopathologic dyes (ThT and Congo red) highly specific, led on to conclude that amyloid was structurally amorphous[7]. Cohen and Calkins in 1959 started electron microscopic studies of diverse origins, humans and animals, amyloid tissues demonstrating that amyloid deposits exhibit a similar fibrillar submicroscopic structure[8].

Table 1.1 | A summary of the main Amyloid diseases and components of their associated fibrillary deposits. (Data from ref. [4])

clinical syndrome	fibril component
Alzheimer's disease	Aβ peptides (wild-type or mutant); Tau (wild-type or mutant)
spongiform encephalopathies	prion protein (full-length or fragments)
Parkinson's disease	α-synuclein (wild type or mutant)
fronto-temporal dementia	Tau (wild type or mutant)
amyotrophic lateral sclerosis	superoxide dismutase (wild type or mutant)
Huntington disease	huntingtin (polyQ expansion)
cerebellar ataxias	ataxins (polyQ expansion)
Spinocerebellar ataxia 17	TATA-boxbinding protein (polyQ expansion)
dentatorubro-pallido-luysian atrophy	atrophin 1 (polyQ expansion)
Kennedy disease	androgen receptor (polyQ expansion)
familial British dementia	ABri peptide
familial Danish dementia	ADan peptide
primary systemic amyloidosis	Ig light chains (full-length or fragments)
secondary systemic amyloidosis	serum amyloid A (fragments)
familial Mediterranean fever	serum amyloid A (fragments)
familial amyloid polyneuropathy (FAP)	transthyretin (over 45 variants or fragments
familial amyloid polyneuropathy (FAP)	thereof)
senile systemic amyloidosis	transthyretin (wild type or fragments thereof)
Finnish hereditary systemic amyloidosis	gelsolin (fragments of the mutant protein)
hemodialysis-related amyloidosis (DRA)	β2-microglobulin
familial non-neuropathic systemic amyloidosis	lysozyme (mutant)
type II diabetes	pro-islet amyloid polypeptide (fragments)
hereditary cerebral haemorrhage with amyloidosis	cystatin-C (minus a 10-residue fragment); Aβ peptides
Inclusion-body myositis (IBM)	Aβ peptide
Injection-localized amyloidosis	Insulin

Today, amyloid is known to have the same core structure, a network of polymeric unbranched fibrils resulting from ordered polymerization of specific proteins[9].

The diseases characterized by the formation and deposition of amyloid fibrils, are generally defined as protein misfolding diseases, that include some of the more well-known neurodegenerative pathologies, such as Alzheimer's and Parkinson's diseases. In this context are included also nonneuropathic localized amyloidosis, relates to a group of diseases where aggregation occurs in a single type of tissue other than the brain and nonneuropathic systemic amyloidosis relates to diseases in which aggregation occurs in multiple tissues.

Some of these conditions, such as Alzheimer and Parkinson's diseases, are predominantly sporadic, although hereditary forms are well documented. Other conditions can arise from specific mutations and are hereditary, e.g. the lysozyme and fibrinogen amyloidosis. In addition, the 85% of the amyloid diseases are sporadic amyloidosis, and the 10% a hereditary forms, while the 5% can also be transmissible in humans, as well as in other mammals, defined spongiform encephalopathies[10].

1.1 Protein folding and misfolding

The proteins, synthesized on ribosomes as linear chains of amino acids in a specific order following the DNA information encoded, attain own specific function through the folding process[11]. The folding path is the way in which the random coiled proteins reach the native structure in the conformational space which is characteristic for each biological molecules[2]. This polypeptide self-organization is a crucial event occurred after or during the translational process in the cytoplasm or specific compartments, such as mitochondria or the endoplasmic reticulum (ER) of the cells[12]. In the last 50 years, many theoretical and experimental works have been combined to explain protein folding dynamics, defining the so-called 'from sequence to folding structure' dogma[13]. How this process occurs is one of the most complicated and fascinating problems in the study of molecular biology: passing from the Levinthal's paradox (the apparent contradiction between the number of possible conformations and the actual rapidity by which the protein chain assume its stable conformation - less than a second), to a new 'folding funnel' view, in which only a small number, energetically favorable, of all possible conformations, need to be sampled during its transition[14–17]. The code for the folding process of a random polymer into these well-defined structures is overall contained within the sequence of amino acids in a polypeptide chain (primary structure)[18]. The primary stabilizations, that are achieved in nearly every native protein, are the 'secondary' structure, i.e. the beta turns and omega loops along with helices and the sheets, obtained by means of the hydrogen bonding between the amide and carbonyl groups of the main chain and several other non-covalent interactions, electrostatic interactions, Van der Waals forces, and hydrophobic interactions.

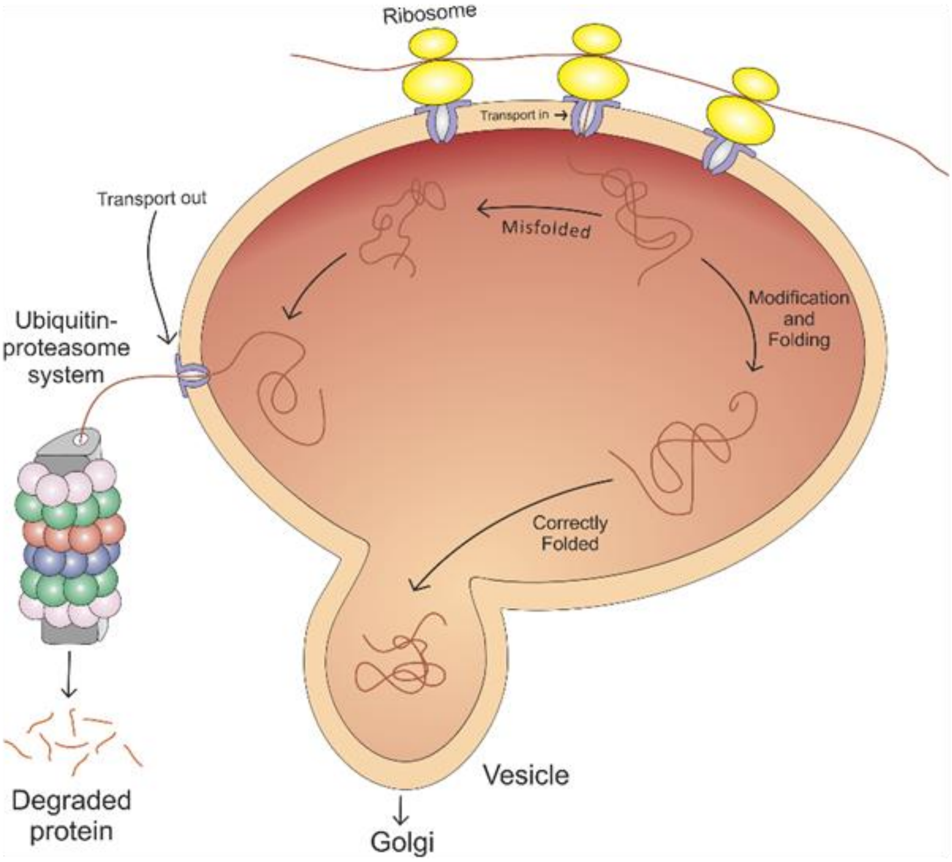
Ribosome
Transport in →
Transport out
Misfolded
Modification and Folding
Ubiquitin-proteasome system
Correctly Folded
Vesicle
Degraded protein
Golgi

Figure 2.1 | Regulation pathways of protein folding in the ER. The synthesized proteins, by ribosome, are translocated into the ER, where, with the help of a series of molecular chaperones and folding catalysts (not shown), they fold into their three-dimensional structures. Correctly folded proteins are then transported to the Golgi complex and then delivered to the extracellular environment. However, the incorrectly folded proteins in which they are ubiquitinated and then degraded in the cytoplasm by proteasomes follow another pathway, the unfolded protein response. Modified from ref. [9].

The relationship between the sequence and the fold in polypeptides and the rapidity in which the folding process enables the correct structure to be found for any given sequence represents a clear example of biological complexity, the 'protein-folding problem'[19]. Inside this regards, the cells exhibit a complex regulatory system to promote a biological functional conformation for the proteins[20] (*Figure 1.1*). The molecular machinery complex consists of molecular chaperones, to favor folding of polypeptide chains (both in the cytosol and in the endoplasmic reticulum) and the ubiquitin-proteasome pathway, to promote their degradation when the three-dimensional correct structure is not achieved[21]. However, despite the incredible organization of cells and intrinsic ability of evolved protein sequences to avoid unfolding/misfolding nevertheless occur, resulting in either to protein misfunction or to the accumulation of protein aggregates[22,23]. In a crowded cellular environment, surrounded by interacting proteins, nascent polypeptides face a formidable challenge in finding the correct interactions that result in a folded and functional protein. Such events can be associated with changing in environmental conditions, such as pH or temperature, misprocessing phenomena chemical modification, aberrant interactions with metal ions or moreover from specific mutations in the sequence[9,24]. However, several proteins become trapped in meta-stable intermediate structures which are usually recognised by proteasomal machinery and degraded or refolded by chaperones[25]. Alternatively, they can also misfold and self-associate leading to formation of either amorphous compounds or structures of elongated ordered morphology, known as amyloid fibrils. Most frequently it was found that this amyloid aggregation occur through the formation of multiple kinetic intermediates. In this scenario, it has been suggested that the generic amyloid state may constitute a deep and sharp energetic minimum representing the most stable state that multiprotein systems can adopt[2,26–28]. An accumulation of these fibrils can result in a range of human diseases commonly referred to as amyloidosis.

1.2 Amyloid structure and aggregation process

Regardless of the protein structure from which they originate, amyloid fibrils show many shared properties, including the peculiar structure, as determined in detail using experimental techniques. A typical cross-β super-secondary structure, in parallel or anti-parallel way, models the core structure of each filaments whose strands are perpendicular to fibril axis[29–31]. Cross-β structures results in a peculiar X-ray diffraction pattern where typical inter-sheets and inter-strand distances, are evident resulting respectively 11 Å and 4.8 Å [32,33] (*Figure 1.2 a*).

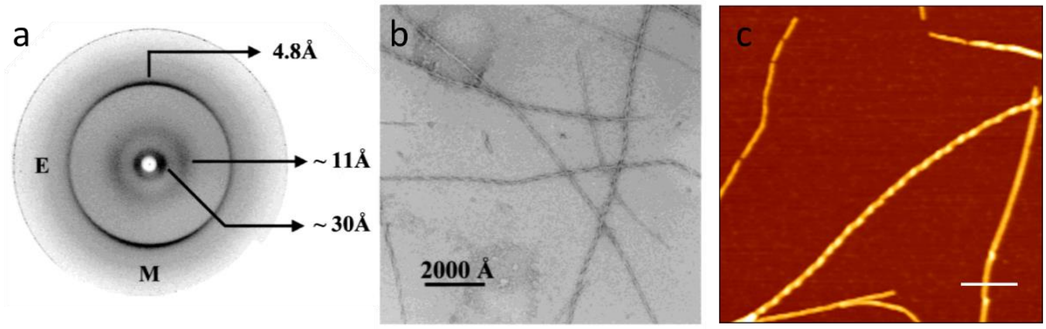

Figure 1.2 | (a) X-ray fibril diffraction pattern of insulin fibrils and (b) EM (from ref. [32]). (c) AFM image of insulin fibrils desiccated on mica. Scale bar: 200 nm.

The structure is made particularly stable by the presence of an highly organized non-covalently bonds originating from a protofilament backbone consisting of β-sheet conformation[27,34].

A typical fibril consists of two to seven proto-filaments, twisted around each other to form supercoiled rope-like structures , with an average diameter of 4–10 nm determined through AFM and electron microscopy (EM) measurements[35,36].

The fibril architecture of a number of peptides, including Amyloid β_{1-40} and Amyloid β_{1-42}, have been proposed using constraints obtained from solid-state NMR[37], and are also consistent with molecular dynamics simulations[38]. In addition, advances in micro-crystallographic techniques enabled the discovery of a high-resolution structure of a peptide extracted from N-terminal segments of Sup35 and many others species, reported by Eisenberg's group[39]. Their studies have confirmed that many peptides, which are unrelated by sequence, adopt the characteristic cross-β pattern in the fibril state. The spine of the amyloid fibril contains dry steric zippers structure formed from self-complementary[40] sequences suggesting a common structural features, shared by amyloid diseases, at the molecular level[8,41].

Real-time monitoring of fibril growth is made possible by highly specific probe, such as ThT, a commonly used dye to diagnose amyloid fibrils, both ex vivo and in vitro[42,43]. The benzothiazole dye ThT exhibits fluorescence quantum yield enhancement upon intercalation into the cross-β super-secondary structure because of the rotational immobilization of the central C–C bond connecting the benzothiazole and aniline rings[44–47]. Upon the binding, the dye changes its absorption/emission spectrum from 385 nm (free dye absorption) / 445 nm (free dye emission) to 450 nm / 482 nm[33,48,49]. Since fluorescence intensity variation, in first approximation, appears to depend on the presence of molecule in amyloid state and not on the interaction with monomeric or dimeric peptides, fluorescence signal at the new emission wavelength is a direct measurement of fibril formation.

The mechanism by which amyloid fibrils are formed seems to resemble the process of crystallization or ordered aggregation of proteins, i.e. a nucleation-polymerisation process, in which the amyloid growth proceeds through several steps[50,51] (*Figure 1.3*).

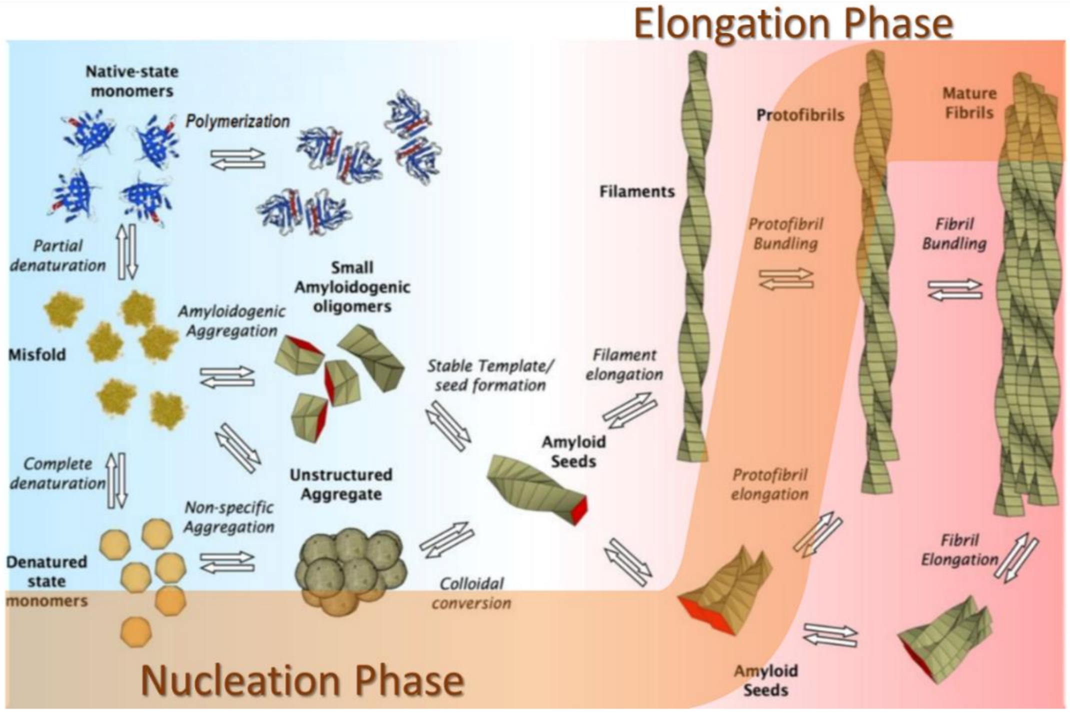
Elongation Phase
Native-state monomers
Polymerization
Partial denaturation
Misfold
Small Amyloidogenic oligomers
Amyloidogenic Aggregation
Complete denaturation
Non-specific Aggregation
Unstructured Aggregate
Denatured state monomers
Stable Template/ seed formation
Colloidal conversion
Amyloid Seeds
Filaments
Filament elongation
Protofibrils
Protofibril Bundling
Protofibril elongation
Mature Fibrils
Fibril Bundling
Fibril Elongation
Amyloid Seeds
Nucleation Phase

Figure 1.3 | Schematic representation of the amyloid aggregation process.

This mechanism has been proposed for many of the proteins responsible for amyloidosis, first of all the Alzheimer Aβ peptide and the prionic protein[52].

The input to follow this partially unfolding/refolding way come from destabilized native conformations[53] via mutations or denaturing conditions such as non-native pH values[54] and elevated temperatures[55]. In particular several studies indicate that during the microscopic processes, the intermolecular hydrophobic interactions display a significant role as the determinants of the formation rate of the misfolded monomers into different types of oligomers[56,57]. At the onset of the fibrillation process, early aggregates are distinguished as an oligomeric protein with a diameter of 2.5–5.0 nm, as confirmed by AFM studies[58]. The formation of amyloid fibrils is not the only pathogenic form of amyloid deposition; these species follow different possible pathways. They frequently associate with each other into bead-like chains or small annular rings, acting as precursors for the formation of extremely organized amyloids such as longer protofilaments and eventually generating mature fibrils. During the elongation step, the presence of fibrillar templates promotes the quick incorporation of amyloidogenic monomers, amyloid complete structure start forming, and the kinetics turns out to be fast[59]. This cooperative phase is followed by a plateau. Amyloid aggregates corresponding to each phase of the kinetics can be characterized using different techniques, including AFM[60].

1.3 Alzheimer’s disease and related protein

Alzheimer’s disease (AD) is the most frequent neurodegenerative disease and the most common cause of dementia in humans, with an estimated prevalence of one in nine people over age 65 and of more than one in three people over age 85[61]. Clinically, initial symptom of AD is impaired short-term memory that changes to profound memory failure and impairment of cognitive functions, consequently neuronal degeneration and death. Despite the remarkable improvements in understanding of the pathogenesis of the disease have been made over last several decades, the accurate mechanism of AD remains unclear. Nowadays the argument about a potential therapeutic strategy is still open[62].

AD neuropathology exhibits two hallmark features: senile plaques containing depositions of Amyloid β (Aβ) proteins and neurofibrillary tangles (NFT), deriving from hyperphosphorylation of microtubule-associated Tau proteins in neurons[63]. Since the discovery by psychiatrist and pathologist Alois Alzheimer in 1906, several theories have been formulated to explain the pathogenesis of AD[62,64]. The central hypothesis for the cause of AD is the failure of the protective degradative mechanism of the cells leading to the accumulation of toxic concentrations of Aβ, which aggregates, into plaques thus causing neuronal degeneration and consequently leading to dementia - the amyloid cascade hypothesis[65,66]. The high heterogeneity and polymorphisms of amyloid aggregates, lead different path of cytotoxicity resulting from several cellular mechanisms in which they are involved, specific for every aggregation state. For example it has been shown that, in the AD, the presence of $A\beta_{1\text{-}42}$ small oligomers impair long-term potentiation[67] and raise ER stress[68]; whereas the presence of the major fibrillar aggregates of the same protein is associated with the neuro-inflammatory response[66,69,70]. In addition, it is still widely debated that despite it seems to have a negligible role in the pathogenesis of amyloid-related neurodegenerative disorders, the presence of mature fibrillary aggregates can provocate some symptoms in systemic amyloidoses[71]. Although the direct causal link between Aβ and impaired neuronal function and memory is still under elucidation, several studies indicate that cell dysfunction is derived from the ability of small aggregates to interact with the cellular membranes, leading to loss of membrane integrity and ultimately to cell death[72–74]. Oligomers interact with plasma membrane[75,51] affecting important biophysical properties, such as microviscosity, molecular order, membrane potential and permeability. Membrane lipid composition, especially with respect to the content of cholesterol and anionic lipids, plays a fundamental role in determining the nature of Aβ/membrane interaction[76–79]. The neurologically disruptive nature of Aβ prefibrillar oligomers has been established in various studies conducted on Alzheimer's[80–82], Parkinson's[73,83] , and Huntington's[84], which can induce oxidative stress, apoptosis, and abnormal calcium homeostasis in neurons. On the contrary, mature fibrils appear to be harmless.

A deep understanding and visualization of the involved molecular mechanisms could lead to new strategies for the treatment of this widespread pathology.

1.3.1 Amyloid $\beta_{1\text{-}42}$ and Amyloid $\beta_{1\text{-}40}$

Aβ peptides are involved in AD as the main component of the amyloid plaques found in the brains of Alzheimer patients. Aβ aggregates originate from an integral membrane glycoprotein, the Amyloid Precursor Protein (APP). This ubiquitous protein is located in plasma membrane, as well as in endoplasmic reticulum, Golgi apparatus, and mitochondria. APP can be metabolized following two different pathways[85,86] (*Figure 1.4*): the secretory pathway and the amyloidogenic pathway. In the former, occurring more frequently, APP may be cleaved between residue 16-17 of the Aβ domain[87]. The event, called α-secretase cleavage, operates in cholesterol poor membrane regions and precludes Aβ formation. The soluble α-secretase cleaved APP (α-sAPP) is secreted and the C-terminal fragment (C83) is processed by γ-secretase, resulting in a not amyloidogenic soluble 3-kDa peptide (p3). In the amyloidogenic pathway, The Aβ fragment is generated beginning with an initial APP cleavage at amino acid residue 672 to define the N-terminus of Aβ[88]. The cleavage is referred to as β-secretase cleavage, which is located in cholesterol rich membrane domains, and results in the secretion of the soluble β-secretase cleaved APP ectodomain (β-sAPP) from neurons and transfected cells. The remaining C-terminal fragment containing the transmembrane and cytoplasmic domains (C99).

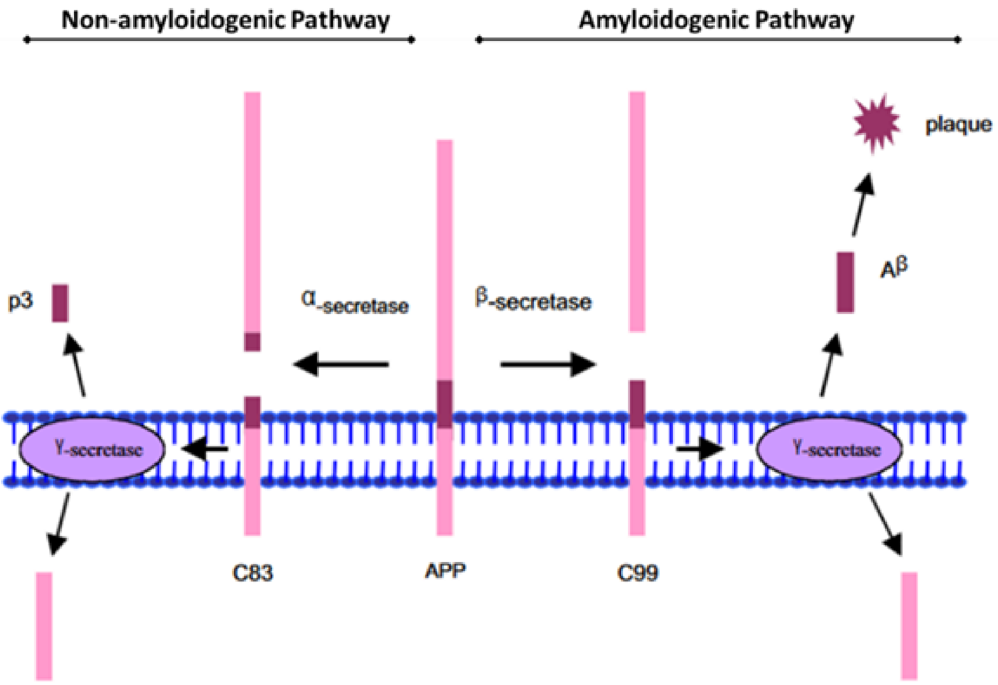

Figure 1.4 | The amyloidogenic and non-amyloidogenic processing of APP. Image from Ref. [287].

After a successive intramembrane cleavage by γ-secretase, amyloid peptides consisting in 39-42 residues are released. The Aβ forms in brain deposits, which are thought to be more involved in AD pathogenesis, are the ones with 40 and 42 residues, two isoforms of different length. The 40-residue peptide $A\beta_{1\text{–}40}$ represents the most abundant Aβ isoform in the brain in vivo[89], whereas the more aggregation-prone, 42-residue variant $A\beta_{1\text{–}42}$ is the major proteinaceous component of the extracellular senile plaques that are the hallmarks of this disease[90]. Despite they only differ by two amino acids in the C-terminal region, yet they display markedly different aggregation behavior[91].

Aβ amyloid fibrils have been analyzed with several biophysical and biochemical techniques, such as solid-state NMR spectroscopy, Electron Microscope (EM), AFM, ThT kinetics studies or mutagenesis[27,34,37,92].

These analyses have provided a wealth of information about specific structural details of the peptide in the fibril and the fragment comparison. The results obtained by using scanning transmission electron microscopy (STEM), suggest that $A\beta_{1\text{-}40}$ and $A\beta_{1\text{-}42}$ share the same fundamental protofilament structure. Some different morphologies observed would, therefore, arise mainly from the different packing and number of protofilaments[93].

Kinetics study, using fluorescence lifetime imaging (FLIM), shown a clear difference between the two peptides to form mature fibrils within live neuronal cells. $^{HF488}A\beta_{1\text{-}40}$ appears to exhibit a lag phase in its aggregation, whereas $^{HF488}A\beta_{1\text{-}42}$ shows no such effect and aggregates rapidly soon after it is internalized into the cells[94]. The latter confirmed by in vitro studies of ThT fluorescence spectroscopy, that exhibit a decreasing in the rate constants for $A\beta_{1\text{-}40}$, relative to $A\beta_{1\text{-}42}$, indicating higher energy barriers to overcome for all microscopic processes during the fibrillation pathway[91,95].

1.4 The generic nature of amyloid structure

One of the remarkable characteristics of the amyloid diseases is that, despite the difference between the associated precursor, amyloid fibrils are very similar in their overall properties and appereance[96]. Starting from this evidence, several studies, in the last two decays, supported the idea that the ability of the protein structure to self-organize into polymeric assemblies is a generic property of the polypeptide chains[97]. *In vitro* studies report how a range of proteins, with no known connection with any disease in vivo, undergoes conversion in vitro into fibrils very similar to those associated with amyloid disease[98,99]. Since first evidence (summarized in Table 1.2)[9,100,101] several studies highlight many other proteins, unrelated to any amyloid disease, able to form amyloid fibrillar aggregates in vitro. This ability occurs under appropriate destabilizing condition, *e.g.* low pH, lack of specific ligands, high temperature, or the presence of specific co-solvents, such that the native structure was partially or completely disrupted[9,102,103].

Table 1.2 | Proteins unrelated to diseases that form amyloid fibrils in vitro (Ref. from [8], data updated at 2003)

Domain/Protein	Year
SH3 domain p85 phosphatidyl inositol-3-kinase (bovine)	1998
Fibronectin type III module (murine)	1998
Acylphosphatase (equine)	1999
Monellin (Dioscoreophyllum camminsii)	1999
Phosphoglycerate kinase (yeast)	2000
B1 domain of IgG binding protein (Staphylococcus)	2000
Apolipoprotein CII (human)	2000
ADA2H (human)	2000
Met aminopeptidase (Pyrococcus furiosus)	2000
Apocytochrome c (Hydrogenobacter thermophilus)	2001
HypF N-terminal domain (Escherichia coli)	2001
Apomyoglobin (equine)	2001
Amphoterin (human)	2001
Curlin CgsA subunit (Escherichia coli)	2002
Vl domain (murine)	2002
Fibroblast growth factor (Notophthalmus viridescens)	2002
Stefin B (human)	2002
Endostatin (human)	2003

As already mentioned above, the core structure of the fibrils is stabilized primarily by interactions, particularly hydrogen bonds, involving the polypeptide main chain. Because the main chain is common to all polypeptides, this observation explains why fibrils formed from polypeptides of very different sequence seem to be so similar[104,105]. The propensity to assume fibrillary conformation under given circumstances can vary markedly between different sequences. The relative aggregation rates for a wide range of peptides and proteins correlates with the physicochemical features of the molecules such as charge, secondary-structure propensities and hydrophobicity. In a globular protein, the polypeptide main chain and the hydrophobic side chains are largely buried within the folded structure. The propensity to convert into amyloid fibrils increase considerably when the structures are exposed, for example when the protein is partly unfolded (e.g. at low pH) or fragmented (e.g. by proteolysis)[106].

The revolutionary discovery that the proteins can undergo fibrillation if placed in a specific denaturing condition, represent an important step forward in the investigation of amyloid pathologies. Therefore, the capability to reproduce the amyloid aggregates behaviour, also in terms of toxicity, employing a highly simplified system can offer additional insights into the molecular details of amyloid fibril formation[107,108].

This approach is particularly useful, for instance, to obtain very controlled processes of aggregation, avoiding the variability displayed in the aggregation of some pathological peptides, such as the ones involved in AD, which can be difficult to handle during some kind of experiments.

1.5 Insulin fibrillogenesis

In this section, a brief introduction of the model protein employed in this work is provided. We have chosen bovine insulin to study amyloid fibrils. The fibrillation process of insulin is very well characterized. Moreover, suitable conditions in order to obtain fibrils on a timescale that is compatible with the experimental time scale can be selected, making this peptide suited for in vitro experiments[60,109].

1.5.1 The model system: bovine Insulin

Insulin is a protein hormone with a largely α-helical structure, which plays a crucial role in the carbohydrate metabolism and several other body systems, e.g. vascular compliance, and it is naturally produced in the Islets of Langerhans in the pancreas[110]. It has been a well-studied fibril-forming protein widely investigated and commercially available in large quantities, at reasonable price, resulting as an excellent model system to study fibrillation.

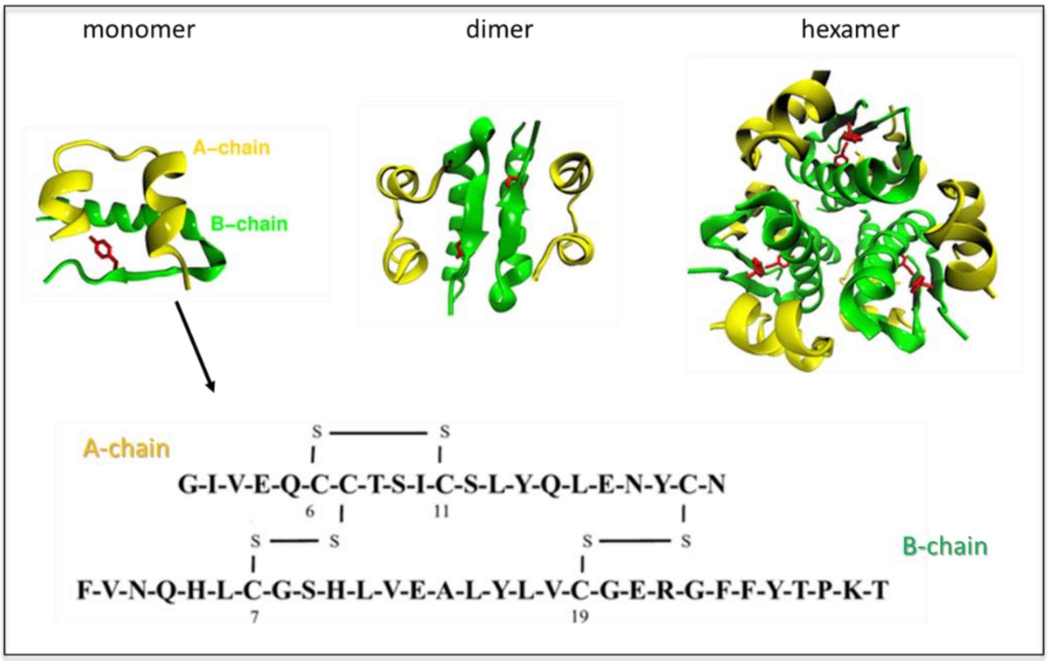
monomer
dimer
hexamer
A–chain
B–chain
A-chain
S — S
G-I-V-E-Q-C-C-T-S-I-C-S-L-Y-Q-L-E-N-Y-C-N
6
11
S — S
S — S
B-chain
F-V-N-Q-H-L-C-G-S-H-L-V-E-A-L-Y-L-V-C-G-E-R-G-F-F-Y-T-P-K-T
7
19

Figure 1.5 | Structure of Insulin. Upper line: From left to right: the monomeric hormone (A and B chains) forms dimers via anti-parallel association of B chain α-helices and C-terminal β-strands; assembly of three dimers to form hexamer. Images from *RCSB Protein Data Bank (PDB) 2ZP6*. Bottom line: primary structure of monomeric human insulin.

Primary structure of bovine insulin was reported by Sanger in 1951[111,112]. Mainly the protein is composed of 51 residues located along two polypeptidic chains the A-chain, which consists of 21 amino acids, and the B-chain of 30 amino acids, linked together by two interchain and one intra-chain disulfide bonds[110,113] (*Figure 1.5*). Bovine insulin differs from the human type by changing two aminoacids in the sequences of the A-chain and one of the B- chain[114–116]. The secondary structure of the A-chain and B-chain consists of two α-helices and a combination of one α-helix and a β-strand, respectively. Non-covalent interactions between residues of the two chains stabilize the tertiary arrangement and determine the structure of the monomer with a hydrophobic core and polar residues located on the external surface. Assembling of monomers in higher hierarchical species is strongly dependent on physical and chemical parameters of the solution as pH, solvent composition, and temperature as well as on insulin concentration.

Several human diseases are related to an aberrant mechanism of insulin production. Besides insulinoma, metabolic syndrome, polycystic ovary syndrome, a high social impact is represented by the diabetes Type I and Type II related to the insulin deficiency and insulin resistance, respectively. Also, amyloid deposits have been observed in type II diabetes patients and in normal aging after subcutaneous insulin infusion and repeated insulin injections[117]. Aggregation and fibrillation of insulin cause problems during production, storage, and delivery[118]. Actually, during the preparation of recombinant insulin for clinical use, it is subjected to low pH, high ionic strength, increased shear, and organic solvents, all conditions that promote fibrillation. For all these reasons, in the last decades, the insulin-based pharmacological formulation has attracted the interest of many researchers.

Insulin from the bovine pancreas is not an amyloidogenic protein in vivo. On the other hand, it has been demonstrated that peptides and proteins that are unrelated to disease have a generic ability to form amyloid fibrils upon destabilization of their native structure induced by particular environmental conditions[100,101,119–121].

1.5.2 Insulin fibril formation

Insulin is mainly stored into an inactive form with long-term stability, i.e. zinc-coordinated hexamer, while zinc-free insulin is a dimer formed at a low concentration over the pH 2-8 range, shifting to a tetramer at protein concentrations of >1.5 mg/ml. Nielsen et al. studied the effect of pH on the association of human and bovine insulin. At pH 7.4 insulin is hexameric and it dissociates upon decreasing the pH. At pH 3 insulin exists as a tetramer, at pH 2.0 is monomeric in acetic acid and at pH 1.6 insulin is dimeric[122]. Formation of insulin fibrils is a physical process in which non-native molecules interact with each other to form linear, biologically inactive aggregates[110]. The early in vitro studies on insulin fibril formation has been shown to result in the formation of insoluble aggregates which are rich in β-sheet structures by using infrared dichroism and wide angle x-ray diffraction[123,124].

Moreover, in vitro at low pH and high temperature, insulin is very prone to form amyloid fibrils[125], thus constituting a suitable model system to study some different and unknown aspects of the amyloid molecular mechanisms. The model has been used both to characterize the mechanical properties of individual amyloid fibrils and to determine the growth rate of amyloid fibrils[126,127].

In the last two decay, regarding insulin protein, many different molecular mechanisms responsible for amyloid formation and protein aggregation have been proposed. It has been shown that the formation of insulin fibrils occurs from different phases, similar to those described in Section 1.2, in which a number of reactions take place.

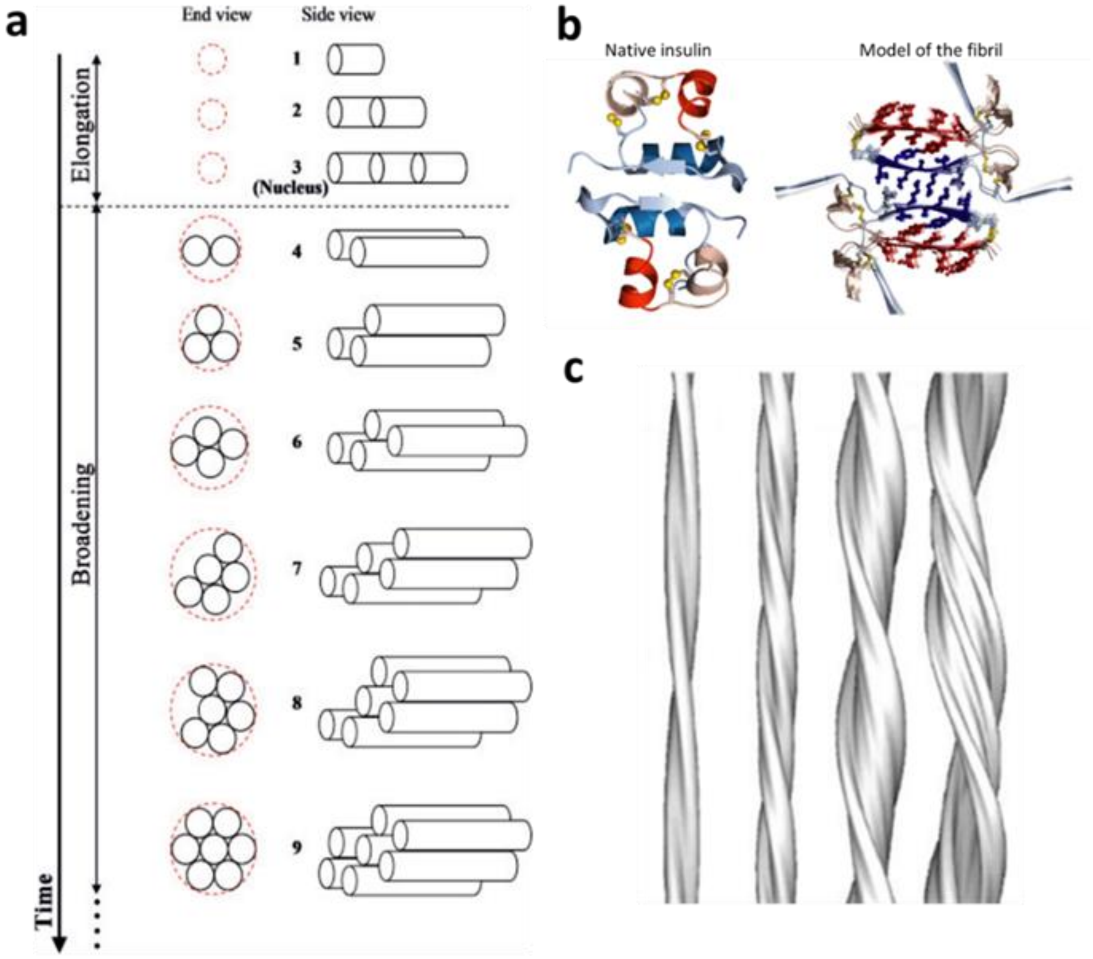

Figure 1.6 | Model for nucleus formation and growth from insulin protein in acidic environment (a) Prior to nucleus formation, ‘‘elongation’’ dominates; after nucleus formation, ‘broadening’’ occurs (from *ref.* [130]). (b) (Right) View of fibril model, looking down fibril axis. One layer of fibril model is made by stretching both monomers of native insulin (left) in a horizontal direction converting the deep blue helix of the B chain and the deep red helix of the A chain into extended β-strands. The spine of the fibril consists of a dry steric zipper formed by the mating of the central two strands from the B-chains of the two insulin molecules, plus two outer strands from the A-chains of the two molecules (from *ref.* [288]). (c) Surface representation of 3D maps of the four insulin fibril structures. (From left to right) Structure of the fibril with a pair of protofilaments twisting around each other. The four-protofilament compact fibril. The six-protofilament fibril. The twisted ribbon. The protofilaments are well resolved in the first three structures, but are less clear in the twisted ribbon (from *ref.* [36]).

Nielsen et al. conducted insulin aggregation studies with human insulin, bovine insulin and insulin mutants at various conditions, including incubation at 60 ˚C, pH 1.6 at insulin concentrations of 2 mg/ml. All of their kinetic results was monitored by the fluorescent probe, thioflavin T, and shown to be consistent with a nucleation-dependent elongation mechanism via the initial formation of a partially folded intermediate conformation[124]. They concluded that both nucleation and fibril growth were influenced by external factors, such as hydrophobic and electrostatic interactions[122]. Several other studies highlight how this process can be influenced, in term of time, by other growth mechanisms such as secondary nucleation (the presence of already formed fibrils in solution)[128] and the behaviour of insulin fibrillation in confined environments[129].

Furthermore, the measure of the temporal formation of insulin oligomers, in different solvents, by small-angle neutron scattering (SANS), suggest a universal pathway for amyloid nucleus and precursor formation using insulin model[130]. This study suggests that, as described for β-amyloid peptide oligomers by scanning tunnelling microscopy and small-angle x-ray scattering[123,131], as well for insulin, the elongation occur by the assembly of individual monomers to the growing fibril. In addition, studies during the early stages of in vitro fibrillation of insulin, demonstrate that the generated nucleus, during the initial critical phase, comprises three dimer units or six monomeric units. The nucleus of three cylindrical-shaped insulin dimers join end-on to form a hexameric nucleus (elongation in *Figure 1.6a*) which then aggregates side-on with other nuclei and preformed aggregates leading to the formation of protofilaments (broadening in *Figure 1.6a*). SANS data on insulin molecules showed that prior to nucleus formation, the length of the precursors increases linearly while their radius remains constant. After nucleus formation, the radius increases as per the close geometric packing of the cylinders, and length increases by about 1/12th of the nucleus length due to sliding of the adjoining nuclei[130].

A more thorough knowledge of the structure and mechanism behind the formation of amyloid fibrils in general is essential for the understanding of the processes of amyloidosis. In the next sections, we are going to propose a new and original approach in the investigation of protein aggregation by using an advanced integrated system obtained from the coupling of a standard atomic force microscope and a super-resolution optical microscopes. I disclose some limits that are inherently related to fluorescence methods.

1.6 – Amyloid cytotoxicity

One of the most essential aspects in the plasma membrane study is that a physiological alteration can bring about numerous pathological consequences. For several years a misleading theory about the nature of the toxic agent in Alzheimer's, Parkinson's (the most known diseases that involve protein deposition), and other degenerative age-related diseases took place. For years, most researchers have backed the notion that clumps of long amyloid fibrils located in the brain and other organs are responsible for killing neurons and other cells. In Alzheimer's, these clumps are termed amyloid plaques and consist primarily of the polypeptide amyloid β protein; in Parkinson's, they are called Lewy bodies and contain the protein α-synuclein.

An increasing quantity of recent experimental data suggests, however, that in many cases at least the species that are most highly toxic to cells are the pre-fibrillar aggregates (sometimes referred to as amorphous aggregates, protein micelles or protofibrils) rather than the mature fibrils into which they often develop[73,84,136,250]. In particular, a number of reports concerning Aβ-peptides, α-syn and transthyretin indicate that these early aggregates are the most toxic species[135,251–254]; in addition, the presence of such species has also been reported for huntingtin and possibly the androgen receptor[255] in diseased transgenic mice.

Such toxicity is likely to arise from the 'misfolded' nature of the aggregated species and their precursors and from the exposure of regions of the protein (e.g. hydrophobic residues and the polypeptide main chain) that are buried in the native state. As many of these regions are likely to be aggregation-prone (or 'sticky') they may be able to interact with membranes and other cellular components[72]. Indeed, in an ensemble of small aggregates containing misfolded polypeptide chains there will be a vast array of exposed groups of amino acids, some of which may mimic regions of the surfaces of native proteins. Such aggregates are therefore likely to be able to interact inappropriately with the binding partners or receptors of a wider range of different proteins. Indeed, the intrinsic instability of pre-fibrillar species that enables them to assemble further and become organised into more highly ordered structures itself reflects the existence of accessible regions of the structures.

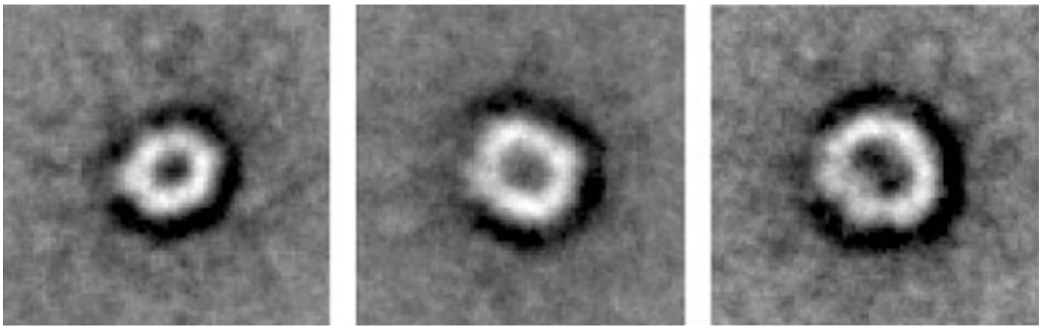

Figure 1.7 | Electron microscopy image of prefibrillar aggregates. The images refer to the α-syn mutant (A53T) aggregation, involved in Parkinson's disease. In the first stage of aggregation the protein shows a characteristic pore-like structure[290]. The images show an area of 30.5x30.5 nm.

In agreement with these conclusions, pre-fibrillar assemblies have been shown to interact with synthetic phospholipid bilayers and with cell membranes, possibly destabilising them and impairing the function of specific membrane-bound proteins[256–258].

In particular, it was observed how the membrane lipid composition, especially with respect to the content of cholesterol and anionic lipids, plays a fundamental role in determining the nature of amyloid protein/membrane interaction[74,76,77,259]. The exact mechanism by which amyloid peptide cause damage to the cell is still an open question. The answer may be found in the interaction with the cell interfaces area[51,84,260]. Several studies performed on cells and model systems indicate that toxic oligomers can permeabilize the cell membrane through the creation of pore-like structures[261–263], altering the physiological ionic balance (*Figure 1.7*).

The membrane itself can act as a catalyst for fibrillization[264,265]. Another option is that aggregates interfere with the normal cell processes occurring at the plasma membrane level, binding some portions of the external leaflet[266,267], or penetrating inside the double layer of phospholipids, causing variations in important membrane properties such as fluidity[268]. Other experiments suggested that the main toxic effect is membrane disruption[269,270],which could happen via a detergent-like mechanism[271] induced by peptides aggregation at the surface.

Chapter 2
Microscopy techniques

In this Chapter, I describe the techniques used in this work. The first part is focused on optical fluorescence techniques, with a brief introduction to confocal microscopy. Specific attention is focused on the reference of super-resolution microscopy. The second part is centered on the scanning probe principles, with a specific overview on AFM.

The field of optical microscopy dates back to at least the 17th-century. It was not until the German mechanic Carl Zeiss started producing microscopes in the late 19th century that a more reliable method was established[142]. Employing the Abbe's formula for the calculation of the maximal resolution achievable from an optical microscope, published in 1873, an essential milestone in the history of microscopy was achieved[143]. According to this, the lateral resolution, d, i.e. the minimum distance between two points is:

$$d = \frac{1.22\lambda}{NA_{obj} + NA_{cond}}$$

,where λ is the wavelength of the light, NA_{obj} is the numerical aperture of the objective, and NA_{cond} is the numerical aperture of the condenser. Numerical aperture is defined as the refractive index of the imaging medium (n) multiplied by the sine of the aperture angle (α): $NA = n \sin(\alpha)$. Additional enhancement has been made to the basic design of the optical microscope. One such modification has been the development of fluorescence microscopy to look at samples that hold fluorescent properties. Fluorescence microscopy has become an indispensable tool in biology and in life sciences because of its unique advantages: it is a largely non-invasive technique and it can probe the deeper layers of a specimen at ambient conditions and enables spectroscopic diagnosis with chemical sensitivity. The photophysical process in a conventional fluorescence microscope is best described by Jablonski diagrams[144] (*Figure 2.1*). Even though fluorescence microscopy has enabled an improvement in visual perception, the resolution is ultimately restricted by the, above mentioned, diffraction limit and, further, by the conditions imposed by the Rayleigh criterion. It is possible to increase resolution by using short wavelength excitation sources and by increasing the numerical aperture of the objective lens, which thus increases the area over which the objective collects light from the sample. This, however, does reach a limit in experiments when the length scale of a sample reaches around 200-300 nm, in line with the λ/2.

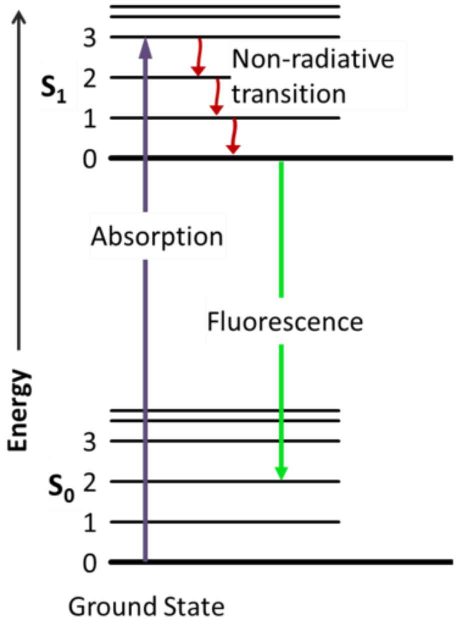

Figure 2.1 | Simplified Jablonski energy diagram representing fluorescence. The purple arrow represents the absorption of light. The red arrow represents vibrational relaxation from singlet-excited state, S_2 to S_1. This process is a non-radiative relaxation in which the excitation energy is dispersed as vibrations or heat to the solvent and no photon is emitted. The green arrow represents fluorescence to the singlet ground state, S_o. (Image from *Wikimedia Commons*)

In this scenario, several advanced concepts aimed at pushing the diffraction limits by reducing the focal spot size. Confocal fluorescence microscopy[145], described in the next section, is one of them.

Importantly, in 1994, by Hell and Wichman[146] STED super-resolution technique was introduced, breaking the diffraction limit.

Due to the intrinsic resolution limitations imposed on optical microscopy, other forms of microscopy are required to probe objects past the diffraction limit. One such technique is that of scanning probe microscopy[147], which can measure both surface topography at the atomic scales. One of the most useful and largely utilized forms of scanning probe microscope is the AFM.

Considering that every technology entails have intrinsic limitations, I thought that correlative techniques are a necessary step towards the achievement of a richer set of informations.

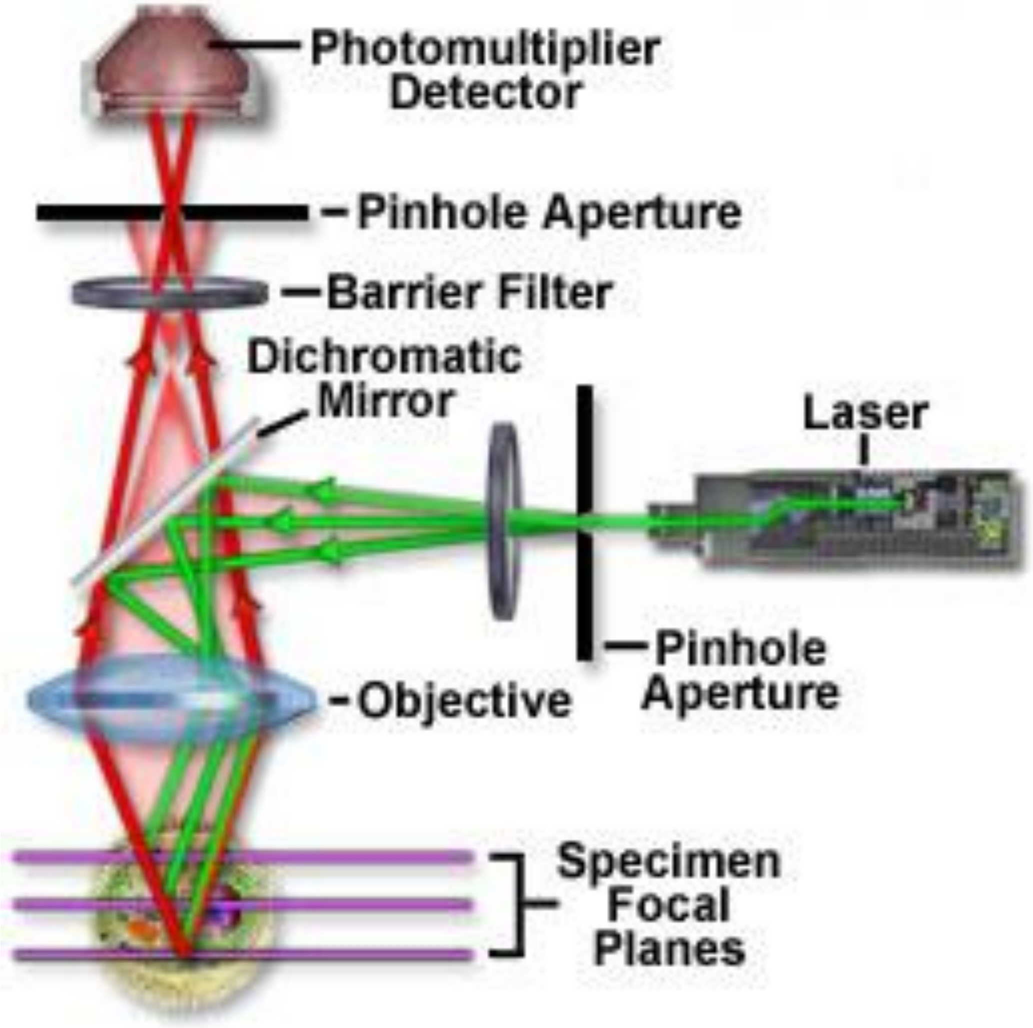
Photomultiplier Detector
Pinhole Aperture
Barrier Filter
Dichromatic Mirror
Laser
Pinhole Aperture
Objective
Specimen Focal Planes

Figure 2.2 | Schematic configuration of laser scanning confocal microscope optical setup. The light coming from the laser passes an (excitation) pinhole, and a dichroic mirror rejects it and focused by a microscope objective to a small spot on the sample. A dichroic mirror reflects one wavelength while transmits the others All the light originating from the in-focus plane will pass freely through the pinhole, whereas the pinhole will mainly block light arising from an out-of-focus plane. (Image from *http://zeiss-campus.magnet.fsu.edu*).

2.1 Confocal microscope

In many areas of current research interest, such as cellular biology, Confocal fluorescence microscopy result to be a useful approach. Due to the relative ease with which extremely high-quality images can be collected from specimens prepared for conventional optical microscopy, it has been extensively employed. The confocal principle relies on upon enhancement of both lateral and axial resolution, overcoming the limitations of the traditional wide-field fluorescence microscopes. Since the development of the 'automated scanning' concept using a fluorescence microscope[148] and the first optical sectioning design[149], it has been gave the opportunity to produce the first clear images of focal planes deep within a thick sample, leading to the development of the laser scanning confocal microscope[150].

In a conventional fluorescence microscope, in which the entire sample is flooded with light from a light source, all the sample within the optical path is excited at the same time. Consequently, the fluorescence detected by the microscope's photodetector is comprising a large unfocused background part. In contrast, the confocal microscope bases its working principle on the introduction of a small aperture (pinhole) in order to eliminate out-of-focus signal. In detail, both of the laser beams, focused on the specimen, and fluorescence light emitted by the dye molecule, are passing through a small pinhole before reaching the photomultiplier (detector). The focal point in the sample and the pinhole lie in conjugate planes; this optical arrangement is called 'confocal'. Since only the light from the focal point can pass the pinhole and can be measured by the detectors[151], the resolution increases but at the expense of decreasing signal intensity. It should also be specified that the resolution in confocal microscopy is limited by the size of the focal spot. The full-width half-maximum (FWHM) radius (Δr) of the focal spot produced by an objective with numerical aperture NA=$n\sin\alpha$ focusing light of wavelength λ is

$$\Delta r = \frac{\lambda}{2nsin\alpha} = \frac{\lambda}{NA}$$

,where n is the refractive index of the medium in which the objective is working and α is the maximal half-angle of the light cone that can exit the lens.

For a typical oil immersion objective (*n* = 1.516), an objective with NA = 1.4 and light of wavelength λ = 640 nm the FWHM of the focal spot would be about 230 nm. This would not allow a detailed observation of nanometric features, such as the amyloid fibrils investigated in this work[152]. *Figure 2.2* shows the scheme of the optical path in an inverted configuration of a modern confocal microscope.

2.2 Super-resolution fluorescence techniques

In the last two decays, a series of original approaches open the way to a new class of far-field microscopy, defined as SR optical microscopy or merely nanoscopy techniques, that shattered the diffraction barrier, improving spatial resolution by an order of magnitude or more over the diffraction limit. These techniques have the potential to provide new insights into biological processes at the, hitherto inaccessible, molecular scale suggesting new amazing applications for the next future[153].

The use of light in far-field optical nanoscopy has been brought to the forefront with the 2014 Nobel Prize for chemistry[154], with fluorescent stimulated emission depletion microscopy (STED). It was achieved a real optical lateral resolution of~30 nm and single-molecule microscopy capable of revealing intra-cellular details of tens of nm using the super localization of fluorescent marker molecules[155–157]. Several other techniques, as well as STED, in the field of SR optical techniques are based on the use of fluorescent molecules. , such as stochastic optical reconstruction microscopy (STORM)[158–160], photoactivation localization microscopy (PALM)[161], reversible saturated optical fluorescence transitions (RESOLFT)[162], and structured illumination microscopy (SIM)[163,164].

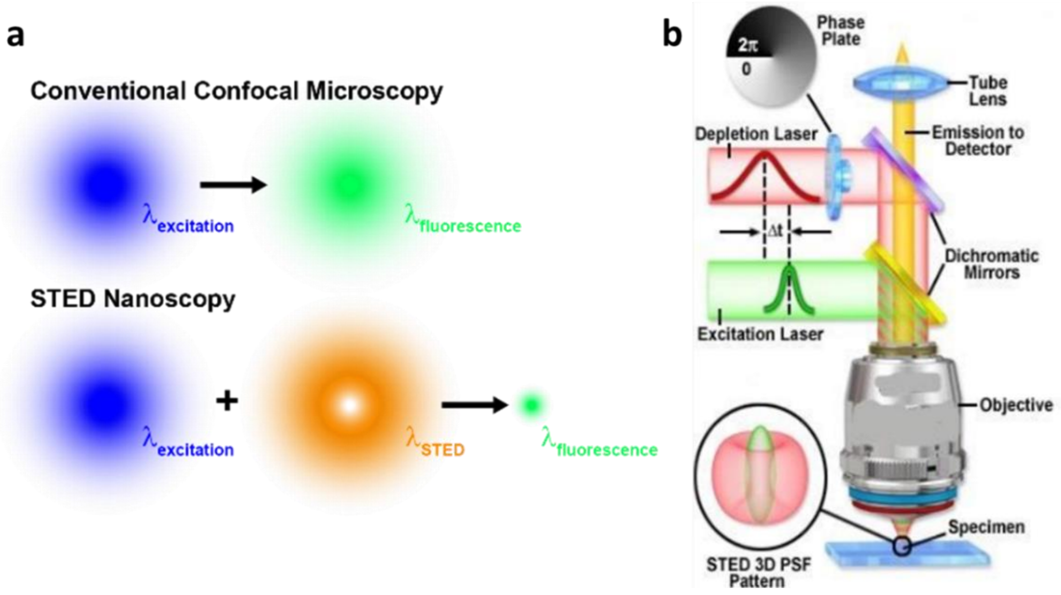
a
Conventional Confocal Microscopy
λexcitation
λfluorescence
STED Nanoscopy
+
λexcitation
λSTED
λfluorescence
b
Phase Plate
2π
0
Tube Lens
Depletion Laser
Emission to Detector
Δt
Dichromatic Mirrors
Excitation Laser
Objective
STED 3D PSF Pattern
Specimen

Figure 2.3 | (a) Conventional confocal microscopy compared with Stimulated Emission Depletion (STED) nanoscopy. It uses (in addition to a fluorescence excitation laser) a second, ring-shaped laser to quench fluorescence. (b) Schematic configuration of STED system. *(*Image from *http://zeiss-campus.magnet.fsu.edu).*

2.2.1 Stimulated Emission Depletion Microscopy (STED)

Stimulated emission depletion (STED) fundamentally overcome the far-field diffraction limit in fluorescence microscopy. The underlying idea is to switch the marker molecules in a controlled way between a bright (fluorescent) state and a dark state[165]. The switching is performed by utilizing the process of stimulated emission. As shown in figure 2.3, compared with a conventional confocal microscope, it uses, in addition to a fluorescence excitation laser, a second, ring-shaped laser to quench fluorescence. In particular, in order to switch off the ability of the markers to fluoresce, a second beam of light inducing the stimulated emission, called STED beam, is overlaid to the focal spot of the excitation laser. The depletion laser is spatially shaped into an optical vortex beam, commonly referred to as a doughnut beam such that it has an intensity minimum at its centre (coaligned with the maximum of the excitation laser). This confines fluorescence emission to the centre of the focal spot and reduces the size of the effective focal spot from which fluorescence can be emitted. The technique is derived from the Confocal basic principle thereby the coaligned depletion and excitation beams are scanned across the sample[165].

A complete depletion from the periphery of focal volume can be ensured by increasing the number of events, which is simply done by increasing the depletion laser intensity in this doughnut-shaped depletion focus and thence gaining a higher resolution. The use of the STED on biological material sets limits on the depletion laser intensity since the sample can easily undergo to photo-damages[166]. Besides, the power of the STED depletion laser source is limited through a photobleaching effect, i.e. an irreversible chemical degradation of a fluorophore into a non-fluorescent species, when the intensity is too high. The phenomenon occurs from excited states where molecules have more energy and a greater probability of reacting with their surroundings, becoming non-fluorescent (photobleached). In this regard, it is necessary to find the right balance between lost of information and lost of resolution[167,168].

Since the first work describing STED microscopy as super-resolution method in 1994 by Hell et al. and its demonstration in 2002 a range of STED methods have been developed based around this principle[169]. In general, these techniques differ in the type of laser used for depletion, pulsed or continuous wave (CW), and the depletion intensity required for a given resolution. The STED pulses beam, despite the highest efficiency with the lower average power, require synchronization with their excitation counterparts. The apparent need for sophisticated pulse preparation hampered the wider use of this technique[170]. In order to greatly simplifies the system, STED microscopy has been implemented with CW lasers, making the use of pulses obsolete in many cases. Among the greatest challenges for implementing microscopy is choosing suitable fluorescent probes due to the potential involvement of fluorescent dark states in photobleaching. In short, the fluorophores trapped in the triplet state must be able to relax to the ground state before the depletion beam moves to the next spatial location. It has been suggested that STED with CW lasers can be further improved by using time-gated detection which rejects lower resolution early emitted photons[171]. Viable for fluorophores with low triplet yield, the use of time-gated modes coupled with CW light sources (gCW-STED) greatly simplifies the implementation of this concept of far-field fluorescence nanoscopy, opening the way for a versatile tool for biological nanometer scale investigation[166].

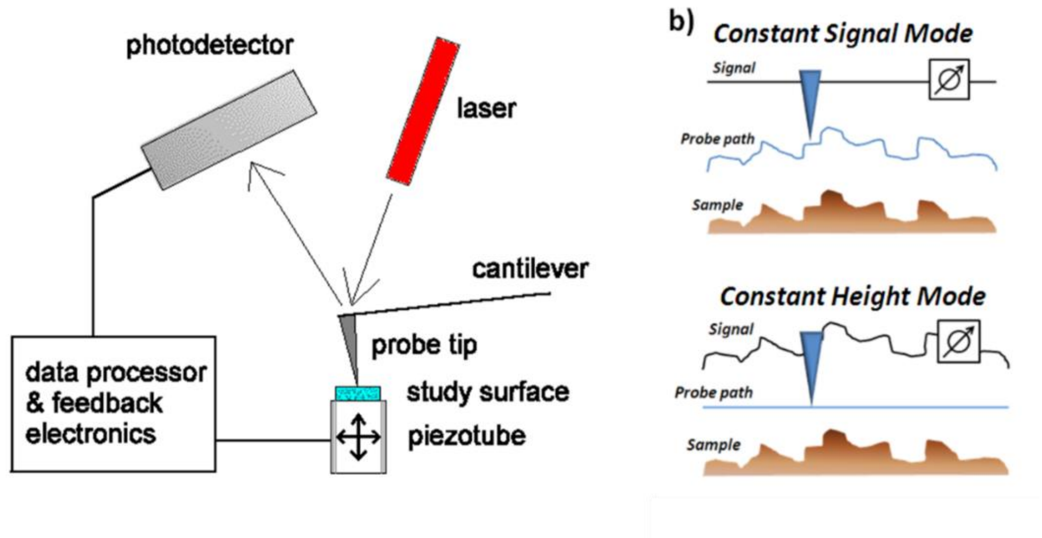
photodetector
laser
cantilever
probe tip
study surface
piezotube
data processor
& feedback
electronics
b)
Constant Signal Mode
Signal
Probe path
Sample
Constant Height Mode
Signal
Probe path
Sample

Figure 2.4 | (a) Schematic representation of a Scanning Probe Microscope. b) Different acquisition modes, with (constant signal) or without (constant height) Z-feedback loop.

2.3 Scanning Probe Microscope – the blind microscope

The history of SPM starts in 1981 with the invention of the first member of the family, the scanning tunnelling microscope (STM) by Gerd Binnig and Heinrich Rohrer, that led to winning the Nobel Prize in 1986[172]. The revolutionary microscope was capable of displaying the topography of surfaces down to atomic resolution. The invention constituted a major breakthrough in the field of physics. SPM techniques are based on the interaction between the sample and a sharp probe, which is scanned over its surface following a raster path. SPM scanners are made of piezoelectric ceramic materials, which can experience a mechanical deformation if an electric potential is applied, allowing the very accurate displacement of the tip. The most commonly used SPM scanners are piezoelectric tubes capable of controlling probe movements in X, Y, and Z at the same time. However, in recent years the use of flexure scanners, based on piezoelectric stack actuators, is generally preferred, since they allow a complete decoupling of motions in different directions, avoiding the intrinsic non-linearity of piezoelectric tubes.

During imaging acquisition, the interaction between the sample and the probe generates a signal at each scanned point (cantilever deflection, cantilever amplitude/frequency of oscillation). Such signal depends on the distance between the probe and the sample allowing the reconstruction of surface topography. SPM system can work in either in constant-height mode or constant-signal mode (*Figure 2.4*). In the first, the vertical position of the probe is kept constant, and the relative probe-sample distance is directly derived from signal measurement. Whereas, in constant-signal mode a Z-feedback loop controls probe vertical position in order to obtain a specific signal value; the topography is then reconstructed considering the vertical displacement of the piezo. The constant-height mode is faster and extremely sensitive. On the other hand, due to the uncontrolled probe-sample distance, the probe can heavily damage the sample. Constant height mode can be used only on flat samples and for small scan areas.

In scanning tunneling microscopy (STM) measurements, a bias voltage is applied between a conductive or semi-conductive sample and STM probe, which consists in a sharp, conductive tip. When the tip gets close enough to the sample (typically 10 Å far), electrons start tunneling through the gap. The tunneling current detecting result extremely precise and depend exponentially on tip-sample distance, allowing imaging of conductive or semi-conductive flat surfaces with an atomic resolution.

2.3.1 Atomic Force Microscopy (AFM)

The AFM is considered the most successful member of the SPM family. Since the origin in 1986[173], It has been demonstrated to be a powerful tool for imaging biological samples in physiological-like conditions, resolving single molecules and without any label or sample treatments. The significant advantage of AFM, concerning STM technique, is that it also works on insulating samples.

Furthermore, it operates in a large number of working conditions, including air, vacuum, and liquid.

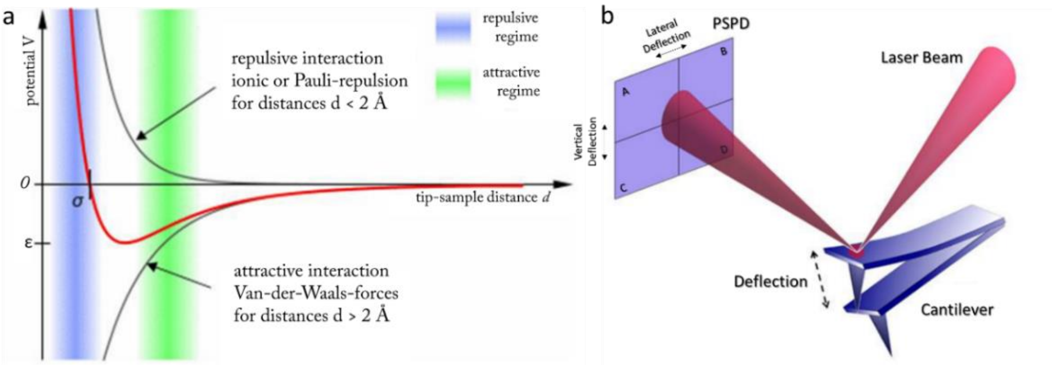
a
potential V
0
σ
ε
repulsive interaction
ionic or Pauli-repulsion
for distances d < 2 Å
attractive interaction
Van-der-Waals-forces
for distances d > 2 Å
tip-sample distance d
repulsive regime
attractive regime
b
Lateral Deflection
PSPD
A
B
C
D
Vertical Deflection
Laser Beam
Deflection
Cantilever

Figure 2.5 | (a) Lennard-Jones potential (red curve), describes interactions between atoms depending on their distance d. It results from the sum of two contributions, related to attractive and repulsive interactions (Image from *http://www.uni-leipzig.de*). (b) Simplified scheme of AFM photodetection system (optical path elements are not shown). Cantilever deflection results in a shift in laser spot position on PSPD. AFM main signal (vertical deflection) is calculated from (A+B)-(C+D), while frictional torsion (lateral deflection) is (A+C)-(B+D).

Working principles

Its working principle is based on the interatomic forces between the probe, generally a sharp tip attached to a suspended cantilever, and the sample. The probe consists of a sharp tip, with a typical radius of curvature (ROC) of 10–30 nm that is attached to the free end of a micro-machined cantilever. The probe cantilever is brought very close to the sample, enabling the tip atoms to interact with the atoms of the sample. These interaction forces deflect the cantilever and the changes in either the static deflection or its dynamic properties are measured to extract the image[174]. The AFM tip perceives two different force regimes. These forces, described by Lennard-Jones potential (*Figure 2.5a*) are characterized by a long-range attractive regime, that include the van der Waals, magnetic and electrostatic forces with an interaction range up to 100 nm, and by a short-range repulsive regime, due to the overlapping of electron clouds and to the repulsion between atomic nuclei.

However, the force exerted by the sample on tip induces a bending on a cantilever. The most employed approach for quantifying cantilever deflection is the one based on optical lever principle[175]. In this detection system (*Figure 2.5b*), a laser beam is focused on cantilever surface, which is coated with a reflective material. The laser spot is reflected on a position-sensitive photodetector (PSPD), which generates a proportional voltage signal. In the absence of interaction, laser reflection is centered on the PSPD. Cantilever bending causes a shift in laser spot position on PSPD, which is proportional to cantilever deflection. Four segments compose PSPD used in AFM, allowing the detection of both vertical and lateral deflection[176].

The cantilever probe is basically a force transducer. It senses the interaction between the tip and the sample and transforms it into a measurable bending of the cantilever. The force is obtained by applying Hooke's law: $F = -kd$, where F is the force exerted by the sample on the tip (and vice-versa), and d represents the vertical deflection. The elastic constant k depends on cantilever geometry: short, thick cantilevers present high k values, while long, thin cantilevers are softer. Reference k values are generally reported for commercial probes, but, if we are interested in knowing exactly the applied force, it is advisable to calibrate each cantilever before measuring. This can be done, for instance, using the thermal noise method[177]. After calibration, force can be easily derived from the measured deflection.

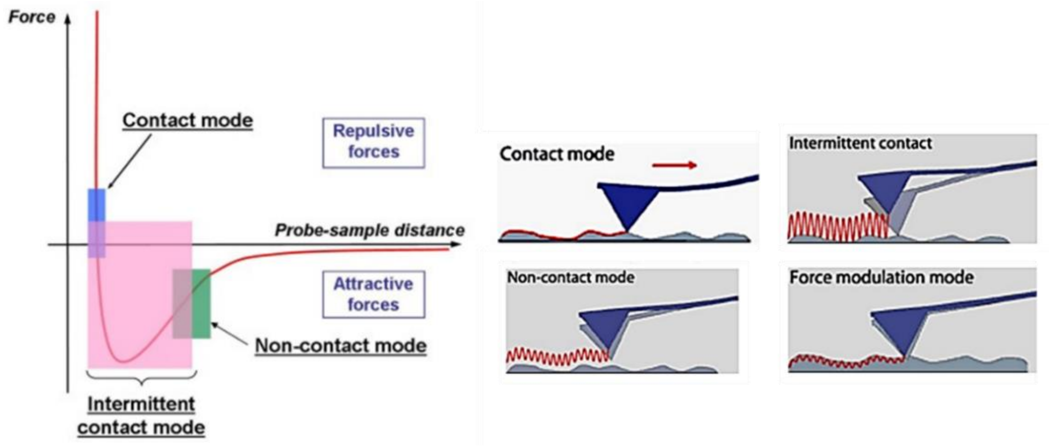
Force
Contact mode
Repulsive forces
Probe-sample distance
Attractive forces
Non-contact mode
Intermittent contact mode
Contact mode
Intermittent contact
Non-contact mode
Force modulation mode

Figure 2.6 | AFM imaging modes (modified from [289]).

AFM Imaging mode

AFM probe can sense objects operating in different modes, depending on the type of sample and on the nature of tip-surface interactions. The main operating modes are indicated as contact mode (static method), intermittent contact mode, non-contact mode, and force modulation mode (dynamic methods), which exploit different interaction force regimes (*Figure 2.6*). As previously discussed, the most frequently used configuration is constant-signal mode in which Z-feedback loop is active and works to keep a measured variable constant, matching it with a chosen setpoint value.

Contact imaging mode operates in repulsive regime where the tip is pushing on the sample and positive force values are measured. Before starting, a force setpoint is chosen, generally low, in order to reduce the interaction with the sample. A feedback control system, during the scan, compares the measured force with the setpoint, driving the piezo in order to maintain the force constant. Contact mode provides the highest resolution and highest stability in AFM imaging.

In intermittent contact mode the tip oscillates near the surface with a frequency close to the resonance of the system. The amplitude of oscillation of the cantilever is the feedback parameter that is maintained constant during the scan, i.e. the more the tip gets close to the sample, the more the free oscillation amplitude is reduced. Intermittent contact involves both repulsive and attractive regime. Since the tip detect the sample in the lower part of the oscillation (repulsive contact force), the interaction with the sample is extremely reduced with respect to contact mode, as well as the lateral force exerted during scanning. Therefore, intermittent contact should be preferred in case of soft, delicate samples, such as the biological ones.

Other kind of information can be indirectly derived from these main acquisition methods: in contact mode, for instance, lateral deflection describes the friction between tip and sample[178], while in intermittent contact different materials can be distinguished from the phase shift, which they induce between the driving signal and the detected one. These secondary imaging modes represent a valid tool for investigating the properties of different sample components[179,180].

Force spectroscopy technique and related methods

The AFM tool is able to obtain other valuable information on sample properties in addition at the capability to perform high-resolution images, even simultaneously. The cantilever, in fact, can be moved along vertical direction on a fixed X-Y position. Starting from a distance far from the sample where the tip-sample interaction is null, the cantilever is approached toward the sample until contact occur and a certain deflection (setpoint) is reached. At this stage, the cantilever is retracted and brought back to the starting situation. The force acting on the tip is measured and plotted against piezo displacement, generating a force-distance curve[181] (*Figure 2.7*). There are a huge number of applications of force spectroscopy, from nano-mechanical investigations of elastic properties to protein unfolding and studies of single chemical bonds. In the last years, a large number of application are related to biological field[182,183].

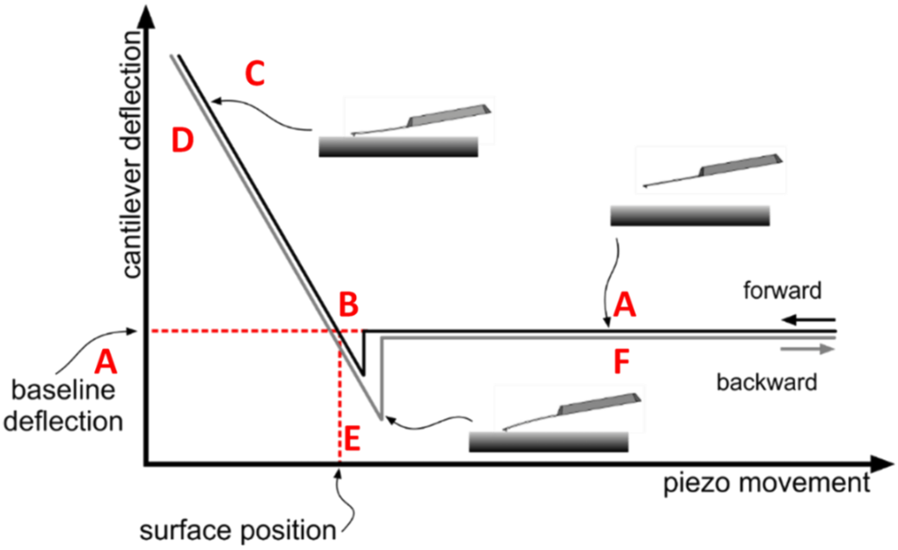

Figure 2.7 | Schematic representation of a force vs distance curve.

The designed method 'Force Volume' concern the acquisition of Force-distance curves on different X-Y position of the sample, possibly regularly spaced in a grid, and also in Z position, collecting the data points in a tridimensional space. The topography of the corresponding area can be obtained as well as in a conventional contact-imaging mode. Height information can be derived for each X-Y point, during the movement performed by the piezo to reach the maximum force setpoint. Furthermore, the information extracted from force-distance curves, representing local physical properties of the sample, can be remapped with a direct reference to the topography. This process can be done automatically during real-time measurement, but in most of the cases it requires a postprocessing. The main drawback of conventional Force Volume is that curve acquisition is extremely time-consuming. Different techniques have been developed to obtain high-speed force volume, including Bruker Peak Force and JPK Quantitative Imaging (QI) mode. In QI mode, the X-Y position is maintained constant during each FD curve acquisition allowing the lateral movements of the tip to be carried out without any interaction between the tip and the sample. This feature can be exploited to image the sample avoiding dragging artefacts, in which the force setpoint is maintain as low as possible, to avoid sample deformation[184].

Table 2.1 | Comparison of high-resolution imaging techniques in molecular and cell biology. Data from *ref.* [186].

Technique /feature	**Atomic Force microscopy**	**Super-resolution microscopy (STED, STORM)**	**Trasmission electron microscopy**	**Scanning electron microscopy**
Resolution	≤1nm	20-50 nm	0.2-10 nm	2-10 nm
Sample preparation and environment	Sample on support; physiological (buffer solution, temperature, CO$_{2)}$	Fluorescence labelling; physiological (buffer solution, temperature, CO2)	Sample on grid; dehydrated (negative stain); vitrified (cryo-electron microscopy)	Freeze/critical point drying and metal shadwing
Artefacts	Tip, force, scanning	Bleaching, toxicity	Dehydration, ice crystal formation, beam damage	Dehydration, metal shadowing, beam damage
Advantages	Imaging under native conditions; no staining, labelling or fixation necessary; high signal-to-noise ratio; assessment of multiple physical, chemical and biological parameters	Access to three-dimensional cellular structure; high spatiotemporal resolution; monitoring biomolecular processes in life cells	Solve atomic structures of proteins; conformational snapshots of proteins and complexes; molecular-resolution structures within the cell	Imaging surfaces of tissues, cells and interfaces at nanometre-scale resolution
Limitations	Restricted to surfaces	Imaging restricted to fluorescence labels	No life processes	No life processes

2.4 Correlative Nanoscopy

Correlative nanoscopy is a new term coined from microscopy methods which correlate two or more different techniques that can visualize and study nanometer-scale details of the sample[185]. Despite the improvement obtained in the field of microscopy, every single technology entails some intrinsic limitations. *Table 2.1* describe advantages and limitations of high-resolution imaging techniques[186]. The aforementioned AFM technique, for instance, because its ability to work in liquid, controlled conditions (temperature, pH, ionic strength, etc.), and label-free has been considered a preferred method to characterized biological structure. On the other hand, in spite of this wide range of demonstrated abilities, this technique alone does not allow the specific identification of individual elements of a heterogeneous sample. This limitation could be restrictive in some molecular environments, such as multi-proteins aggregation or biomembrane .

Fluorescent microscopy is a very popular tool expecially in biological science due to its ability to noninvasively image in all-spatial dimension. Attaching fluorophores to the molecule of interest with antibody, direct covalent labelling or genetic modification is highly specific, enabling sensitive measurement with low background. The use of fluorescent molecules is a key procedure, because, properly labeled, produce the main signal at the basis of the image formation process. Actually, an affordable technique to control (visualize) the fluorophore distribution within the sample, as well as the rise of unpredictable anomalous processes induced by the fluorophore, and that occur locally on a submicron scale, is missing. Several attempts to overcome this limitation were made in the past decades. Moreover, because of the high complexity of biological system a single type of technique is often not enough to obtain an exhaustive characterization of the sample itself. For this reason, the coupling of high-resolution systems could unravel mechanisms that are still open. The study proposed in this thesis was carried on through the use of a technique that combined STED microscopy and AFM.

2.4.1 AFM/STED techniques

AFM can be complemented by optical microscopy in many ways. This can include using the faster imaging speed of an optical microscope to quickly screen a sample and select regions of interest for high resolution AFM imaging[187,188] or combining chemical identification – from fluorescent labelling of the sample – with high resolution AFM imaging to correlate structure with chemical species[189]. In particular, AFM has been correlated with confocal microscopy imaging of the actin cytoskeleton however, due to the limited optical resolution, actin filaments in dense structures could not be observed[187]. Therefore, it has been necessary integrate an optical microscope with a lateral resolution as close as possible to that achieved by scanning probe techniques. In the last years, applications of SR techniques integrated with AFM have been reported on vitro cells[190,159], opening the way to new modalities, e.g. nanomanipulation[191,192].

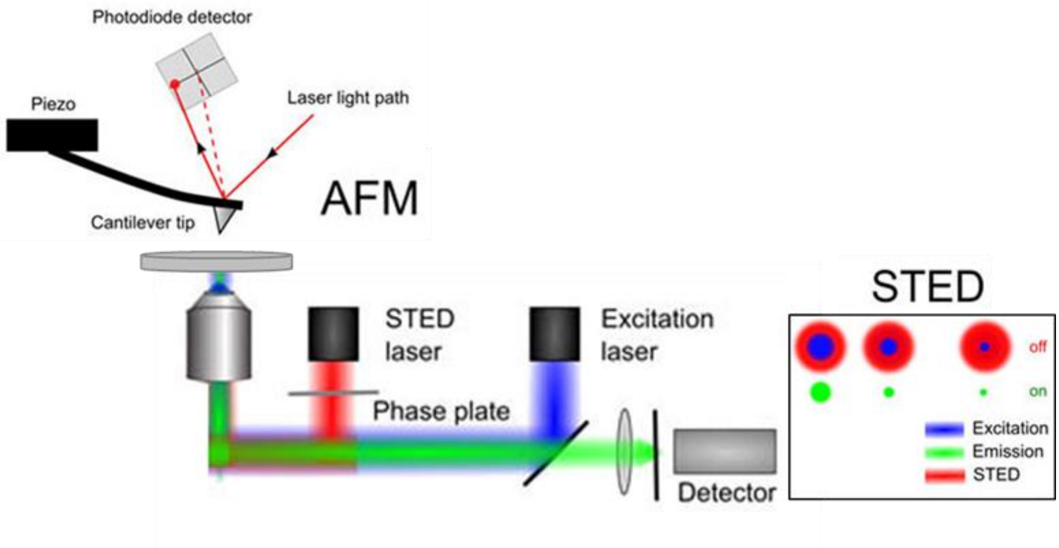
Photodiode detector
Piezo
Laser light path
Cantilever tip
AFM
STED
STED laser
Excitation laser
Phase plate
Detector
off
on
Excitation
Emission
STED

Figure 2.8 | AFM/STED Schematic representation. The confocal and STED images are acquired in reflection, while the AFM probe is reaching the sample from above, providing a 3D topographical view at high resolution.

In *Figure 2.*8 a schematic representation of a combined AFM/STED microscope is shown. The setup and the calibration system will be described in detail in Chapter 3.

Chapter 3
AFM/STED correlative on proteins aggregation

This chapter provides a description of the methodology used during my PhD. The main objective was to obtain new insights on the aggregation process followed by a mixture of fluorescently labeled and unlabeled. For this purpose, it has been proposed a new approach in the study of misfolded protein aggregation, based on the use of a combined system that couple the capability of an AFM, a primary technique in the study of amyloid aggregation in vitro, with that of a stimulated emission depletion (STED) microscope. In particular, amyloid aggregates derived from insulin and two different alloforms of β-amyloid peptides, $A\beta_{1\text{-}42}$, and $A\beta_{1\text{-}40}$ were investigated.

The aggregation process of the peptides was also followed by standard methods (ThT fluorescence, dynamic light scattering and AFM). These techniques were presented in the first part of the Materials and Methods, together with the labeling methods employed. Experimental details of AFM/STED correlative nanoscopy are described in sections 3.9.

Materials and Methods

3.1 - Insulin labeling

Bovine insulin was purchased from Sigma-Aldrich (St Louis, MO, USA) and used without further purification. The protein was labeled with fluorescent dyes, ATTO 488 NHS ester (Sigma-Aldrich, St Louis, MO, USA). NHS-esters readily react with amino groups of proteins, i.e., the ε-amino groups of lysine or the amino-terminus, forming a chemically stable amide bond. In step 1 of *figure 3.1,* the potential binding sites on the monomeric insulin structure are shown.

Labeling was done in a solution of sodium bicarbonate 100 mM at pH 8.3, and mixing monomeric insulin at a final concentration of 2 mg/ml (0.35 mM), with 1 mM ATTO 488, previously diluted in dimethylsulfoxide (DMSO) (Thermofisher, Waltham, MA, USA).

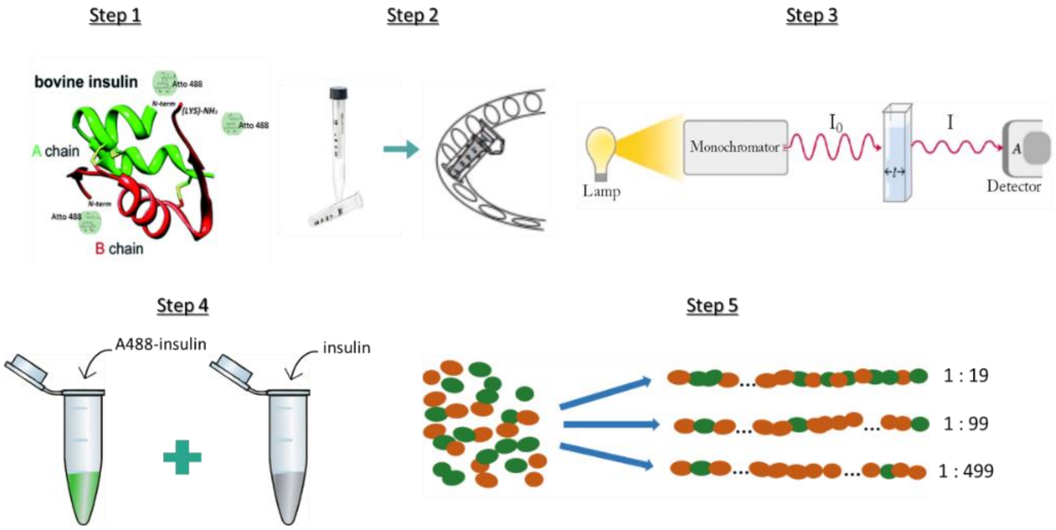
Step 1
bovine insulin
Atto 488
N-term
(LYS)-NH₂
Atto 488
A chain
N-term
Atto 488
B chain
Step 2
Step 3
Monochromator
I₀
I
Lamp
A
Detector
Step 4
A488-insulin
insulin
Step 5
1 : 19
1 : 99
1 : 499

Figure 3.1 | Schematic representation of Insulin Labeling procedure. In Step 1 labeling of insulin. The following step are: Step 2, purification; step 3, quantification; step 4, final solution of labeled and unlabeled insulin in three dye-to-protein ratio; step 5, fibrillation process.

After 1 hour under stirring, the proteins were separated from the excess of free dye via filtration with Amicon Ultra, centrifugal filters (MWCO 3K, Merck Millipore, Milan, Italy) (*Figure 3.1 – step 2*). Immediately after filtration the concentration of the labeled proteins was determined spectrophotometrically (ε_{280nm} 5840 $M^{-1}cm^{-1}$) (Cary spectrophotometer, Agilent, Technologies, Santa Clara, CA, USA) (*Figure 3.1 – step 3*) and adjusted at 1 mg/ml. The unlabeled insulin monomers were added in HCl solution, pH 2, to a final dye-to-proteins ratio (i.e., labeled: unlabeled insulin) of 1:19, 1:99 and 1:499 (*Figure 3.1 – step 4*).

3.2 – Labeled and unlabeled Insulin fibrillogenesis

The fibrillation solution consists of pH 2 Hydrochloric acid (HCl) 37% (Sigma-Aldrich, St Louis, MO, USA) diluted in deionized water. Insulin is dimeric under this condition[110,193] (*Figure 3.2*). Lyophilized insulin peptide was dissolved, at the final concentration of 1 mg/ml (0.2 mM), in HCl solution.

The aggregation was performed on unlabeled insulin or mixed solution at different dye-to-protein ratio (i.e., number of labeled:unlabeled insulin monomers) 1:19, 1:99 and 1:499.

Fibrillation of labeled (described in section 3.1) and unlabeled insulin peptides took place at 60°C in glass vials, without agitation[60]. AFM was used to verify the fibrillation process in the presence and without fluorescent molecules.

The aggregation process was followed for at least 2 weeks. Immediately after the incubation time, the protein samples were diluted 100 times with water and applied onto freshly cleaved muscovite mica for AFM control measurements and on microscope coverslip for AFM/STED images. The dilution of the samples with water immediately quenches the aggregation process. Moreover, for dry condition measurement, deposition on the mica surface is followed by a gently drying procedure by means of a low nitrogen flow to obtain water evaporation, which eventually prevents further aggregation. Successively, AFM images have been taken for each sample.

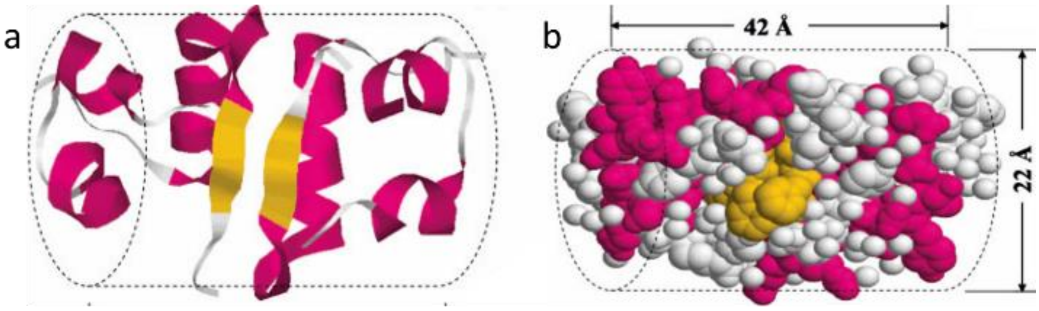

Figure 3.2 | Molecular structure of dimeric insulin at pH 2.0. (a) Ribbon structure showing the secondary structural motifs, and (b) space filled representation of the same dimer. The length and diameter of the cylinder was estimated to be 42 and 22 Å, respectively[193]. (Image from *ref.* [130])

3.3 – Fibrillogenesis of unlabeled and labeled Aβ_{1-42} and Aβ_{1-40}

Lyophilized synthetic human Aβ_{1-42}/Aβ_{1-40} (Bachem, Bubendorf, Switzerland) were dissolved in 100% hexafluoroisopropanol (HFIP) solution (1mg/ml), aliquoted and then stored at -20°C. The storing buffer HFIP is used to avoid aggregates formation before starting the incubation. Beside solvent evaporation, fibrils were prepared by incubating the Aβ protein in 50 mM sodium hydroxide.

Synthetic $A\beta_{1-42}$/$A\beta_{1-40}$-HiLyte Fluor 488 (HF488) (Anaspec, San Jose, CA, USA) were dissolved in 1% Ammonium hydroxide solution (1mg/ml), aliquoted and then stored at -20°C. Labelled peptides were used without further purification. Fluorescently labeled amyloid fibrils were prepared by dissolving unlabeled Aβ in saline phosphate buffer and adding HF488 labeled Aβ to give a final dye-to-protein ratio 1:19, 1:99 and 1:499 at the 25 µM final protein concentration.

Unlabeled and labeled protein solutions were sonicated for 5 min and centrifuged for 10 min at 15000 rcf to separate possible aggregates. The pelleted fractions were discarded, and the supernatant was incubated at 25°C for 1 day without agitation[194]. AFM and DLS were used to exclude the presence of pre-aggregated peptides at the beginning of the fibrillation process. The samples were deposited on the substrate (as previously described for insulin), rinsed with deionized water to remove salts and dried under a mild nitrogen flow before AFM/STED imaging.

3.4 – Immunolabeling analysis of $A\beta_{1-42}$ peptide

Labeling of the fibrils was done by standard immunofluorescence staining. $A\beta_{1-42}$ was prepared as above described in 3.3 section and, a drop of solution after 1 day of aggregation in vitro was deposited on the microscope coverslip previously cleaned and treated with 1M $MgCl_2$. The fibrils were then slightly rinsed, and incubated overnight with mouse monoclonal $A\beta_{1-42}$ antibody (Abcam, Cambridge, UK), diluted in 1% BSA (Bovine serum albumin). The primary monoclonal antibody recognize specifically the amino-terminal residues 1-17 of human Aβ. The samples were rinsed three times with 1% BSA and then incubated with Alexa Fluor 488 secondary antibody (Sigma-Aldrich, St Louis, MO, USA), diluted in 1% BSA for 2 hour, rinsed again with 1% BSA and PBS.

3.5 - Thioflavin T assay

ThT were purchased from Abcam (Cambridge, UK). The stock solutions were prepared by dissolving ~30 mg dry powder in 1 ml water. The solution was filtered through 0.22 µm syringe filters and stored protected from light at 4°C for less than 2 weeks. ThT solution was diluted at different concentration for each proteins. The final concentration of 100 µM with 50µM of insulin protein, while ThT at 50 µM with 25µM of Aβ has been used. A twofold molar excess of ThT is used to ensure saturation of the binding sites. The fluorescence was measured using FluoroMax-4 spectrofluorometer (Horiba Jobin Yvon Inc.) using an excitation of 450 nm[42]. The time evolution of emission maximum which is taken in account as fluorescence intensity measure observed was in the insulin-bound ThT at 490 nm, while in Aβ-ThT at 488 nm.

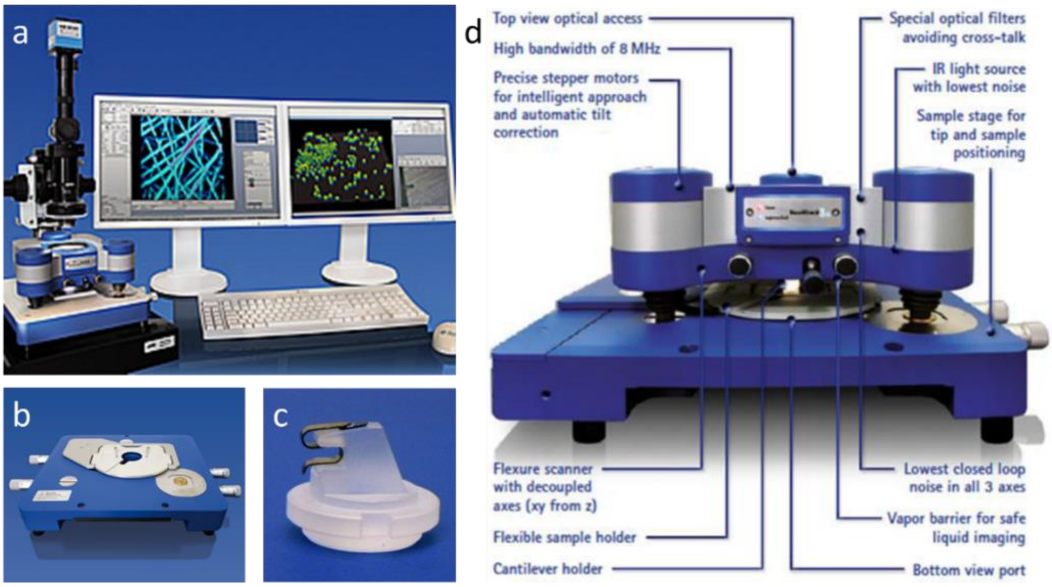
a
b
c
d
Top view optical access
High bandwidth of 8 MHz
Precise stepper motors for intelligent approach and automatic tilt correction
Special optical filters avoiding cross-talk
IR light source with lowest noise
Sample stage for tip and sample positioning
Flexure scanner with decoupled axes (xy from z)
Flexible sample holder
Cantilever holder
Lowest closed loop noise in all 3 axes
Vapor barrier for safe liquid imaging
Bottom view port

***Figure 3.3* | *(a) JPK Nanowizard III with Zeiss inverted optical microscope. (b) Motorized stage with sample holder. (c) Cantilever holder. (d) Description of JPK Nanowizard III. Images modified* from: http://www.jpk.com.

3.6 - Light scattering.

Dynamic light scattering (DLS) measurements were performed with a Malvern instrument Zeta Sizer NanoZS system (Malvern Instruments Ltd., Worcestershire, UK) at a protein concentration of 0.05 mg/ml Aβ_{1-42} and Aβ_{1-40} was dissolved in water, after pretreatment 100% hexafluoroisopropanol and centrifugation for seed removal. The measurements were done immediately after 10 min centrifugation at 15000 rcf.

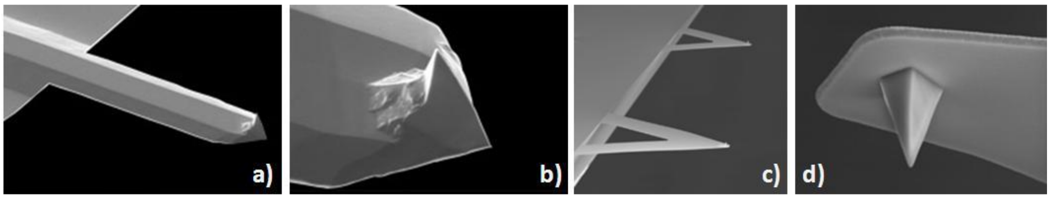

Figure 3.4 | AFM cantilever. (a) Rectangular silicon cantilever for intermittent contact imaging in air. (b) Silicon tip of cantilever in a. (c) Triangular silicon nitride cantilevers for imaging in liquid. (d) Silicon nitride tip of cantilever in c.

3.7 - Atomic Force Microscopy measurements

AFM control measurements were performed by using a Nanowizard III (JPK Instruments, Berlin, Germany) mounted on an Axio Observer D1 (Carl Zeiss, Oberkochen, Germany) inverted optical microscope (*Figure 3.3*). Following a well-established methodology[120,195,196], a drop of the sample solution (20 µl) was deposited on cut muscovite mica mounted on glass slides. The samples were adsorbed, rinsed with deionized water to remove salts and dried under a mild nitrogen flow before AFM imaging.

Images have been acquired in both air and liquid in intermittent contact mode, using rectangular silicon cantilevers (TESPA, Bruker, MA, USA) with nominal spring constant 42 N/m, resonance frequency 320 kHz, and a tip with curvature radius 8 nm, for imaging in air (Figure 3.4 a, b), and triangular silicon nitride cantilevers (DNP, Bruker, MA, USA) with nominal elastic constant of 0.24 N/m, resonance frequency of 64 kHz, and a tip with a typical curvature radius of 20-60 nm, for imaging in liquid (*Figure 3.4 c, d*). All images were acquired as 512 x 512 pixels images with a scan rate between 0.6 and 1.0 Hz.

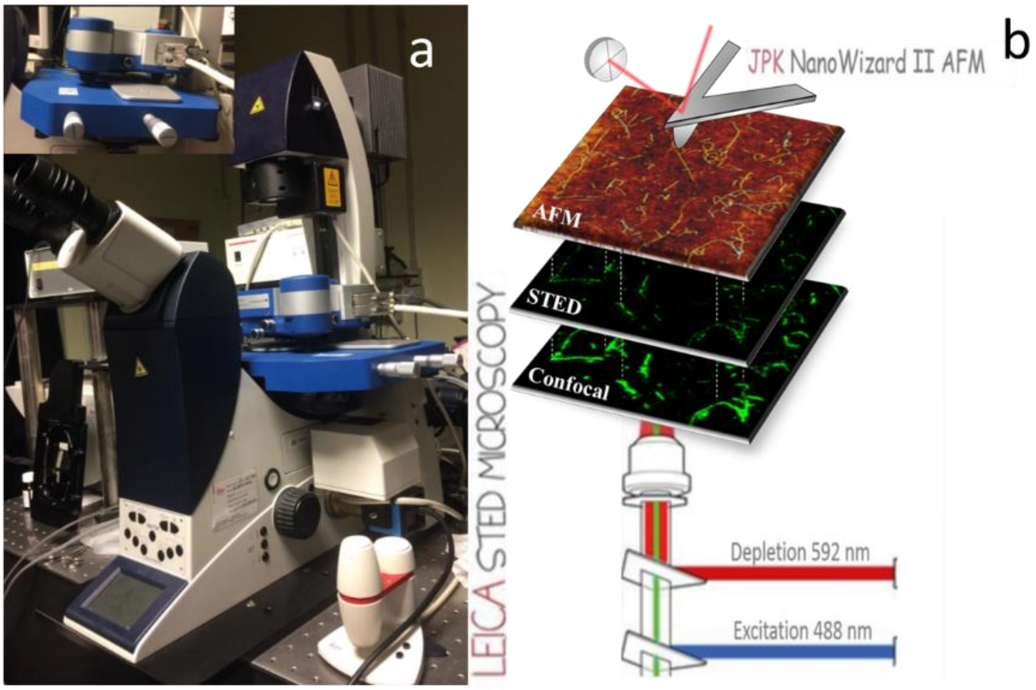

Figure 3.5 | Correlative AFM/STED setup (a). NanoWizard II AFM stage and head in the inset. (b) Images of the same area can be acquired in different modes. The excitation and depletion lasers arrive from below (inverted optical microscope). The confocal and STED images are acquired in fluorescence, while the AFM probe is reaching the sample from above, providing a 3D topographical view at high resolution.

3.8 - Stimulated Emission Depletion Microscope

Commercial Leica STED continuous wave gated microscope (Leica TCS SP5 gated STED-CW, Leica instrument) has been used. STED Images have been collected by a Hybrid detector in the spectral range 470-520 nm[171,197]. We have used an HCX PL APO CS 100x 1.4NA oil objective (Leica Microsystems, Mannheim, Germany) and a scan speed of 1000 Hz for 1024 pixel per line with a 32-line average and a time-gated detection of 1.2 ns. The selected dye was ATTO 488 for insulin and HiLyte Fluor 488 for Aβ measurements, which are suitable for 488 nm excitation and 592 nm depletion wavelengths.

3.9 - Correlative AFM/STED

A NanoWizard II AFM head (JPK , JPK Instruments, Berlin, Germany) was mounted on a commercial Leica STED-gCW microscope, described above (*Figure 3.5a*). The optical microscope stage was exchanged with an AFM compatible stage (JPK Instruments, Berlin, Germany) (*Figure 3.5a inset*), which features minimum mechanical coupling of noise to the AFM cantilever. This procedure is made simple by the availability of suitable mountings for microscope commercial models. The overlay between AFM and STED images (*Figure 3.6*) was performed by using the Direct Overlay software (JPK Instruments, Berlin, Germany).

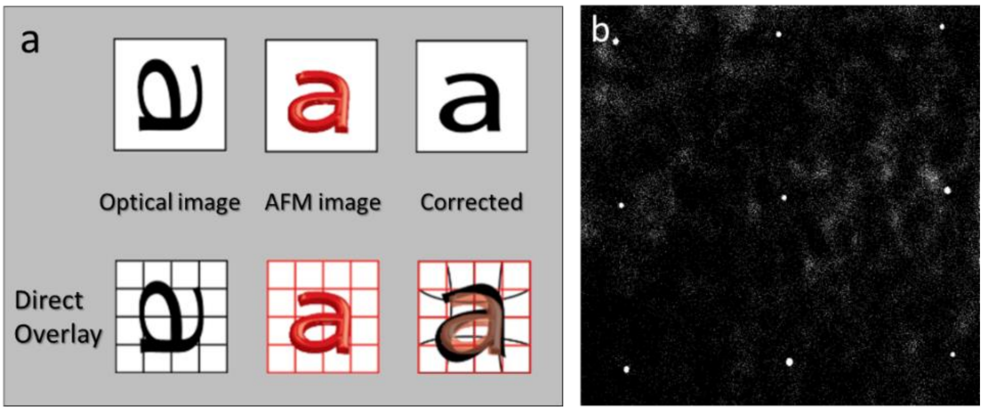

Figure 3.6 | Direct overlay procedure. Panel a shows the total overlay procedure. In the first row of this panel, we show a cartoon of the collected optical image with inherent aberrations, AFM and the corrected image (Image modified *from ref.* [191]). Second row depicts the direct overlay software, which calibrates the pictures and makes a grid automatically. The panel b shows the reflection images made on a 30 µm x 30 µm of optical field of view by moving the tip in 25 µm x25 µm regions in order to calibrate this area using 9 points as shown.

Direct overlay requires an image calibration file created for an objective and field-of-view from an image sequence of AFM movements. In detail, this overlay image is a grid of at least 9 points which nonlinearly shifts, rotates and stretches the optical image to correct for all possible optical aberrations. The AFM software makes this grid from sequential reflection images of the tip's actual movement in specific piezo positions with a finite pixilation and scan size. The grid has been done for a 30 *µm* x 30 *µm,* shown in *Figure 3.6b* and the AFM software visualizes the respective overlay of AFM images on 25 *µm* x 25 µm inside this calibrated area.

The correlative images and the level of co-localization between AFM and optical images is calculated by using the colocalization function of ImageJ (Bethesda, USA)[198,199] and deriving the ratio of colocalization. An example is shown in *Figure 3.7*. In particular, the Colocalization Threshold plugin was employed. The threshold was automatically determined by the software, by using the Costes autothreshold method[200].

All the correlative images of insulin samples were acquired in liquid working in tapping mode. The AFM/STED images on Aβ samples were performed in air.

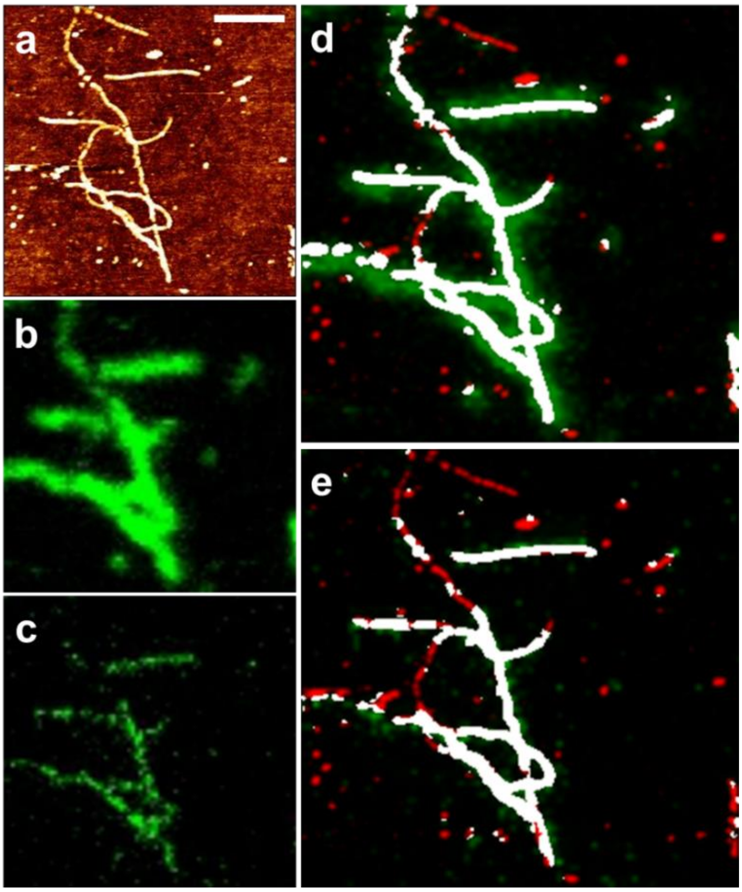

Figure 3.7 | Insulin fibril 1:19 dye-to-protein ratio. AFM (a), Confocal (b) and STED (c) were analysed by using the Colocalization function by ImageJ (NIH, Bethesda, MD, USA). The ratio of colocalization is the ratio between the number of colocalized pixels (white pixels in d and e) and the total number of pixel that composed the fibrils in the AFM images.

Chapter 4
Characterization of misfolded protein aggregates by AFM/STED correlative microscopy

4.1 Amyloid fibrils from Insulin

In this study, as it was already said, bovine insulin has been chosen since the structure of insulin fibrils is well known, as well as the number of monomers that are present in a unit length of an insulin fibril[130].

Aggregation kinetic was monitored by means ThT assay, to support AFM data. Numerous studies have been performed to investigate the physico-chemical and spectroscopic properties of ThT upon binding and it's the binding mechanism[201]. Nielson et al. reported that ThT did not affect the kinetics of insulin fibril formation at 60°C[124], but other study suggest 'increasing the ThT concentration results in a slightly slower fibrillation process'[202]. Xue et al. compared β2-microglobulin fibrillation in the presence and absence of ThT and concluded that ThT has no significant effects on β2-microglobulin aggregation[203]. Regarding $A\beta_{1\text{-}40}$ aggregation experiments, D'Amico et al. suggest that ThT promotes $A\beta_{1\text{-}40}$ aggregation[201]. All these studies reported above and others, showing as the changing, in the presence of ThT molecules, during the amyloid formation process are concentration-dependent and different for protein species[44].

The AFM is considered a primary technique in the study of amyloid fibrils and aggregates in vitro, taking advantages of label-free ability, and it has been extensively utilized in the last decade[195,204–206]. The greatest achievement of the AFM is the possibility to study proteins in different environments and enabling the visualization of dynamic events like the nucleation and fibril formation and aggregation. The AFM can take images in solution at distinct time points as well as generating time-lapse images about the initial steps of amyloid formation like seed formation and about growing fibrils and about the development of matured aggregates. With this technique is possible to study the rates of fibrillogenesis, as well as mapping the progression of variations in morphologies and the development of structural hierarchy. Furthermore, events can be studied under conditions close to the native physiological state[207].

In the last decade a new class of far-field microscopy, SR optical microscopy, described in chapter 2, gave new impetus to the investigation of nanometric structure, e.g. amyloid aggregates[94,208–210,]. SR techniques are fluorescence microscopy modes, based on the use of fluorescent molecules. Ideal molecular dyes must provide high specificity, brightness, and stability. While the two former properties are mostly related to the molecular structure of the fluorochrome itself, the specificity depends on the method used to recognize and bind a particular molecular target[211]. Furthermore, the influence of the fluorescent dye on the biological processes under investigation should be minimal. In particular, covalent fluorescent labeling is a procedure commonly applied in vitro[212]. The fluorophores employed for covalent labeling are small molecules (<1kDa) and are widely used in the study of dynamic processes of inter-molecular interaction. In spite of this, previous reports highlighted that covalent linkage of fluorophores can affect the visualization, dynamics and/or biological properties of molecular system[213–215]. However, it is not trivial to have a direct and unambiguous assessment of the efficiency and homogeneity of the labeling, as well as on the influence that the fluorescent tag has on the molecular activity.

The work described here as well as the one illustrated in the next chapter is addressed on the correlation of SR fluorescence microscopy and label-free AFM as a means to study the aggregation process of a non-pathological protein, insulin from the bovine pancreas covalently labeled with NHS-dye fluorophore. These results demonstrate that the integration of AFM with super resolution fluorescence microscopy can be used to validate the results deriving from fluorescence microscopy, but also to highlight important features on molecular processes.

4.1.1 – Insulin fibrillation Kinetics

Variations of ThT fluorescence signal over time from insulin solution containing ThT at 100 Mm concentration were measured, displaying a sigmoidal behaviour which is typical of amyloid aggregation kinetics for insulin samples in analogous conditions (*Figure 4.1*). The twofold molar excess of ThT is used to ensure saturation of the binding sites.

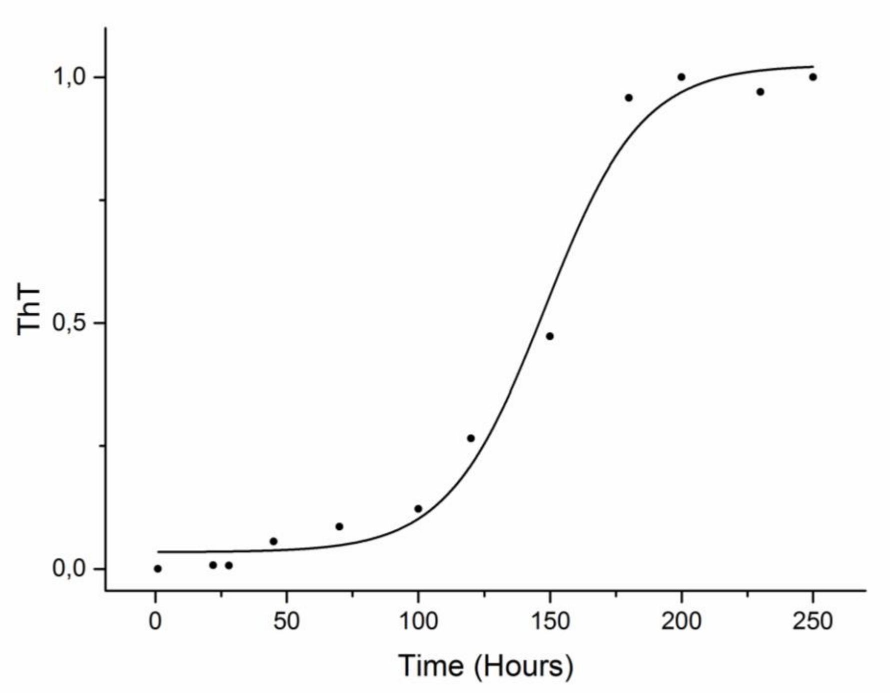

Figure 4.1 | Thioflavin t kinetic. Time course aggregation of a 50 µM solution of insulin at 60 °C, monitored by ThT fluorescence increase (ThT 100 µM). Emission wavelength: range 470-540 nm; excitation wavelength: 450 nm; slit width: 1nm. Aliquots of 50 µL of solution were taken away at different time processes. The points indicate the aliquots extracted in time and the corresponding ThT normalized value.

ThT data show the three main steps occurring in the fibrillation process. As it is evident, lag phase lasts for about four days followed by an elongation phase that reaches the plateau in eight days.

Aliquots of insulin-HCl solution were taken at different times to be investigated by AFM, and stored at 4 °C in order to slow down the aggregation process. Concentration and temperature are the two parameters that influence the rate of fibrillation. Five aliquots were extracted during the lag-phase, lasted four days, in which prefibrillar aggregates and few small protofibrils are formed.

The other two aliquots correspond, respectively, to the elongation phase, in which protofibrils grow, and to the final plateau, characterized by the presence of mature fibrils. Repeatability of the sigmoidal behaviour has been verified by conducting a triplicate monitoring of the aggregation process.

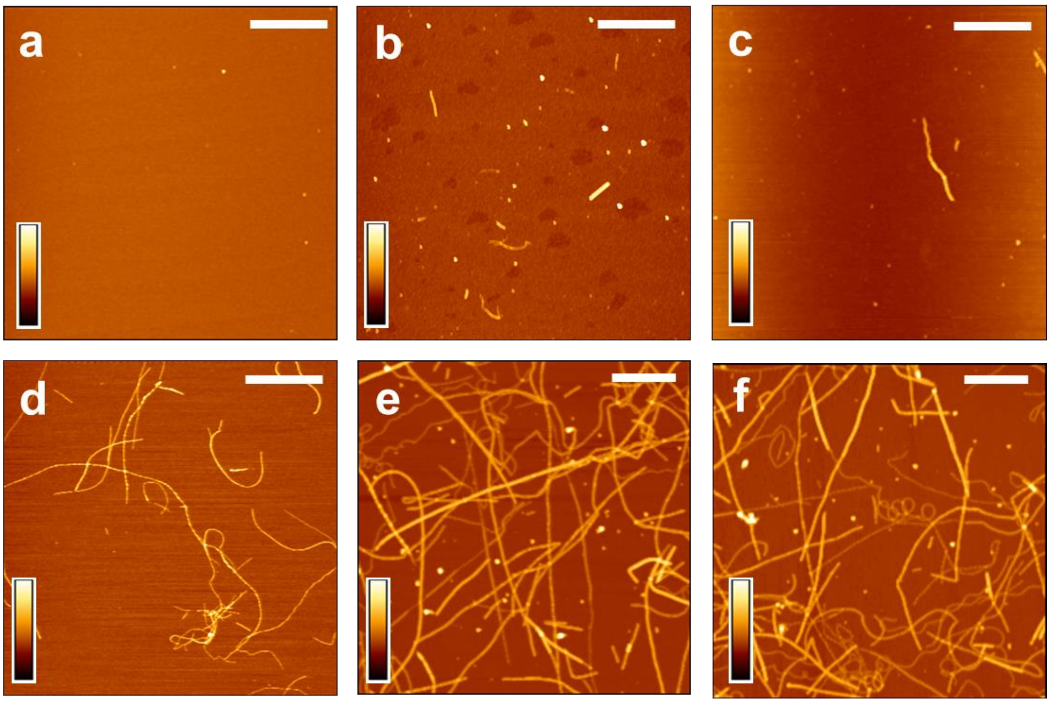

Figure 4.2 | AFM images of unlabeled insulin aggregated species sampled at different instant of kinetic and desiccated on mica. a: t= 0; b: t= 3 days; c: 4 days; d: t = 6 days; e: t= 12 days; f: t= 14 days . Scale bars a-f: 2 µm. Z-range 7 nm (a, b, c), 15nm (d, e, f).

4.1.2 – AFM characterization of *label-free* Insulin aggregates

AFM was used as a consolidated technique to follow the aggregation of insulin and to characterize the morphology of the fibrils. Insulin solution was diluted 100 times with deionized water, 20 µl aliquots were deposited on freshly cleaved mica substrate for AFM measurement. As reported in the sample preparation section the dilution of the samples with water immediately quenches the aggregation process, and the dry conditions prevents further unspecific aggregation. The corresponding topographies are shown in *Figure 4.2*. At the beginning of the lag-phase (time 0 – *Figure 4.2* a) only small species are present, sizing few tens nanometers with a thickness (height) of less than 1 nm. As aggregation goes on (time 3 days – *Figure 4.2 b*), larger globular aggregates and few protofibrils form, characterized by a lateral size ranging from 20 to 80 nm and a thickness of few nanometers. The elongation start in 4 days of incubation (*Figure 4.2 c*), a few small fibrils are present, with a length ranging from 500 nm to 2 µm and around 5 nm in thickness. In this part of fibrillation, short fibrils replaced prefibrillar aggregates.

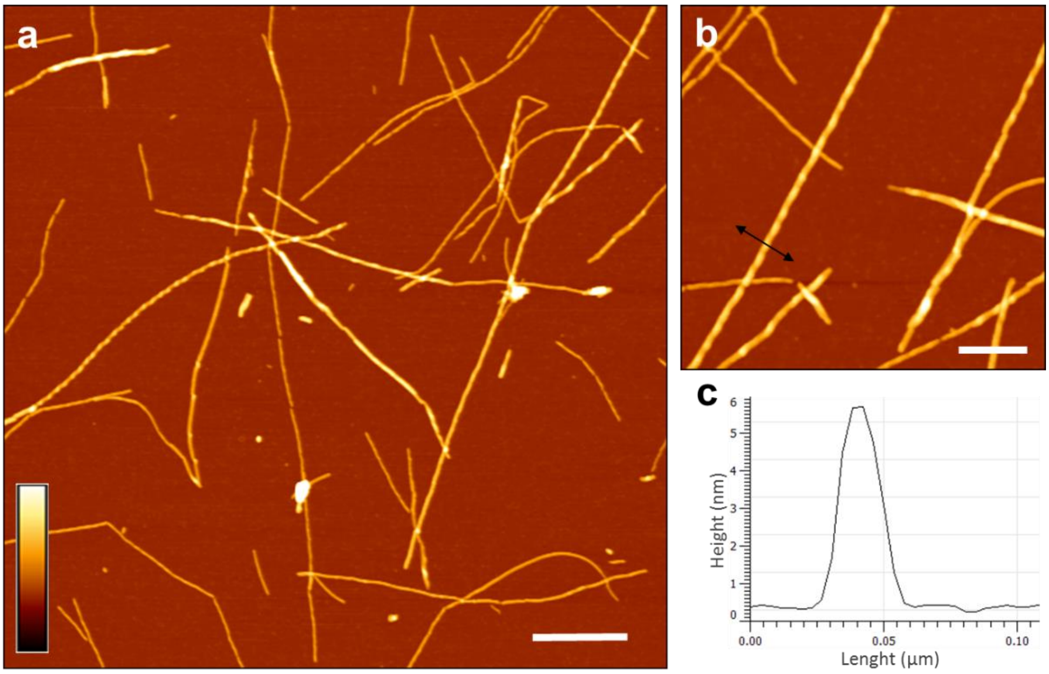

Figure 4.3 | AFM image of mature insulin fibrils. (a) Overview of preformed insulin in water diluted 100 times (scale bar: 500 nm). (b) Details of structure (scale bar: 200 nm) and (c) relative profile. Z-range: 15 nm.

The amount of fibrils increase during the elongation step (*Figure 4.2 d, e*). Mature fibrils appear in the last part of the kinetics (*Figure 4.2 f*). The process reaches equilibrium when most soluble proteins are converted into fibrils, in terms of ThT-kinetic is referred to the last part of the elongation phase. The AFM images show mature fibrils with a length of several microns and a relatively small diameter. In the lateral dimension, the fibrils show a variable size, ranging from 30 to 80 nm. Unlabeled fibrils have a height of 5.6±1.7 nm. AFM images support morphologically the general properties of amyloid insulin structure. In *Figure 4.3,* an investigation at a larger resolution of mature fibrils to highlight characteristic features slightly evident in fig. 4.2 e and f.

In *Figure 4.3a* is clearly noticeable some characteristic traits of the mature amyloid fibrils, i.e. the tendencies to bend, twist, and agglomerate. Moreover, in *Figure 4.3b* is visible the classical helix structure: parallel tubular fibers, twisted ribbon like structures[60].

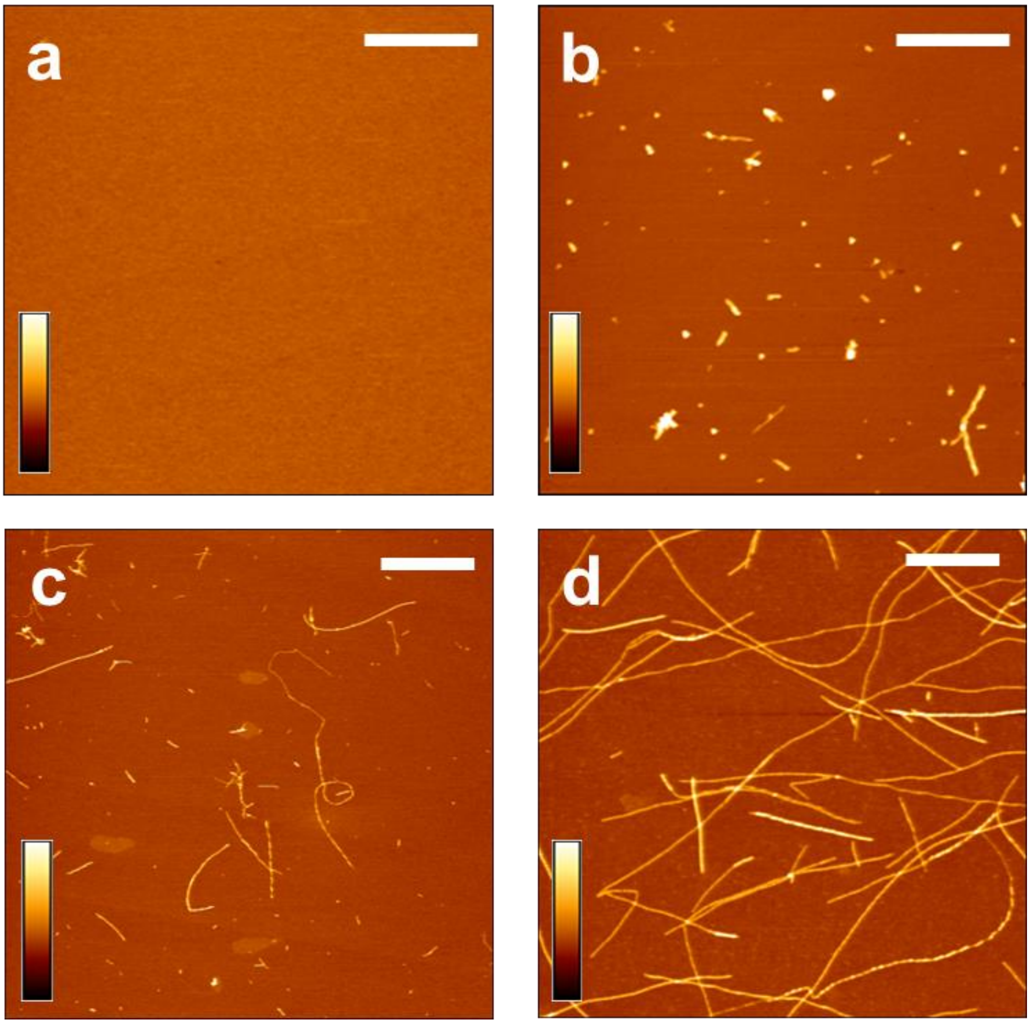

Figure 4.4 | ATTO 488-Insulin 1:19 dye to protein ratio aggregated by AFM. The images sampled at different instant of kinetic: (a) 0 day, (b) 6days, (c) 12days (d) 14days. Scale bar: 2 µm. Z-range: 7 nm (a, b), 15nm (c, d).

4.1.3 - AFM characterization of ATTO 488-Insulin aggregates

ATTO 488 with NHS-esters, for coupling to primary amines on the proteins, has been used. Monomeric bovine Insulin present three possible -NHS binding site exposed from the structure, two of which concern the strands N-terminus and one from a Lysine group on the B-chain.

The hydrophilic nature of ATTO labels minimizes the risk of interference with the protein polymer self-assembly[216]. Labelling was done preferentially at the N- terminus by means of a judicious choice of the reaction pH, using phosphate buffer, as described in Methods section. Moreover, in order to have an optimal labeling ratio for SR technique, the different ratio between the fractions of labeled relative to unlabeled protein were used. Higher labeling density would compromise resolution[217] and mainly might potentially lead to steric interferences of the dye with the fibrils.

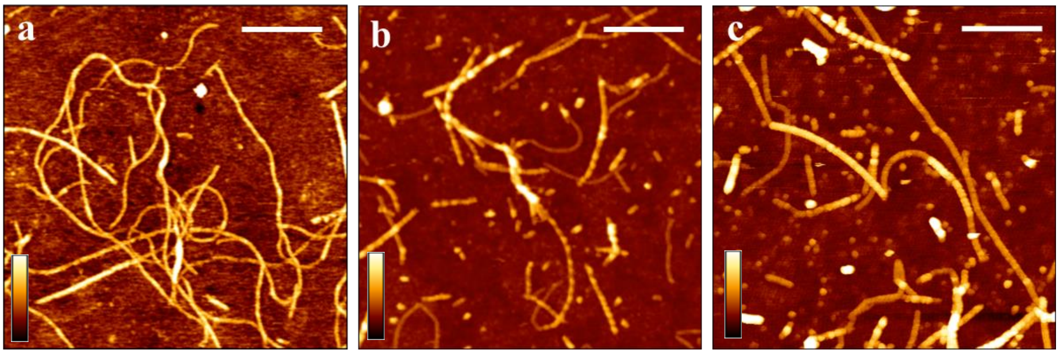

Figure 4.5 | Insulin aggregation in three dye to protein ratio. AFM images performed after 10 days incubation in denaturing conditions. (a) 1:19, (b) 1:99, (c) 1:499. Scale bar: 1 µm. Z-range: 10 nm

Three dye to protein ratio (i.e., labeled:unlabeled insulin) were tested: 1:19, 1:99 and 1:499. AFM was used to characterize morphologically the formed structure and to verify that the presence of the dye was not precluding then formation of the fibrillary aggregates. Following the procedure described previously, few microliter of 1:19 labelled insulin was imaged at 0, 6, 12, 14 days of incubation time (*Figure 4.4*). A large number of long unlabelled insulin fibrils (with a thickness of 5.6±1.7 nm) at time 6 days (as is shown in *Figure 4.2d*) are displayed. However, AFM image of 1:19 labelled insulin sample at the same time *(Figure 4.4b)* reveal the presence of larger globular aggregates and small protofibrils. At the concentration considered, the kinetics of aggregation appear slightly delayed by the presence of the fraction of labelled monomers.

Fibrils have a variable length, and the thickness is slightly affected by the presence of the dye. In *Figure 4.5* are shown, in sequence, the morphologies of the three different concentrations. In particular, the mean thickness are: 6.3±2.7 nm for 1:19 samples (*Figure 4.6*), 7.5±2.5 nm for 1:99 and 7.6±2.5 nm for 1:499. In lateral dimension is possible to observe ranging from 50 to 100 nm. On the other hand, the apparent lateral dimension of all AFM-imaged objects are overestimated as a result of the influence of the geometry of the probe tip, with a finite size, that is in the same order that a protein molecule[218,219]. The knowledge of the approaches in both measurement and data analysis when using AFM technique are essential for the correct interpretation of surface topographic features.

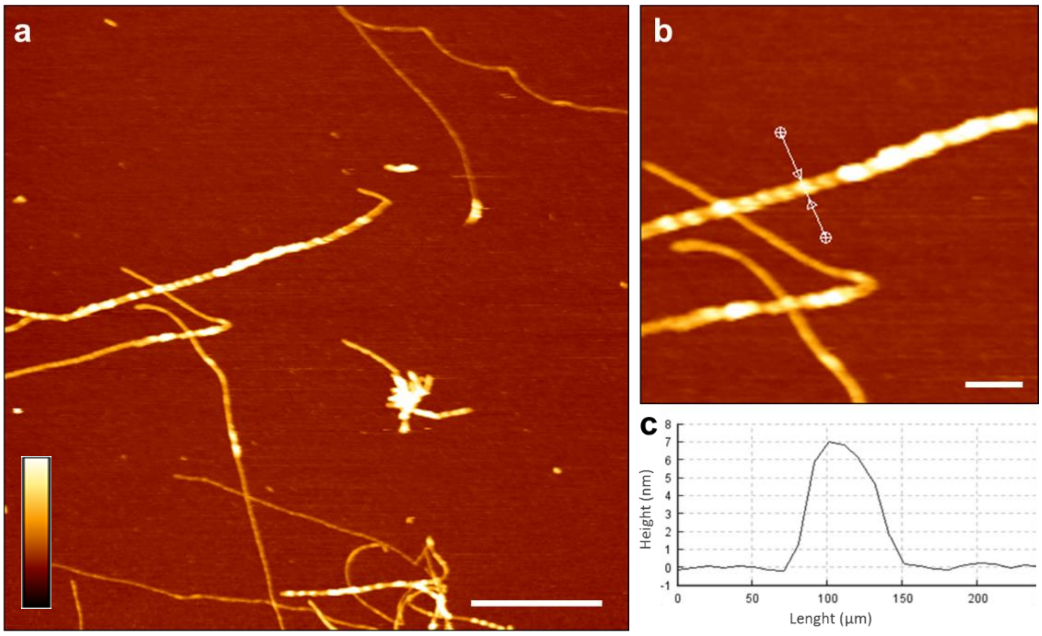

Figure 4.6 | AFM image of mature insulin fibrils labeled 1:19. (a) Overview of preformed insulin in water diluted 100 times (scale bar: 1 μm). (b) Details of structure (scale bar: 200 nm) and (c) relative profile. (z-range: 10 nm).

A qualitative evaluation of fibrils shape

In this section, I intend to give a brief insight for the characterization of protein aggregates structure via AFM. Concerning to handling details, one of the most important factors to take into account is the AFM tip. In fact, tip geometry can give overestimation the size of the sample, while it does not affect the height measurements. The major effects with regards to tip geometry are those leading surface feature broadening as a result of tip curvature's radius being, in this specific case, larger than the size of features. During the study of fibril morphology, several factors contribute to define the apparent fibril size and shape. In particular, the measured fibril width appears much larger than the real fibril size as a result of, so-called, 'tip-broadening' effects (*Figure 4.7*).

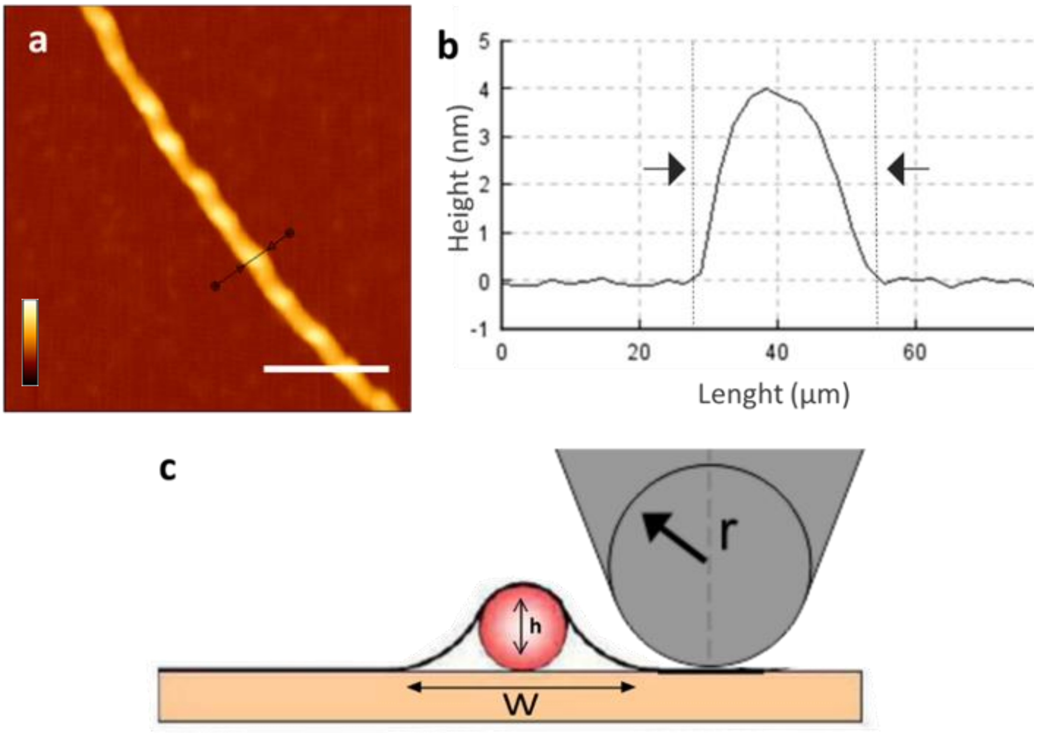

Figure 4.7 | The lateral broadening effect led by the tip size. (a) AFM image in dry condition of insulin fibrils structure (Scale bar: 100 nm. Z-range: 10 nm). (b) The profile cross-section indicate a height of 4 nm and a length of 30 nm. (c) Schematization of broadening effect in AFM image due to tip size effect.

Here we roughly consider the fibrils structure as a cylinder, with a circular cross-section, therefore the apparent width (*W'*) is related to the height (*h*) according to the equation,

$$W' = \sqrt{8Rh}$$

,where R is the radius of curvature of the tip and *h* the measured thickness[220]. With the values of height above reported and considering the nominal R of the tip employed in this work we found that insulin fibrils are significantly flattened, likely due to the interaction and binding at the substrate.

In particular, the mean value of *W/W'*, where *W* is the measured fibril width, is 1.7±0.5 in 1:19 samples, 2.6±0.6 in 1:99, 2±1.1 in 1:499, and 1.5±0.4 in *label-free* insulin.

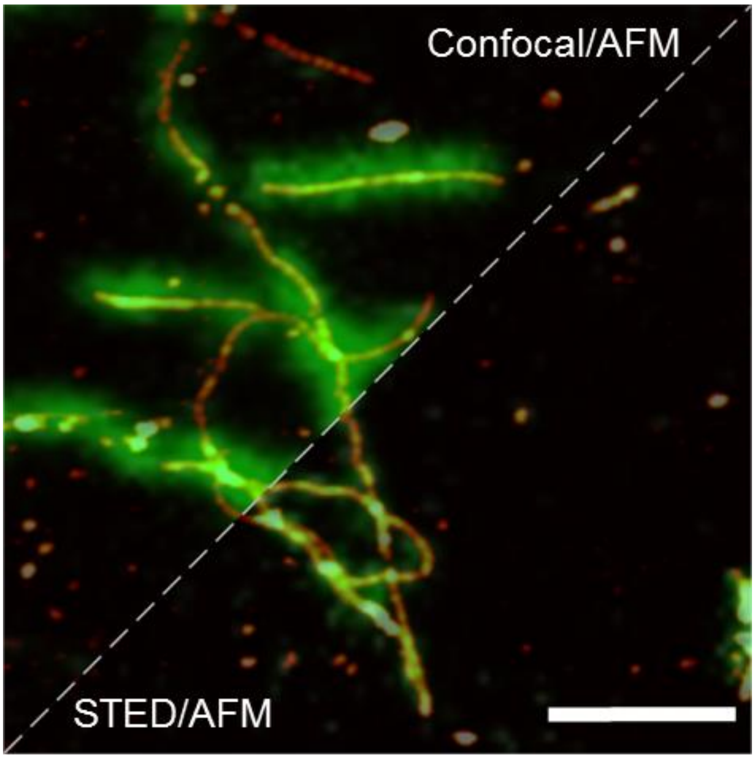

Figure 4.8 | Correlative technique on amyloid fibrils from bovine insulin in 1:19 dye-to-protein ratio. The STED and Confocal images are overlaid with AFM topography. Scale bar: 1 µm.

4.1.4 - AFM/STED on Insulin aggregates

Correlative AFM/STED technique has been applied in the study of mature fibrils, i.e., aggregates after 14 days of incubation in denaturating conditions.

In *Figure 4.8* is shown an example of image obtained consecutively by techniques on the same scan area, highlighting the difference between conventional confocal microscopy (in green above) and STED microscopy (in green below), and showing the overlap with AFM (red hot colour).

The resolution of the STED microscopy image is significantly enhanced with respect to the confocal microscopy image. The fibrillar aggregates at the three different dye to protein ratio (called 1:19, 1:99, 1:499 in the following) were imaged, following the procedure described in the Methods section.

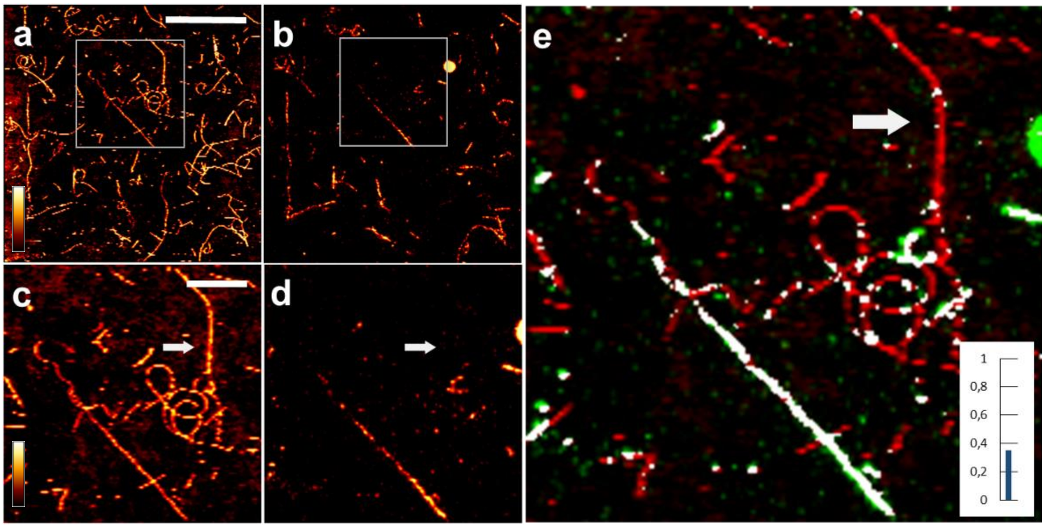

Figure 4.9 | ATTO 488-Insulin fibrils 1:19 images. AFM (a, c), STED microscopy (b, d) and the correlative images obtained by c and d (e). The ratio of co-localization in this particular field of view is indicated by the histogram (inset e). Scale bars: (a, b) 5 µm, (c-e) 2 µm. Z-range: (a, c) 5 nm.

SR fluorescence images acquired on the 1:19 sample (*Figure 4.9 b, d*) show a significant presence of unlabeled fibrils, detectable only by using AFM (*Figure 4.9 a, c*). Only a fraction of the fibrillar aggregates is displayed in the optical image. In particular, some long fibrils are completely missing (white arrow in *figure 4.9)*, indicating that the labeled monomers were not taking part in the formation of this aggregates. In addition, a heterogeneous distribution of the dye-insulin molecules led to the formation of two other species: aggregate entirely fluorescent (continuous distribution of fluorophores) and aggregate not homogenous fluorescent (discontinuous distribution of fluorophores).

Fibrils in which the distribution of the fluorophore is discontinuous (white arrow in *Figure 4.10*) have a homogeneous thickness, supporting the idea of a regular distribution of protofilaments along the fibrils and, roughly, a same amount of monomers per unit length along the whole fibril.

The ratio of co-localization between AFM and STED images is 0.25 for this specific field of view. An analysis of 10 images acquire from samples derived from 3 different preparations indicates a value of correlation of 0.42±0.11.

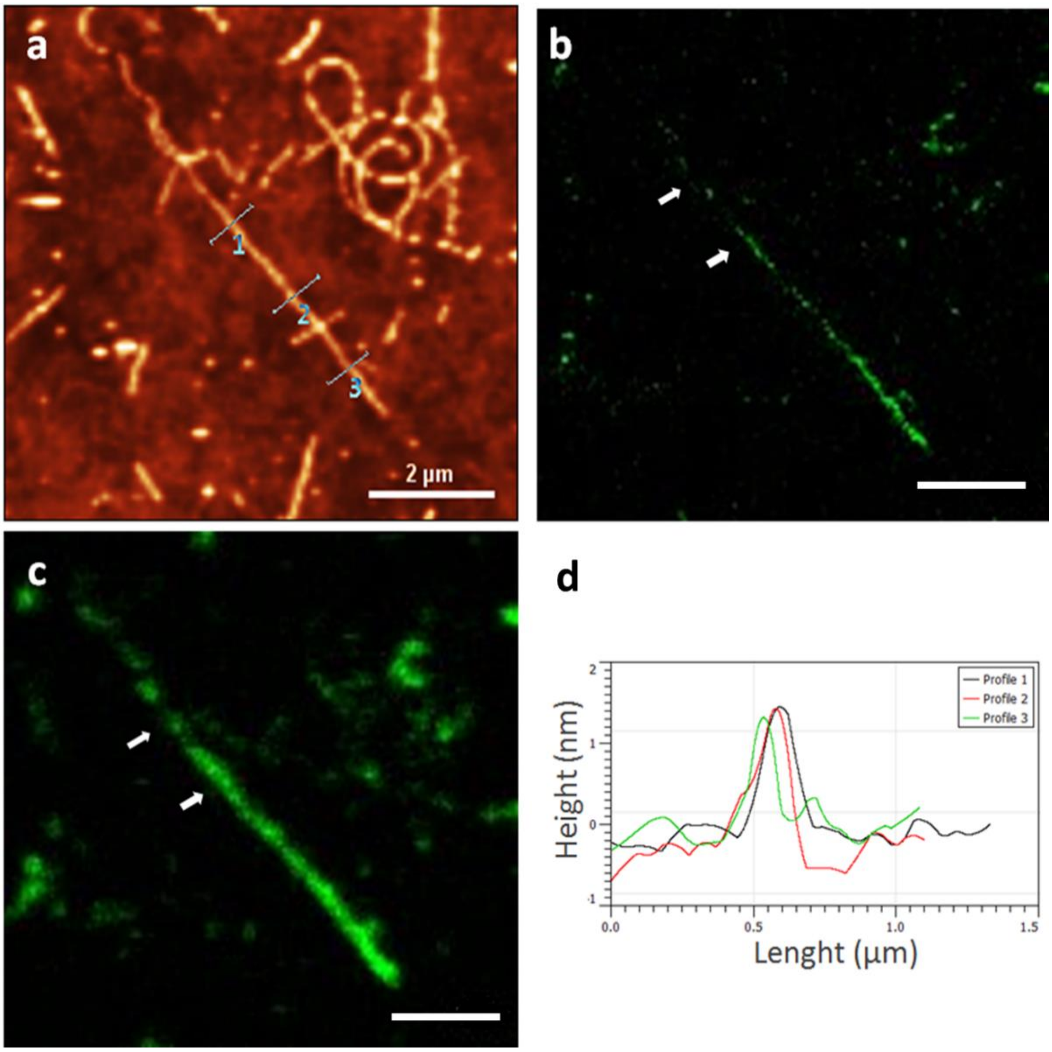

Figure 4.10 | Detail of insulin 1:19 fibrils in AFM (a), STED (b), Confocal (c). (d) AFM profile comparison of the same fibril displayed a not continuous distribution of fluorophore. Optical microscope scale bar 2 µm.

The same experiment was repeated on 1:99 (*Figure 4.11 a-c*) and 1:499 (*Figure 4.11 d-f*) samples - 3 preparations per each sample. As expected, the correlation between the AFM and STED images decreases at lower dye to protein ratio, and the ratio of colocalization is 0.29±0.07 (1:99, n=10) and 0.19±0.09 (1:499, n=10).

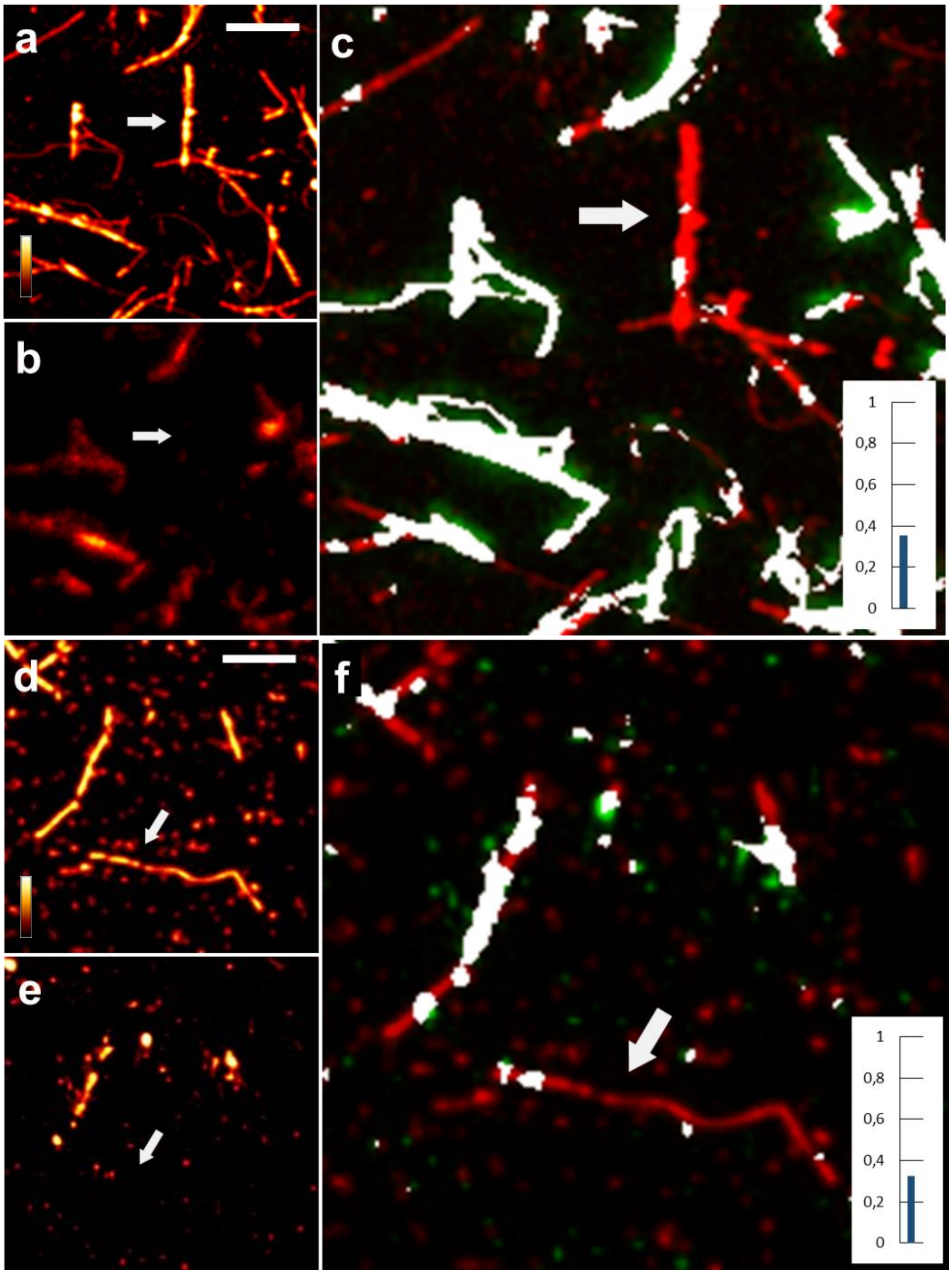

Figure 4.11 | Insulin fibrils obtained from 1:99 (a-c), and 1:499 (d-f) dye to protein ratio. AFM images (a, d), STED microscopy images (b, e) and correlative images obtained by the previous (c, f). Several fibrils are totally unlabeled. This result resembles the one obtained at a dye to protein ratio of 1:19. The ratio of colocalization is shown by the blue bar in the inset. Scale bar: 1 µm. Z-range: (a, d) 10 nm.

4.2 - Characterization of Aβ aggregation

Biophysical techniques can be used to study protein aggregation and give information about, for instance, aggregation kinetics[221,222]. These techniques generally average over a large number of aggregating molecules and cannot be used to read out the length or shape of individual fibrils. On the other hand, high-resolution microscopy methods such as AFM and EM have been applied to studying fibril growth with resolutions lower than 1 nm[60,223,224]. Moreover, SR fluorescence microscopes were applied in the study of the molecular mechanism associated with misfolded protein diseases. In particular, Direct-STORM technique was used to investigate the aggregation of Aβ both in vitro and in situ, offering a useful approach in the study of the morphological differences between the species [217]. By using two-color dSTORM, the polarized elongation of $A\beta_{1\text{-}42}$ fibrils was also demonstrated[225]. Immunolabeled tau filaments from brain sections were imaged with a resolution of 77 nm by using STED microscopy[152]. In a recent study, the preferential localization of γ-secretase in the presynaptic and postsynaptic compartment has been characterized by STORM and STED microscopy[226]. In the field of Parkinson's disease, amyloid fibrils from α-synuclein were imaged with an unprecedented resolution by using binding-activated localization microscopy (BALM)[227]. Two-color d-STORM has been employed to study the elongation of preformed α-synuclein fibrils, providing new insights into the role of seeding in the fibrillogenesis[228]. Finally, the fibrillation of human lysozyme, involved in a fatal form of hereditary systemic amyloidosis was characterized in details[229].

The molecular mechanism involved in cross-β structure proteins aggregation into fibrillar structures is nowadays an open question. In-depth analysis of the dynamics of these processes can lead to a better understanding of the cause of these diseases and assist progress in the search for therapeutic intervention[230].

The workplan of this section is to use of the correlative technique AFM-STED, to analyze the eventual affection induced by the presence of a fraction of fluorescent Aβ molecules on the aggregation process. We used a largely employed fluorescent Aβ and together well established protocols for protein aggregation[31].

4.2.1 – Aβ fibrillation Kinetics

$A\beta_{1-42}$ and $A\beta_{1-40}$ aggregation kinetics was investigated using ThT assay. Dilution of ThT stock solution was done in PBS buffer at the final concentration of 50 µM and used with 25 µM of Aβ protein at 25°C.

The fluorescence was measured using an excitation of 450 nm and an emission of 482 nm. Aliquots of Aβ-Tht solution, immediately after mixing, were investigated directly by spectrofluorometer over 4 hours. The kinetic course graph in *Figure 4.12,* with the characteristic phase of amyloid aggregation, shows that $A\beta_{1-42}$ is slightly faster than $A\beta_{1-40}$, with a smaller Lag-phase.

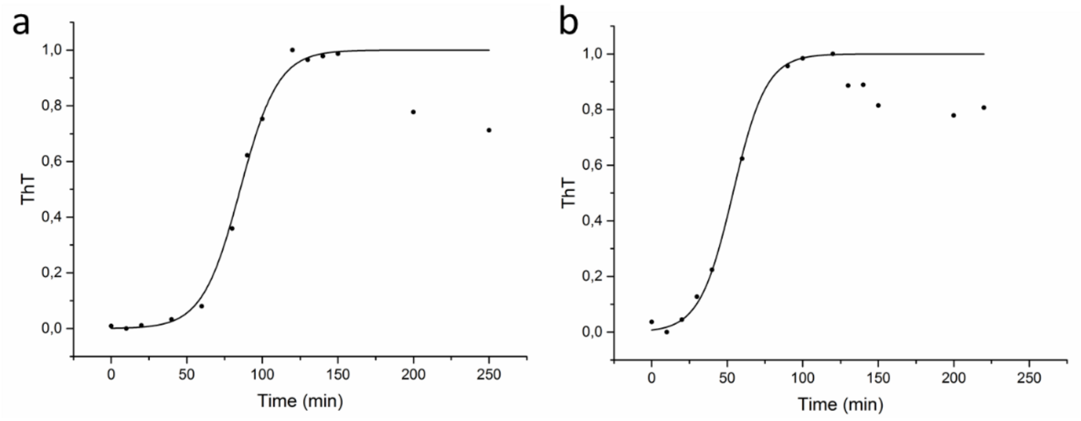

Figure 4.12 | ThT fluorescence intensity kinetics of Aβ. Time course aggregation of a 25 µM solution of $A\beta_{1-40}$ (a) and $A\beta_{1-42}$ (b), monitored by ThT fluorescence increase (ThT concentration was 50 µM). Emission wavelength: 482 nm; excitation wavelength: 450 nm; slit width: 1nm.

4.2.2 - AFM characterization of $A\beta_{1-42}$ and $A\beta_{1-40}$ fibrillar aggregates

The aggregation of $A\beta_{1-42}$ was induced using standard protocol proposed in the literature[31,194] and described in Chapter 3. The characterization of the initial state of the aggregation was made to exclude the presence of pre-existent fibrillar aggregates that could induce important artefact in the analysis.

AFM images acquired just after the resuspension of the lyophilized peptide in the aggregation medium are shown in *Figure 4.13* and are indicating the presence of a monodisperse distribution of globular aggregates.

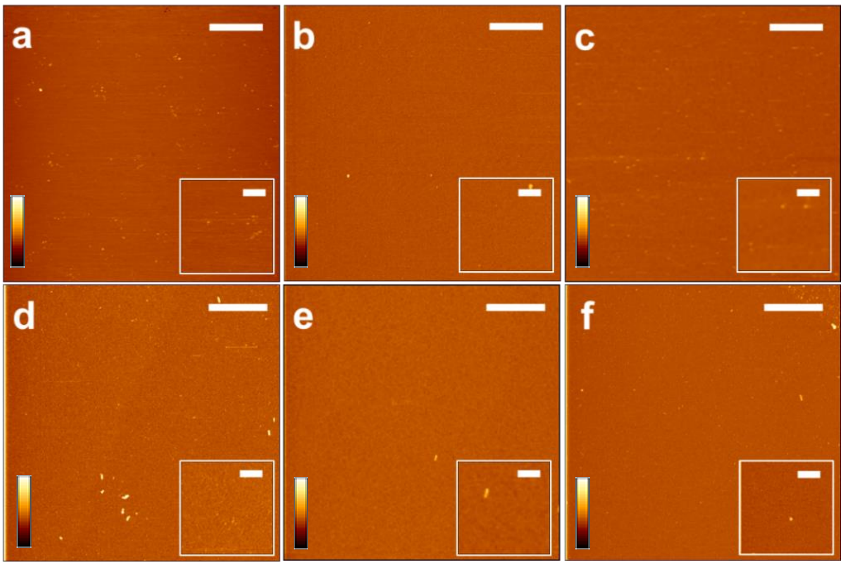

Figure 4.13 | AFM images of amyloid-β peptides just after resuspension of the lyophilized peptide in the aggregation medium. A$\beta_{1\text{-}42}$ (a) unlabeled, (b) 1:19, (c) 1:99, (d) 1:499. A$\beta_{1\text{-}40}$ (e) unlabeled and (f) 1:19. Scale bar: 1 µm. Z-range: 10 nm. Insets scale bars: 200 nm. Prefibrillar aggregates are not present at the beginning of the aggregation process.

The dynamic light scattering (DLS) confirm the data with a mean size for A$\beta_{1\text{-}42}$ of 2.0±0.4 nm and for A$\beta_{1\text{-}40}$ of 2.4±0.3 nm.

AFM images support ThT measurement, after 1 day of aggregation the fibrillar proteins are present (*Figure 4.14*) and completely formed in branched fibrils.

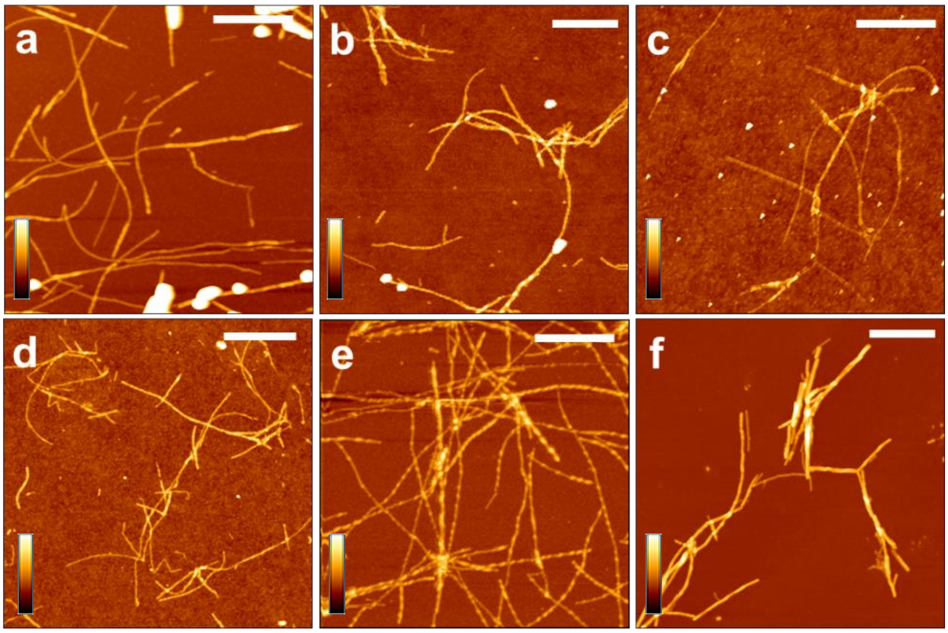

Figure 4.14 | Amyloid β fibrils. AFM was used to follow the aggregation of Aβ_{1-42} and to characterize the morphology of the fibrils after 1 day of aggregation. (a) Unlabeled, (b) 1:19, (c) 1:99, (d) 1:499. Aβ_{1-40} (e) unlabeled and (f) 1:19. Scale bar: 1 µm. Z-range: (a) 10 nm, (b, c, d, e, f) 20nm.

4.2.3 - AFM/STED on Aβ_{1-42} and Aβ_{1-40} aggregates

The well-established correlative method tested on insulin aggregation, has highlighted a new and important scenario about aggregation studies. In order to have a more general view and to extend the result to a pathological peptide synthetic Aβ_{1-42}/Aβ_{1-40}-HiLyte Fluor 488 (HF488) has been used. Correlative AFM/STED technique has been applied on mature fibrils, i.e., aggregates after 1 day of incubation at 37°C. Following the same procedure explained for insulin, the HF488-aggregates was investigated in three different ratios between the fractions of labeled relative to unlabeled protein: 1:19, 1:99, 1:499. The correlative images indicated the presence of different types of aggregates (*Figure 4.15*); with a significant unlabeled fraction of fibrils already present at a dye to protein ratio of 1:19 (*Figure 4.15 a-c*). The correlation between AFM and STED images, i.e., the population of fibrils that are visible in fluorescence microscopy, decreases at lower dye to protein ratio: 0.45±0.13 (1:19), 0.26±0.11 (1:99), and 0.16±0.04 (1:499).

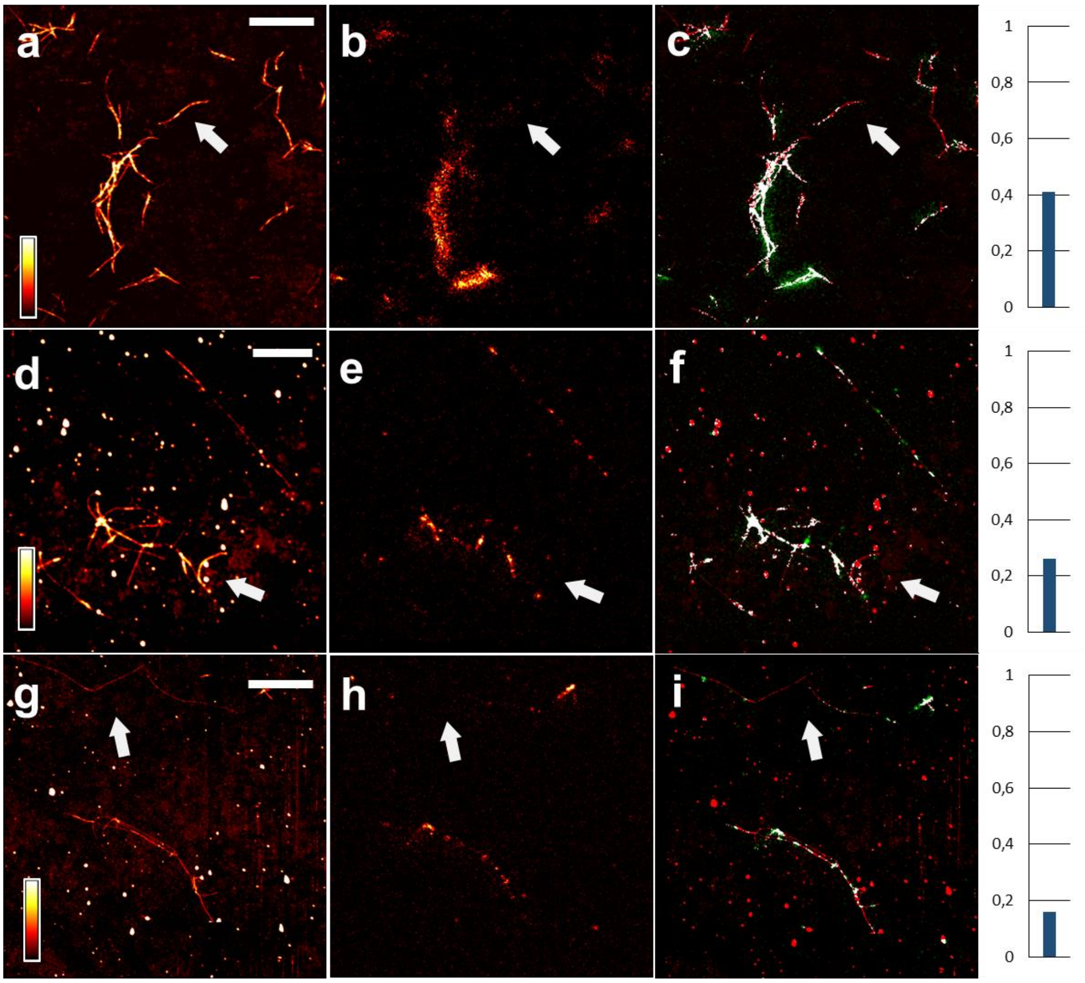

Figure 4.15 | Amyloid aggregates from HF488 Aβ_{1-42}. Different concentrations of fluorescent peptides were present. The dye to protein ratios are (a-c) 1:19, (d-f) 1:99, (g-I) 1:499. Also at the higher dye to protein ratio (a-c) some fibrils were not displayed by fluorescence images (e.g., see the withe arrows). Scale bar 2 µm. Z-Range (a, g) 10 nm, (d) 5 nm. Overlay graph on the right.

These results, derived from two different preparations, and from a total number of 15 images per each sample, are summarized in discussion section (*Table 4.1)*. Furthermore, these results have been confirmed on HF488 Aβ_{1-40}, analysing 22 different images from two different preparations at 1:19 dye-to-protein ratio. The presence of a significant population of unlabeled fibrils is evident in *Figure 4.16 a-c*.

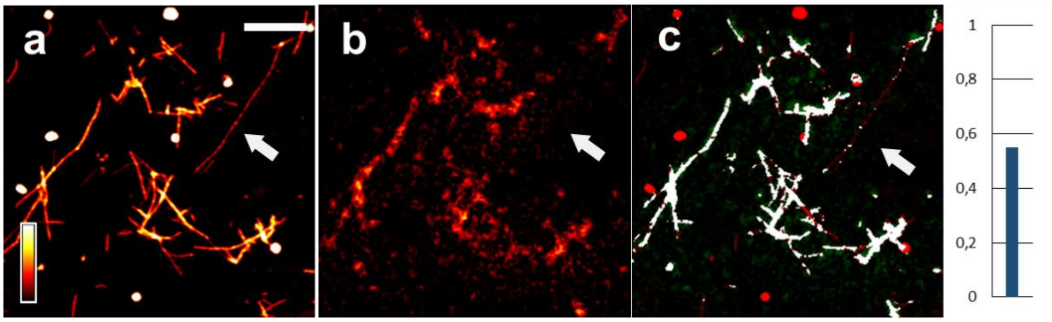

Figure 4.16 | AFM/STED on HF488 Aβ_{1-40} aggregates. Fibril imaged by AFM (a) and STED (b). The overlapped image (c) in which the green color represent STED fibrils, red color AFM fibrils and in white color the ratio of co-localization. The dye to protein ratio is 1:19. Scale bar 2 µm. Z-Range (a) 10 nm.

4.2.4 - Characterization of immunolabeled Aβ_{1-42} aggregates

Amyloid fibrils from Aβ_{1-42} were labeled via indirect immunolabeling, following a well-established procedure (See Chapter 3). After the conjugation with the fluorescent secondary antibody, we found that all the fibrillar aggregates displayed by AFM were also visible in the STED image. As a consequence of this, the correlation between the AFM and STED images (*Figure 4.17*) is very high for all the images acquired (n=12) and for the two preparations.

The level of co-localization between AFM and STED images has been quantified to 0.92±0.05. The typical cross-section of the fibrils, measured by AFM (*Figure 4.17 a, d*), is significantly increased as a consequence of a massive binding of antibody molecules at the fibril surface, with a mean height value of 20.4±7 nm. This indirect proof of the presence of the molecular dyes is a final example of the potentialities that are opened by the use of a correlative technique in the study of intermolecular interaction.

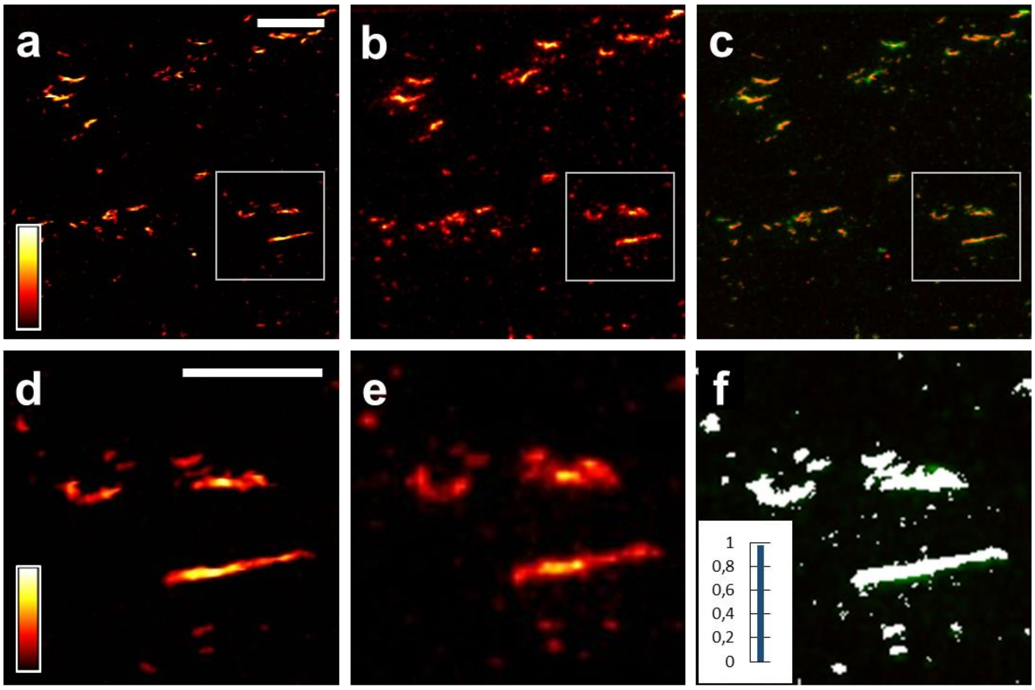

Figure 4.17 | Amyloid aggregates formed from Aβ$_{1-42}$ in the absence of fluorescent monomers and subsequently labelled via indirect immunolabeling. All the features displayed in the AFM images (a, d) are also visible in the STED images (b, e) and are colocalized (c, f). Interestingly, the fibrils size, measured by AFM, is larger with respect to the unlabeled fibrils, confirming the presence of a large amount of antibody on the fibrillar aggregates. Scale bar (a-c) 2 µm, (d-f) 1 µm. Z-range (a, b) 30 nm. Inset (f) graph of co-localization

4.3 - Discussion

Amyloid aggregates derived from insulin and two different alloforms of β-amyloid peptides, Aβ$_{1-42}$, and Aβ$_{1-40}$ were images by correlative AFM-STED microscopy. The aggregation started from solutions of mixed unlabeled and labeled proteins/peptides at different dye to protein ratio (1:19, 1:99, 1:499). The dye to protein ratio of 1:19 was chosen following well established methods and largely employed[231–233], while 1:99 and 1:499 were used as a control, in order to evaluate how the presence of fluorescent aggregates rescale with the concentration of the dye. Insulin was labeled by covalently binding a fluorophore at the free amine groups, while fluorescent Aβ$_{1-42}$ and Aβ$_{1-40}$ presented a single fluorophore at a terminal group and was purchased by an external company. In both the cases, we found that, at all the three dye to protein ratio under investigation, fluorescent fibrils coexist with a significant fraction of aggregates that are mainly, or entirely unlabeled.

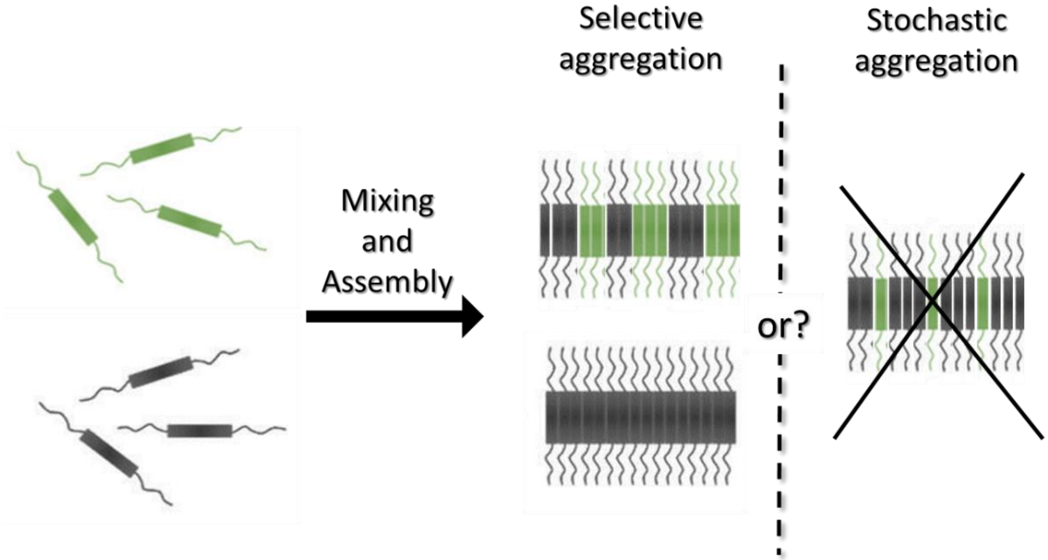

Figure 4.18 | A stochastic aggregation of the labeled/unlabeled peptides should bring to the formation of uniformly labeled fibrils. Our experiments indicate a different scenario where just a fraction of the fibrils has a labeled component. Other fibrils, dark in the STED analysis, are unlabeled. These two products are the results of different aggregation pathways. The correlative technique here employed gives an answer to the above question.

Insulin from the bovine pancreas is not an amyloidogenic protein in vivo. In particular, we chose insulin since the structure of insulin fibrils is well known, as well as the number of monomers that are present in a unit length of an insulin fibril[130] . From Small Angle Scattering experiments, it was calculated that an insulin fibrils with a circular cross-section of 6 nm in diameter is formed by 7 protofilaments and the number of monomer per unit length was calculated. Comparing this model with the morphological features of our insulin fibrils (average thickness and aspect ratio is reported in Insulin section) and with the assumption of an indistinct aggregation - in which fibrils are the result of the stochastic assembly of labeled and unlabeled monomers - we deduce that at least 1 labeled molecules every ~ 6 nm along the fibril axis must be expected in 1:19 samples, 1 every 30 nm in 1:99 samples and 1 every 150 nm in 1:499 samples. Considering this rough estimation, if the labeled monomers take part to the aggregation process stochastically, considering the resolution achieved in our experimental conditions, the fibrils must appear homogeneously and entirely fluorescent upon STED microscopy visualization, at least in the case of 1:19 and 1:99 samples (*Figures 4.9, 4.11a-c*). The presence of a large population of unlabeled fibrils indicates the coexistence of distinct aggregation pathways, some of them allow the contribution of the labeled peptide in the formation of aggregates, and the others preclude this contribution (*Figure 4.18*).

The presence of directly labeled monomers is not only slowing the kinetics of the aggregation of insulin, but is favoring the coexistence of the different aggregation pathways bringing to two distinct final products: labelled and unlabeled fibrils. We pointed out that the presence of these two species of aggregates can be evinced only by applying a couple AFM-fluorescence microscopy correlative technique, but we also noted that only super-resolution microscopy is providing the sufficient capability of discerning between different filaments that are tightly packed in a confined space.

The same procedure has been applied to the Alzheimer's associated peptides A$\beta_{1\text{-}42}$ and A$\beta_{1\text{-}40}$, demonstrating that the phenomenon described in details for insulin is general in the process of aggregation of misfolded proteins. Furthermore, unlabeled aggregates are present also when the peptides are labeled with a single dye at the N-terminus, a part of the polypeptide chain that has been classically considered as scarcely relevant in fibrillation processes[225,233]. In *Table 4.1,* an overview of the data obtained for the different peptide species and dye to protein ratios. The colocalization values (the ratio between the number of co-localized pixels and the total number of pixel that composed the fibrils in the AFM images) show a lower amount over the decreasing of the dye, how we expected, but also very similar values among the different species for each concentration. Suggesting a similar behavior in the aggregation process in presence of the dye molecule of insulin and Aβ peptides.

By using a standard indirect immunolabeling method, we have been able to display the entire population of fibrils within the sample, demonstrating that the loss of information evinced from directly labeled samples is not related to an instrumental limit, but is inherently related to the sample properties.

Table 4.1 | The ratio of colocalization calculated for the different peptide species and dye to protein ratios.

Insulin	Aβ 1-42	Aβ 1-40	
0.42±0.11	0.45±0.13	0.47±0.04	**1:19**
0.29±0.07	0.26±0.11	-	**1:99**
0.19±0.09	0.16±0.04	-	**1:499**

As a whole, these results indicate that the integration between AFM and super-resolution fluorescence microscopy represents not only a complement but a fundamental tool to validate the results deriving from fluorescence microscopy, and that it can drive the experiments towards more accurate and less invasive methods of labeling. AFM-STED microscopy could be a fundamental test in the validation and in the quality control of the new dyes employed for the in vitro study of molecular processes.

Chapter 5

Interaction between plasma membrane and amyloid protein

5.1 - Plasma membrane and membrane model

The membrane of cells is the interface through which all interactions of the cell with its direct outer world take place (*Figure 5.1*). It is a complex structure involved in important biological processes, including bidirectional transport of molecules and cell-cell communication. The two principal components of biological membranes are lipids and proteins, perfectly organized at the molecular level in a cell-dependent ratio[234]. Different kind of lipids composes the membrane structure: glycerophospholipids, sphingolipids, and sterols[235]. However, lipids are not uniformly distributed between the two membrane leaflets[236–238]: phosphatidylcholine, which accounts for more than half of phospholipids in most of the eukaryotic membranes, is mainly located in the outer leaflet, as well as sphingolipids, while phosphatidylserine, phosphatidylethanolamine and phosphatidylinositol are predominantly found in the inner leaflet. Cholesterol resides for more than 70% in the cytofacial leaflet. Nevertheless, its presence and distribution in the exofacial leaflet are fundamental in determining lateral lipid organization.

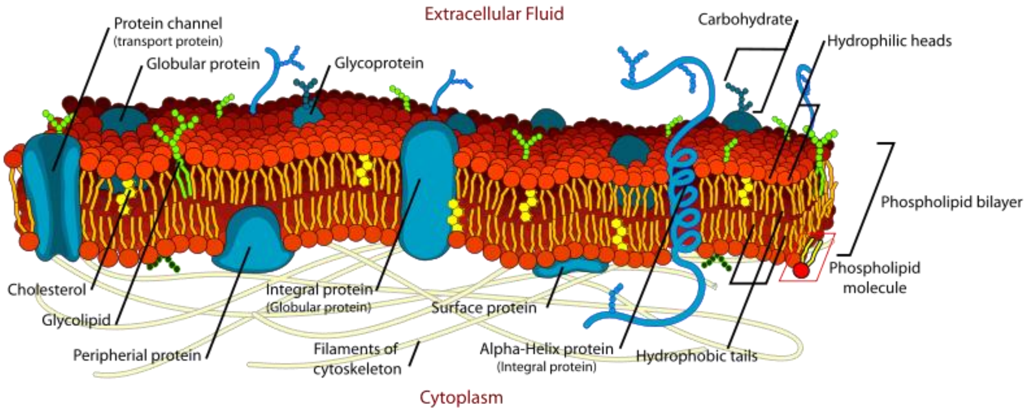
Protein channel
(transport protein)
Globular protein
Extracellular Fluid
Glycoprotein
Carbohydrate
Hydrophilic heads
Phospholipid bilayer
Phospholipid
molecule
Cholesterol
Glycolipid
Peripherial protein
Integral protein
(Globular protein)
Surface protein
Filaments of
cytoskeleton
Alpha-Helix protein
(Integral protein)
Hydrophobic tails
Cytoplasm

Figure 5.1 | Schematic representation of plasma membrane.

The membrane basic structure consists of a double layer of amphiphilic lipid molecules, with the polar parts pointing toward the aqueous medium and the hydrophobic moieties facing each other. Plasma membrane, ranging from only a few nanometers in thickness, is selectively permeable, generally less permeable to large, polar solutes and therefore drugs and biomolecules interacting with the cell must first permeate the membrane.

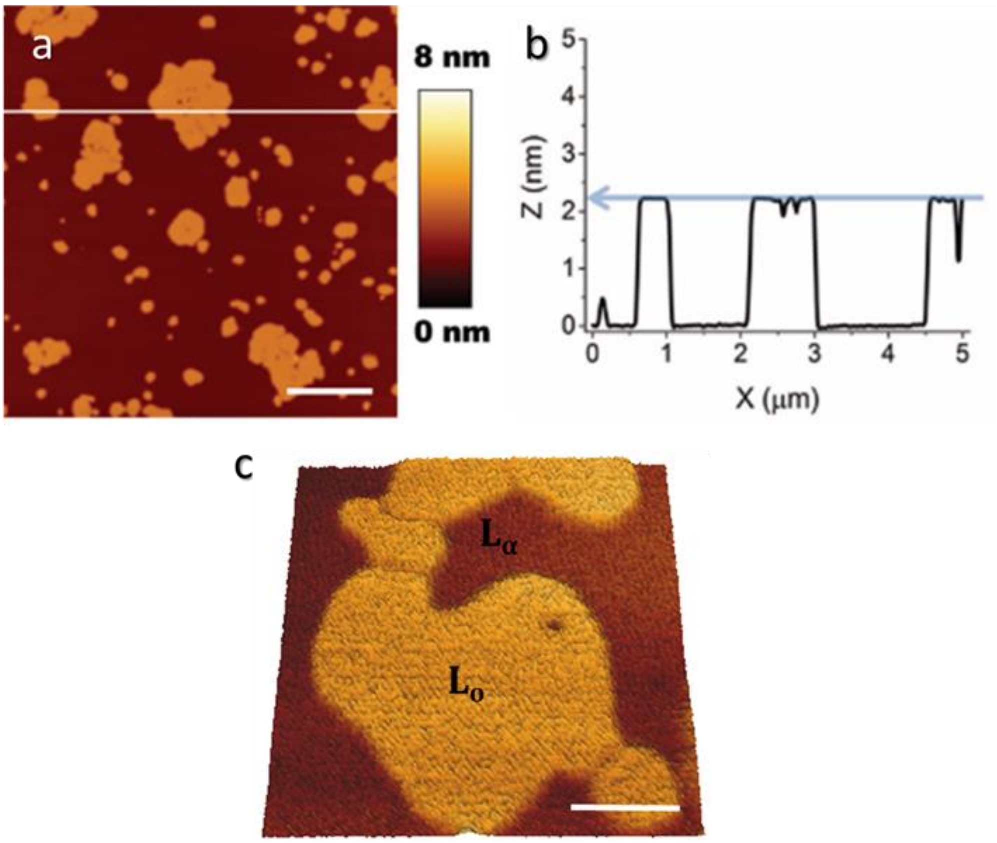

Figure 5.2 | Phase separation in a supported lipid bilayer containing DOPC, Sphingomyelin (SM), Cholesterol and GM1 imaged using AFM. (a) Typical morphology. Scale bar: 1.0 μm. (b) Cross section was taken along the white line in a (X axis). The difference in height between the two phases is ~ 2.2 nm. Images and plot profile from *Oropesa et al.*[78] . (c) Particular view of lipid l_α and l_o domains. Scale bar: 200 nm.

The first modern model was proposed by S.J. Singer and Garth L. Nicolson in 1972, called the fluid mosaic model[239]. The model has evolved somewhat over time, but it still best accounts for the structure and functions of the plasma membrane as we now understand them. However, this model did not take into account a central aspect of the lipid bilayer structure, the lateral organization of the membrane that is involved in several functions such as signal transduction, protein and lipid sorting, and endocytosis. In 1997 it was introduced a new concept asserting the not uniformity in the lipid distribution in cell membrane matrix[240]. It is thought that different types of lipids actively phase-segregate, forming distinct compartments[241], different in composition and physical properties.

The differential solubility of the plasma membrane, treating the cells with a cold detergent, such as Triton-X, was demonstrated[242]. One of those fractions, defined as a detergent-resist membrane, or lipid raft, is enriched in cholesterol and sphingolipids[243]. Lipid rafts are small liquid-ordered (L_α) assemblies of sphingolipids, cholesterol and raft-associated membrane proteins that diffuse within the liquid disordered (L_o) lipid membrane. Raft and raft-associated membrane proteins have been recognized has the responsible of a growing number of physiological and pathological cellular processes and hence our interest in them[77,78,244]. Due to their small size (10-200 nm)[245] or to their possible transient nature[246], direct observation of these structures in the real cell membrane is still missing. To test this hypothesis but to avoid the inherent complexity and heterogeneity of the cell membrane, a simplified model capable of mimicking the behavior of the extracellular membrane have been used to investigate the segregation behavior of lipids and different proteins in predetermined lipid mixture. Work in this direction has been performed using atomic force microscopy[77,78,247] (*Figure 5.2*) and a combination of AFM and fluorescent correlation spectroscopy[248,249].

5.2 – Alpha-synuclein: structure, functions, and interactions

α-Synuclein is a physiological protein mainly observed in the presynaptic terminal of the neurons. Although the function of native α-syn is not well understood, studies suggest that it is associated with the synapse and involved in synaptic activity, synaptic plasticity, neurotransmitter release, dopamine metabolism, synaptic pool maintenance and vesicle trafficking[272,273]. Disorders characterized by α-syn accumulation, Lewy body formation and Parkinsonism (and in some cases dementia) are collectively known as Lewy body diseases (LBD). It is considered as a molecular biomarker for the detection of Parkinson disease (PD) in its earlier stages[274], also present in AD plaques as a non-Aβ component (NAC). The molecular mechanism(s) through which α-syn abnormally accumulates and contributes to neurodegeneration in these disorders remains unknown.

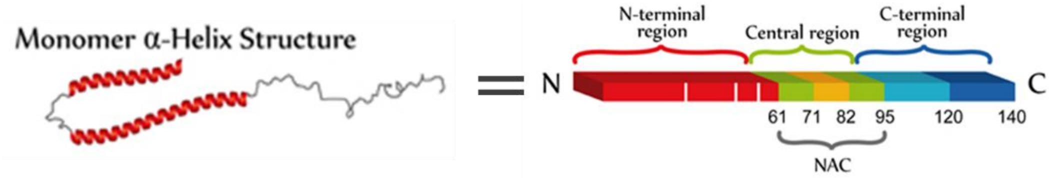

Figure 5.3 | Primary and secondary structure of α-syn. To right shows the three main domains of α-syn. The N-terminal is an amphipathic domain that contains the three point mutations (white bars) linked to the autosomal dominant form of PD. The central region is a highly hydrophobic domain that was originally identified in patients with AD or LBD, which is the precursor of the non-amyloidogenic component of the extracellular senile plaque (NAC), which promotes the protein aggregation. The C-terminal domain has an acidic character, which possesses anti-amyloidogenic properties.

The human α-syn protein is made of 140 amino acids with three domains: an N-terminal lipid-binding region, a hydrophobic central domain and a C-terminal acidic tail (*Figure 5.3*). α-Syn can be present as an α-helix structure in association with phospholipids (lipid-binding region) or an unfolded conformation in the cytosol, suggesting that it plays specific roles in different cellular locations based on its dynamic structure[275]. The N-terminal domain of α-syn is a positively charged region, containing sequences repeats that are also present in the α-helical domain of apolipoproteins (lipid-transport proteins). These repeats are responsible for the ability to form α-helical structures and therefore important in α-syn-lipid interactions. The core region of α-syn, known as NAC, is particularly rich in hydrophobic residues and makes up the core region of amyloid fibrils as it forms cross-β structure[276,277]. The C-terminal domain of α-syn is present in a random coil structure due to its low hydrophobicity and high net negative charge. In vitro studies have revealed that α-syn aggregation can be induced by lowering pH or by truncations of the C-terminal[278,279]. α-Syn can be found both as an intrinsically disordered peptide in the cytosol but also with an α-helical conformation when associated to lipid membranes. It is therefore suggested based on its dynamic structure, to play specific roles in different cellular locations.

Amyloid protein and lipid membranes interaction is of critical importance in biology, potentially associated with toxicity and propagation of Parkinson´s disease. Several techniques, such as spectroscopy, AFM, and protein chemistry have been used to address and investigate the influence of lipid bilayer model, that mimic the outer leaflet membrane, on the aggregation of α-syn[280]. On the other hands, a well-characterized lipid composition and its relative SLB, for AFM-α-syn interaction studies, that simulate the cytoplasmic leaflet of the membranes is not still available.

Understanding the nature of the α-syn-membrane interaction, how it is involved in the toxicity may inform future studies aiming to develop therapeutic prevention and intervention.

5.3 - Materials and Methods

The experimental works described in this chapter are based on in situ AFM application, previous described in chapter 2. The main aim is related to the characterization of the affections induced by α-syn aggregates on Solid-supported Lipid Bilayers (SLBs). Here, it has been investigated on two different SLBs composition: a well-studied bilayer that mimic the outer (extracellular) leaflet (following the protocols previously defined in our lab[78]), and a new more complex bilayer model that simulate the inner leaflet (cytoplasmic) of the membranes. I will describe the procedures used in supported lipid bilayers preparation and the potentialities of AFM in the study of these model systems.

5.3.1 - SLB preparation

SLBs used in the experimental work were prepared employing vesicle fusion technique on mica substrate. Vesicle fusion consists in the deposition of a large unilamellar vesicles (LUVs) suspension onto a hydrophilic substrate: vesicle adsorption and spreading on the surface may lead, under specific conditions, to bilayer formation (*Figure 5.4*). LUVs solution has been made at 'Italian Institute of technology' in Genova by Barbara Salis, following a standard protocol[74].

For external leaflet, lipid vesicles are formed by unsaturated 1,2-dioleoyl-SN-glycero-3-phosphocholine (DOPC), sphingomyelin (SM) (brain, porcine) in a 2:1 molar ratio, cholesterol (Chol) 1% molar and 5% molar of ganglioside GM1 (brain, ovine). At room temperature, each LUVs suspension was diluted 10 times with ultrapure water. 40 µL of LUVs suspension 0.1 mg/mL were then administrated to freshly cleaved mica, attached to a coverslip slide. Right after, 10 µL of $CaCl_2$ 10 mM were added, in order to trigger vesicle fusion. After a variable resting time, preceding the beginning of bilayer formation (indicated by a variation of liquid spreading on the substrate), samples were stored at 60°C in a close chamber with 100% relative humidity (r.h) for 15 minutes. The samples were cooled at room temperature and, after 2.0 h, gently rinsed three times with ultrapure water to remove excess vesicles from the liquid phase before AFM measurements. The surface was kept hydrated during the rinse.

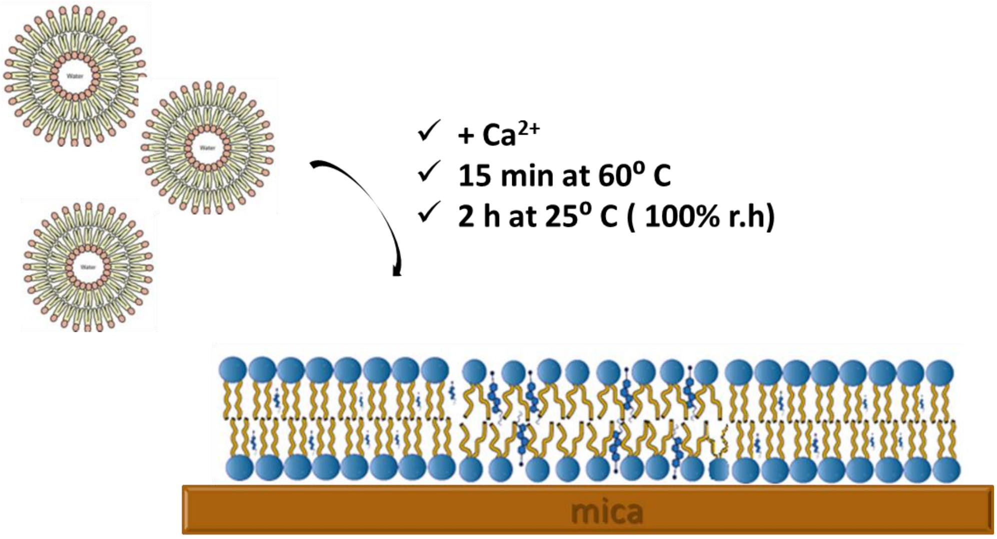

Figure 5.4 | Schematic representation of the vesicle fusion protocol employed in this work.

For the inner leaflet preparation was used the same vesicle fusion protocol described above. Different lipid compositions were tested to produce inner membrane models in order to fabricate a proper and stable SLB by vesicle fusion. In particular, the final LUVs composition, in molar ratios, employed for the experiments is: 45% DOPC, 20% 1,2-diolyeil-phosphatidylethanolamine (DOPE), 20% SM , 10% 1-palmitoyl-2-oleoyl-SN-glycero-3-phospho-L-serine (POPS) and 5% cholesterol. Using this lipid mixture, LUVs were fabricated in PBS 1X.

5.3.2 - Peptide preparation

Lyophilized α-syn (Sigma-Aldrich, St Louis, MO, USA) was dissolved, at the final concentration of 1 mg/ml in ultrapure water. Aliquots of 200 µl were stored at -20°C. Oligomers were prepared, starting from frozen aliquots, sonicated for 5 min, diluted at the selected concentration in ultrapure water and used for SLB interaction studies. Regarding the external leaflet, a 1nM concentration of α-syn was used, while for the inner bilayer increased concentration ranging from 20nM to 200nM.

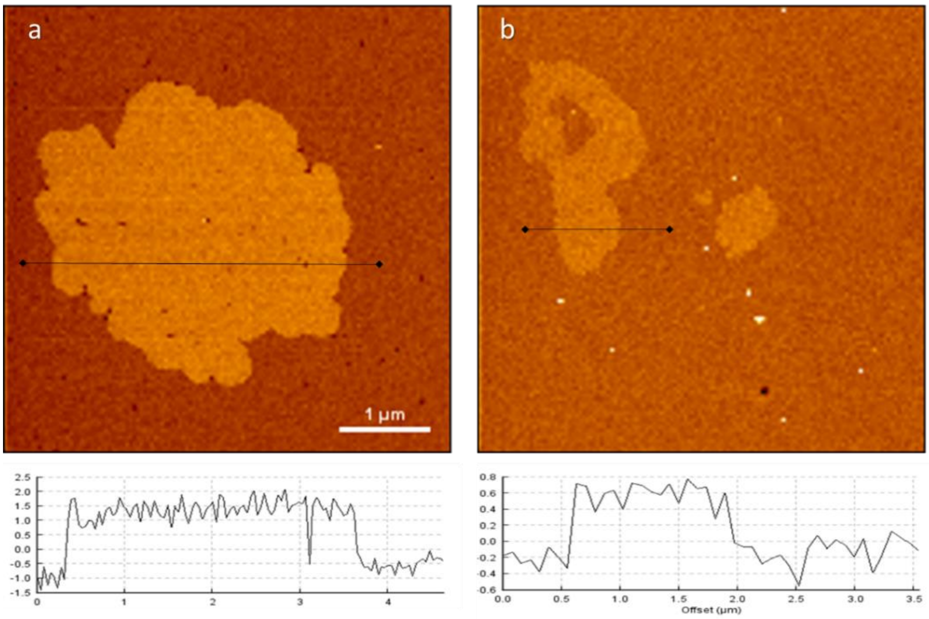

Figure 5.5 | Difference in thickness between outer (a) and inner (b) leaflet.

5.4.3 – AFM on Supported Lipid Bilayer

AFM measurements were performed by using the setup previously described in Chapter 3. V-shaped DNP silicon nitride cantilevers (Bruker, Massachusetts, US), with a nominal spring constant 0.24 N/m, a resonance frequency in air ranging from 40 to 75 kHz, and a tip with typical curvature radius

20-60 nm were used. Before α-syn administration, the morphological features of SLBs were evaluated through AFM imaging. The AFM tip was lifted up 100 µm from the sample, the oligomer was administered, to the bilayer, and let incubating for 10 minutes before further measurements. AFM imaging on SLBs is performed in a water environment to preserve the lamellar configuration of the bilayer. AFM images are acquired both in intermittent contact mode. In all the cases, the amplitude setpoint was kept above 70% of free oscillation amplitude to prevent possible damages to the sample. The determination of the difference in thickness between the ordered (L_β) and disordered (L_α) lipid phases (ΔZ) was determined by analyzing image height distributions with the help of the JPK Data Processing software (JPK Instruments, Germany). The actual spring constant of each cantilever was ascertained in situ, using the thermal noise method.

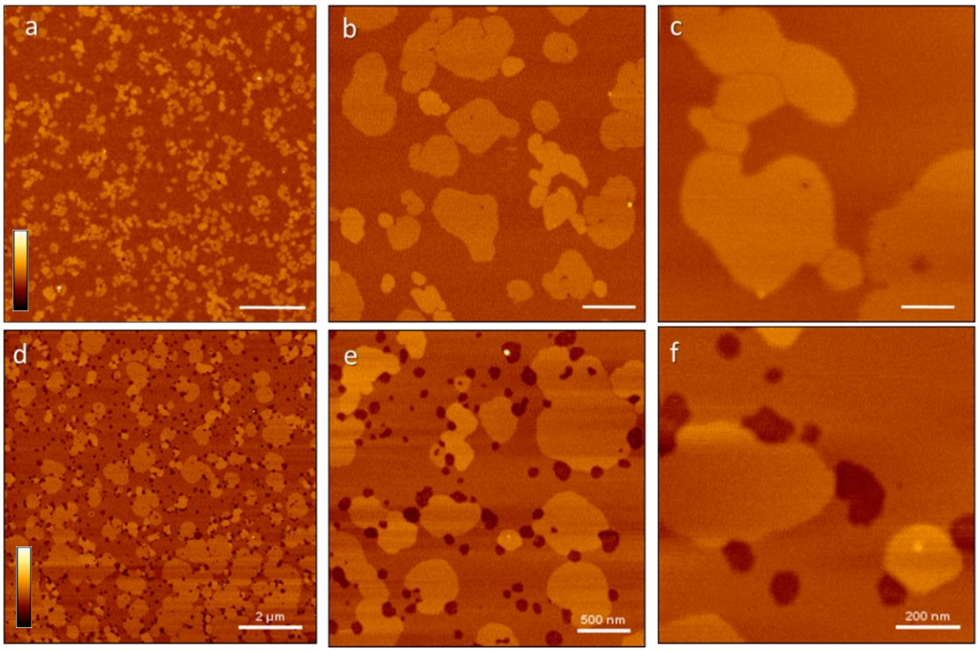

Figure 5.6 | AFM images of SLBs sampled before (a-c) and after administration of α-syn aggregates solutions (d-f). After 10 min incubation, α-syn induce destabilization on the defected-free bilayer. Scale bar 2 µm (a, d), 500 nm (b, e) and 200 nm (c, f). Z-range 10nm.

5.4 - Results

Cell membranes have complex lipid compositions, including an asymmetric distribution of phospholipids between the opposing leaflets of the bilayer.

Although it has been well observed the lipid composition of the outer leaflet of the plasma membrane and the formation of L_β domains, the lipids of the inner leaflet remains unknown[281].

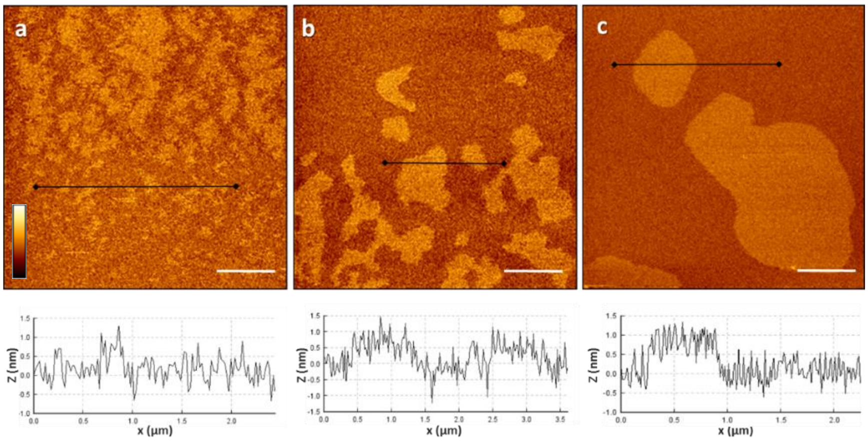

Figure 5.7 | The neural inner plasmatic model membrane (DOPC/DOPE/SM/POPS/ch) by AFM. The profile section (with the dark line) below the image shows the roughness in the initial stage of the scan session. Scale bar 1 µm (a, b), 500 nm (c). Z-range 6 nm (a, b), 10 nm (c).

It is well known that the lipid composition of outer and inner leaflets of the plasmatic neuronal membrane is different[282]. Both leaflets include phosphatidylcholine (PC), sphingomyelin (SM) and cholesterol (ch). In particular, the inner leaflet of the cellular membrane is more negatively charged than the outer leaflet and, in addition, it is characterized by the presence of phosphatidylethanolamine (PE). AFM result to be the most advantageous method for the study of the SLB model system, due to the high lateral and vertical resolutions. Indeed, it has been widely used to characterize supported model membranes[283,284], as well as to investigate their interaction with peptides at the nanoscale[285,286]. The unique features of AFM allow the study of the presence of different domains in the bilayer, including the difference in thickness between coexisting lipid phases. Here, I compared the morphology of the SLBs before and after the interaction with α-syn. In *Figure 5.5*, it is shown a typical bilayer morphology with characteristic raft domain for each lipid composition. The first morphology shown in *Figure 5.2c* is related to the microdomains thickness, which range from 1 nm to 1.5 nm in the DOPC/SM/ch/GM1 SLB, while for inner leaflet (DOPC/DOPE/SM/POPS/ch) less than 1 nm.

The experimental protocol employed in this study, regarding the peptide interaction, consisted in administering α-syn aggregates solution to defect-free bilayers, incubating for 10 min, rinsing, and checking with AFM to determine possible destabilizing effects. The integrity of DOPC/SM/ch/GM1 SLBs has been verified with AFM before peptide administration: intermittent contact imaging produced typical topography as expected for an intact SLB (*Figure 5.6 a-c*). In addition, the process of bilayer phases formation can be monitored through image acquisition at different time intervals after vesicles administration until it reaches the complete stabilisation. Images were acquired at 10x10 µm, 5x5 µm and 1x1 µm.

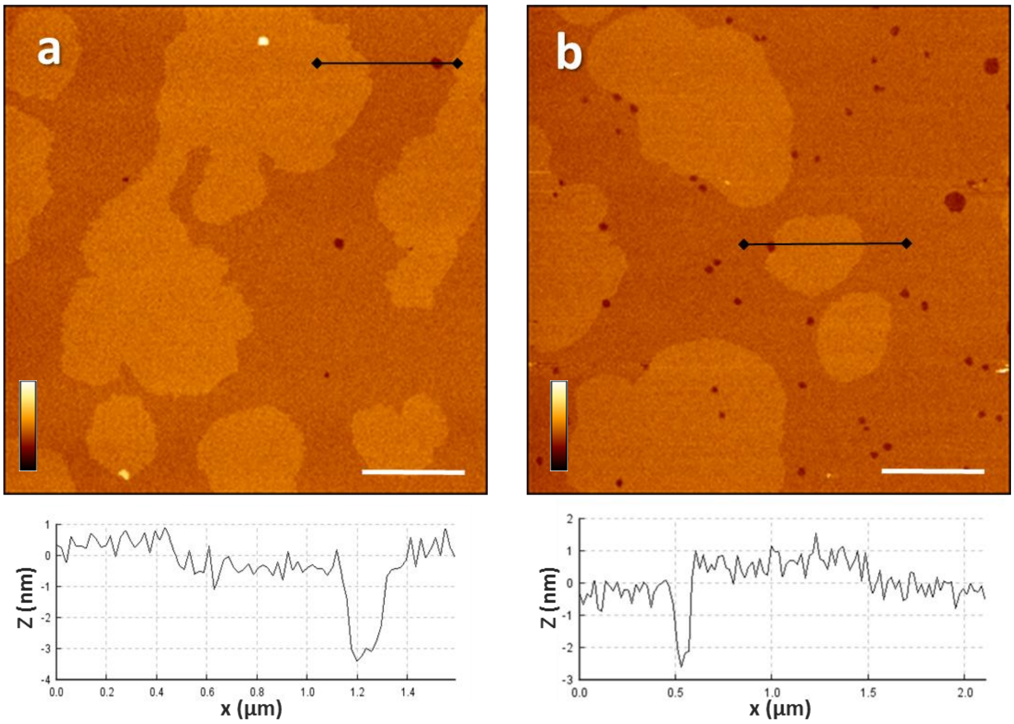

Figure 5.8 | AFM Images of α-syn interaction with DOPC/DOPE/SM/POPS/ch bilayer. After 10 min incubation time oligomers peptide induced removal of bilayer parts and consequent holes formation. (a) 20 nM and (b) 70 nM concentration of α-syn deposited. The black line indicates a profile section (showed below). Scale bar 1 µm. Z-range 10 nm.

Right after, SLB has been incubated with aggregates solutions at 1 nM concentration, following the procedure described above. In *Figure 5.6 d-f* it is shown the peptide effect obtained, after waiting 10 min, on the bilayer surface.

The results indicate an evident disruptive interaction between α-syn and DOPC/SM/ch/GM1 lipid membrane, indicated by the holes formation on the surface. This result is in agreement with a large number of literature data[51,76–78], which identify that low concentration of oligomers peptide induced removal of bilayer parts and consequent holes formation. In our experiments it is clear that the damage is higher in the fluid domain.

For the inner leaflet preparation was used the protocol described in Methods section. Firstly, it has been tested the stability and the presence of the phase on the bilayer. Initially, the lipid segregation within the bilayer appears not well define (as it is shown in *Figure 5.7 a*). After the complete formation and stabilization of the order phase domain (*Figure 5.7 c*), the protein solution has been added on the bilayer. I observed that, as expected, the interaction is concentration-dependent. The first visible effect on lipid bilayer was observed at 20 nM concentration of α-syn (*Figure 5.8 a*), at this concentration the formation of holes is evident. Besides, increasing the protein concentration at 70 nM further destabilization is obtained (*Figure 5.8 b*). In *Figure 5.8* are reported images of the same sample shown in *Figure 5.7*.

Also in this second case, the damage is prominently in the fluid phase domain, indicating that the mechanical properties of the lipid membrane have a central role in the definition of the mechanism of interaction between membrane and pathological peptides/peptide aggregates. Furthermore, these results indicates that a significant damage of the outer leaflet composition membrane is obtained at concentration at least 20 time lower with respect to the membranes that simulate the inner composition.

Studies performed by Barbara Salis in our lab by means of Quartz Crystal Microbalance (QCM) confirmed the inner bilayer-protein interaction data obtained in this study by AFM.

These results are preliminary, but in my thesis work, I set the condition for the formation of the bilayer that mimic the inner leaflet composition, a fundamental step to obtain further consistent and reproducible results. A further step in this research activity would be represented by the introduction of some fluorescent components and in a combined analysis by using the integrated AFM/STED setup described above.

Chapter 6
General Conclusions

My work is focused on the application of advanced biophysical approaches to the study of molecular processes involved in protein conformational diseases that arise from uncorrected protein folding and subsequent aggregation.

My work can be divided into two phases. The main part is presented in Chapter 4, and regards the study of the anomalous effects induces by the presence of fluorescently labeled peptides on the fibrillation process of misfolded proteins. The second part, described in Chapter 5, introduces a study on the interaction of a particular amyloidogenic peptide, α-syn, and planar supported lipid membranes.

In particular, I show that the slowing of the kinetics of aggregation, detectable with several techniques such as ThT binding, AFM, reported in this study and others present in the literature (FTIR, time-lapse) is just an aspect of the influence of the labeled monomers on the intermolecular processes. The results obtained by applying for the first time correlative AFM-STED microscopy to this biological problem revealed the rising of unexpected mechanisms of aggregation. I clearly demonstrate that labeled peptides are following only selective aggregation pathways, as a result of this, only part the amyloid aggregates, generated by the aggregation of a mixture of labeled/unlabeled monomers, are fluorescent. This novel findings generate a warning: fluorescence techniques are not able to characterise all the products derived from the in vitro aggregation of misfolded proteins. This statement reveals the importance to correlate fluorescence data with other derived from label-free techniques. The loss of information that is not only affecting the imaging, but also the spectroscopic techniques based on the fluorescence of a dye molecule, is suggesting the primary role that can be played by label-free techniques.

We pointed out that the presence of these two species of aggregates can be evinced only by applying a coupled AFM-fluorescence microscopy correlative technique.

These findings, defining a new and not expected scenario, suggested the need of new investigations aimed to characterize the physico-chemical properties of the two species of aggregates, i.e., fluorescent and non-fluorescent aggregates. Furthermore, the analysis should be extended to the bio-activity of the same species with a particular focus on their toxicity.

In Chapter 5, I present a study on the interaction mechanisms of α-syn, a peptide related to Parkinson's disease, and lipid membranes. In particular, the role of membrane composition is investigated. I focused my attention on two different compositions of lipids, one that mimic the external part of the neuronal cell membrane, and a second that resembles that internal leaflet of the membrane. I observed that α-syn is able to damage both the model membranes, but concentrating its destabilization on the fluid part of the membrane. Furthermore, I found that the membranes derived from the external leaflet composition are destabilized at a lower peptides concentration. The formation of pore-like structure was not detected in my investigation, supporting the idea of a cytotoxic mechanism related to membrane disruption. This result suggests a new aspect to be considered in the definition of the mechanism of neurodegeneration in Parkinson's disease. The work on the bilayer that mimic the inner leaflet composition has to be consider as a preliminary step toward the accomplishment of a systematic investigation. However, in my PhD work I set the experimental conditions that will allow the preparation of reproducible samples and a well-defined method.

References

1. Sipe, J. D. *et al.* Nomenclature 2014: Amyloid fibril proteins and clinical classification of the amyloidosis. *Amyloid* **21,** 221–224 (2014).
2. Dobson, C. M. Protein folding and misfolding. **426,** (2003).
3. Fink, A. L. Protein aggregation: Folding aggregates, inclusion bodies and amyloid. *Fold. Des.* **3,** 9–23 (1998).
4. Bucciantini, M., Rigacci, S. & Stefani, M. Amyloid aggregation: Role of biological membranes and the aggregate-membrane system. *J. Phys. Chem. Lett.* **5,** 517–527 (2014).
5. Virchow, R. Ueber eine im Gehirn und Rückenmark des Menschen aufgefundene Substanz mit der chemischen Reaction der Cellulose. *Arch. für Pathol. Anat. und Physiol. und für Klin. Med.* **6,** 135–138 (1854).
6. Friedreich, N.; Kekule, A. Zur Amyloidfrange. Virchows Arch Pathol Anat 1859, 16, 50–65.
7. Divry, P., and Florkin, M. (1927) Sur les proprietes optiques de l'amyloide, C. R. Soc. Biol. 97, 1808–1810.
8. Cohen, A. S. & Calkins, E. Electron Microscopic Observations on a Fibrous Component in Amyloid of Diverse Origins. *Nature* **183,** 1202 (1959).
9. Stefani, M. & Dobson, C. M. Protein aggregation and aggregate toxicity: New insights into protein folding, misfolding diseases and biological evolution. *J. Mol. Med.* **81,** 678–699 (2003).
10. Chiti, F. & Dobson, C. M. Protein Misfolding, Functional Amyloid, and Human Disease. *Annu. Rev. Biochem.* **75,** 333–366 (2006).
11. Sambrook, J. & Gething, M. J. Protein folding in the cell. *Nature* **355,** 33–45 (1992).
12. Brodsky, J. L. & McCracken, A. A. ER protein quality control and proteasome-mediated protein degradation. *Semin. Cell Dev. Biol.* **10,** 507–513 (1999).
13. Vendruscolo, M., Zurdo, J., Macphee, C. E. & Dobson, C. M. Protein folding and misfolding: A paradigm of self-assembly and regulation in complex biological systems. *Philos. Trans. R. Soc. A Math. Phys. Eng. Sci.* **361,** 1205–1222 (2003).
14. Levinthal, C. Are there pathways for protein folding? *J. Chim. Phys.* **65,** 44–45 (1968).
15. Dill, K. A. & Chan, H. S. From levinthal to pathways to funnels. *Nature Structural Biology* **4,** 10–19 (1997).
16. Dinner, A. R., Šalib, A., Smitha, L. J., Dobsona, C. M. & Karplus, M. Understanding protein folding via free-energy surfaces from theory and experiment. *Trends Biochem. Sci.* **25,** 331–339 (2000).
17. Chan, H. S. & Dill, K. A. Protein folding in the landscape perspective: Chevron plots and non-arrhenius kinetics. *Proteins Struct. Funct. Genet.* **30,** 2–33 (1998).
18. Anfinsen, C. B. Principles that Govern the Folding of Protein Chains. *Science (80-.).* **181,** 223–230 (1973).
19. Fersht, A. R. & Daggett, V. Protein folding and unfolding at atomic resolution. *Cell* **108,** 573–582 (2002).
20. Kaufman, R. J. *et al.* The unfolded protein response in nutrient sensing and differentiation. *Nat. Rev. Mol. Cell Biol.* **3,** 411–421 (2002).
21. Stefani, M. Protein misfolding and aggregation: New examples in medicine and biology of the dark side of the protein world. *Biochim. Biophys. Acta - Mol. Basis Dis.*

1739, 5–25 (2004).
22. Luheshi, L. M. & Dobson, C. M. Bridging the gap: From protein misfolding to protein misfolding diseases. *FEBS Lett.* **583,** 2581–2586 (2009).
23. Thomas, P. J., Qu, B. H. & Pedersen, P. L. Defective protein folding as a basis of human disease. *Trends Biochem. Sci.* **20,** 456–459 (1995).
24. Ellis, R. J. Macromolecular crowding: an important but neglected aspect of the intracellular environment. *Curr. Opin. Struct. Biol.* **11,** 114–119 (2001).
25. Priya, S., Sharma, S. K. & Goloubinoff, P. Molecular chaperones as enzymes that catalytically unfold misfolded polypeptides. *FEBS Lett.* **587,** 1981–1987 (2013).
26. Uversky, V. N. Mysterious oligomerization of the amyloidogenic proteins. *FEBS J.* **277,** 2940–2953 (2010).
27. Makin, O. S. & Serpell, L. C. Structures for amyloid fibrils. *FEBS J.* **272,** 5950–5961 (2005).
28. Baldwin, A. J. *et al.* Metastability of Native Proteins and the Phenomenon of Amyloid Formation. *J. Am. Chem. Soc.* **133,** 14160–14163 (2011).
29. Eanes, E. D. & Glenner, G. G. X-ray Diffraction Studies on Amyloid Filaments. *J. Histochem. Cytochem.* **16,** 673–677 (1968).
30. Marshall, K. E. & Serpell, L. C. Insights into the structure of amyloid fibrils. *Open Biol. J.* **2,** 185–192 (2009).
31. Ladiwala, A. R. A. *et al.* Conformational Differences between Two Amyloid β Oligomers of Similar Size and Dissimilar Toxicity. (2012).
32. Bouchard, M., Zurdo, J., Nettleton, E. J., Dobson, C. M. & Robinson, C. V. Formation of insulin amyloid fibrils followed by FTIR simultaneously with CD and electron microscopy. *Protein Sci.* **9,** 1960–1967 (2000).
33. Groenning, M. *et al.* Binding mode of Thioflavin T in insulin amyloid fibrils. *J. Struct. Biol.* **159,** 483–497 (2007).
34. Lührs, T. *et al.* 3D structure of Alzheimer's amyloid-β(1–42) fibrils. *Proc. Natl. Acad. Sci.* **102,** 17342–17347 (2005).
35. Serpell, L. C. *et al.* The Protofilament Substructure of Amyloid Fibrils. 1033–1039 (2000). doi:10.1006/jmbi.2000.3908
36. Jiménez, J. L. *et al.* The protofilament structure of insulin amyloid fibrils. *Proc. Natl. Acad. Sci. U. S. A.* **99,** 9196–201 (2002).
37. Petkova, A. T. *et al.* A structural model for Alzheimer's beta -amyloid fibrils based on experimental constraints from solid state NMR. *Proc. Natl. Acad. Sci. U. S. A.* **99,** 16742–7 (2002).
38. Ma, B. & Nussinov, R. Stabilities and conformations of Alzheimer's beta -amyloid peptide oligomers (Abeta 16-22, Abeta 16-35, and Abeta 10-35): Sequence effects. *Proc. Natl. Acad. Sci. U. S. A.* **99,** 14126–31 (2002).
39. Sawaya, M. R. *et al.* Atomic structures of amyloid cross-β spines reveal varied steric zippers. *Nature* **447,** 453 (2007).
40. Soriaga, A. B., Sangwan, S., MacDonald, R., Sawaya, M. R. & Eisenberg, D. Crystal structures of IAPP amyloidogenic segments reveal a novel packing motif of out-of-register beta sheets. *J. Phys. Chem. B* **120,** 5810–5816 (2016).
41. Rochet, J. C. & Lansbury, P. T. Amyloid fibrillogenesis: themes and variations. *Curr. Opin. Struct. Biol.* **10,** 60–8 (2000).
42. Khurana, R. *et al.* Mechanism of thioflavin T binding to amyloid fibrils. **151,** 229–238 (2005).
43. Di Carlo, M. G. *et al.* Thioflavin T templates amyloid β(1-40) conformation and

aggregation pathway. *Biophys. Chem.* **206,** 1–11 (2015).
44. Xue, C., Lin, T. Y., Chang, D. & Guo, Z. Thioflavin T as an amyloid dye: Fibril quantification, optimal concentration and effect on aggregation. *R. Soc. Open Sci.* **4,** (2017).
45. Stsiapura, V. I., Maskevich, A. A., Kuzmitsky, V. A., Turoverov, K. K. & Kuznetsova, I. M. Computational Study of Thioflavin T Torsional Relaxation in the Excited State. *J. Phys. Chem. A* **111,** 4829–4835 (2007).
46. Voropai, E. S. *et al.* Spectral properties of thioflavin T and its complexes with amyloid fibrils. *J. Appl. Spectrosc.* **70,** 868–874 (2003).
47. Srivastava, A. *et al.* Identifying the Bond Responsible for the Fluorescence Modulation in an Amyloid Fibril Sensor. *Chem. - A Eur. J.* **16,** 9257–9263 (2010).
48. Ban, T., Hamada, D., Hasegawall, K., Naiki, H. & Goto, Y. Direct observation of amyloid fibril growth monitored by thioflavin T fluorescence. *J. Biol. Chem.* **278,** 16462–16465 (2003).
49. Naiki, H., Higuchi, K., Hosokawa, M. & Takeda, T. Fluorometric determination of amyloid fibrils in vitro using the fluorescent dye, thioflavine T. *Anal. Biochem.* **177,** 244–249 (1989).
50. Cohen, S. I. A. A. *et al.* Nucleated polymerization with secondary pathways. I. Time evolution of the principal moments. *J. Chem. Phys.* **135,** 065105 (2011).
51. Butterfield, S. M. & Lashuel, H. A. Amyloidogenic Protein–Membrane Interactions: Mechanistic Insight from Model Systems. *Angew. Chemie Int. Ed.* **49,** 5628–5654
52. Jahn, T. R. & Radford, S. E. The Yin and Yang of protein folding. *FEBS J.* **272,** 5962–5970 (2005).
53. Dumoulin, M., Kumita, J. R. & Dobson, C. M. Normal and aberrant biological self-assembly: Insights from studies of human lysozyme and its amyloidogenic variants. *Acc. Chem. Res.* **39,** 603–610 (2006).
54. Debelouchina, G. T., Platt, G. W., Bayro, M. J., Radford, S. E. & Griffin, R. G. Magic angle spinning NMR analysis of β 2-microglobulin amyloid fibrils in two distinct morphologies. *J. Am. Chem. Soc.* **132,** 10414–10423 (2010).
55. Uversky, V. N., Li, J. & Fink, A. L. Evidence for a Partially Folded Intermediate in ??-Synuclein Fibril Formation. *J. Biol. Chem.* **276,** 10737–10744 (2001).
56. Calamai, M., Chiti, F. & Dobson, C. M. Amyloid fibril formation can proceed from different conformations of a partially unfolded protein. *Biophys. J.* **89,** 4201–4210 (2005).
57. Bader, R., Bamford, R., Zurdo, J., Luisi, B. F. & Dobson, C. M. Probing the Mechanism of Amyloidogenesis through a Tandem Repeat of the PI3-SH3 Domain Suggests a Generic Model for Protein Aggregation and Fibril Formation. *J. Mol. Biol.* **356,** 189–208 (2006).
58. Relini, A. *et al.* Monitoring the Process of HypF Fibrillization and Liposome Permeabilization by Protofibrils. *J. Mol. Biol.* **338,** 943–957 (2004).
59. Wilson, M. R., Yerbury, J. J. & Poon, S. Potential roles of abundant extracellular chaperones in the control of amyloid formation and toxicity. *Mol. Biosyst.* **4,** 42–52 (2007).
60. Jansen, R., Dzwolak, W. & Winter, R. Amyloidogenic self-assembly of insulin aggregates probed by high resolution atomic force microscopy. *Biophys. J.* **88,** 1344–1353 (2005).
61. Mielke, M. M., Vemuri, P. & Rocca, W. A. Clinical epidemiology of Alzheimer's disease: Assessing sex and gender differences. *Clin. Epidemiol.* **6,** 37–48 (2014).

62. Du, X., Wang, X. & Geng, M. Alzheimer's disease hypothesis and related therapies. *Transl. Neurodegener.* **7,** 1–7 (2018).
63. Harris, J. R. *Protein Aggregation and Fibrillogenesis in Cerebral and Systemic Amyloid Disease*. (Springer Netherlands, 2012). at <https://books.google.it/books?id=R9upBYWAumgC>
64. Hardy, J. & Selkoe, D. J. The Amyloid Hypothesis of Alzheimer ' s Disease : Progress and Problems on the Road to Therapeutics.
65. Karran, E., Mercken, M. & Strooper, B. De. The amyloid cascade hypothesis for Alzheimer's disease: An appraisal for the development of therapeutics. *Nat. Rev. Drug Discov.* **10,** 698–712 (2011).
66. Dong, S., Duan, Y., Hu, Y. & Zhao, Z. Advances in the pathogenesis of Alzheimer's disease: a re-evaluation of amyloid cascade hypothesis. *Transl. Neurodegener.* **1,** 18 (2012).
67. Gong, Y. *et al.* Alzheimer's disease-affected brain: Presence of oligomeric A ligands (ADDLs) suggests a molecular basis for reversible memory loss. *Proc. Natl. Acad. Sci.* **100,** 10417–10422 (2003).
68. Chafekar, S. M., Hoozemans, J. J. M., Zwart, R., Baas, F. & Scheper, W. A *β* $_{1-42}$ Induces Mild Endoplasmic Reticulum Stress in an Aggregation State–Dependent Manner. *Antioxid. Redox Signal.* **9,** 2245–2254 (2007).
69. Journals, H. & Article, R. Alzheimer ' s Disease : A Review. (2017).
70. Eikelenboom, P. *et al.* Neuroinflammation in Alzheimer's disease and prion disease. *Glia* **40,** 232–239 (2002).
71. Tan, S. Y. & Pepys, M. B. Amyloidosis. *Histopathology* **25,** 403–14 (1994).
72. Bucciantini, M., Giannoni, E., Chiti, F., Baroni, F. & Formigli, L. Inherent toxicity of aggregates implies a common mechanism for protein misfolding diseases. 507–511 (2002).
73. Winner, B. *et al.* In vivo demonstration that α-synuclein oligomers are toxic. *Proc. Natl. Acad. Sci.* **108,** 4194–4199 (2011).
74. Canale, C. *et al.* Different effects of Alzheimer's peptide Aβ(1-40) oligomers and fibrils on supported lipid membranes. *Biophys. Chem.* **182,** 23–29 (2013).
75. Williams, T. L. & Serpell, L. C. Membrane and surface interactions of Alzheimer's A?? peptide - Insights into the mechanism of cytotoxicity. *FEBS J.* **278,** 3905–3917 (2011).
76. Davis, C. H. & Berkowitz, M. L. Interaction between amyloid-β (1-42) peptide and phospholipid bilayers: A molecular dynamics study. *Biophys. J.* **96,** 785–797 (2009).
77. Seghezza, S., Diaspro, A., Canale, C. & Dante, S. Cholesterol drives Aβ(1-42) interaction with lipid rafts in model membranes. *Langmuir* **30,** 13934–13941 (2014).
78. Oropesa-Nuñez, R. *et al.* Interaction of toxic and non-toxic HypF-N oligomers with lipid bilayers investigated at high resolution with atomic force microscopy. *Oncotarget* **7,** 44991–45004 (2016).
79. Dante, S., Hauß, T. & Dencher, N. A. Cholesterol inhibits the insertion of the Alzheimer's peptide Aβ(25-35) in lipid bilayers. *Eur. Biophys. J.* **35,** 523–531 (2006).
80. Williams, T. L. *et al.* Aβ42 oligomers, but not fibrils, simultaneously bind to and cause damage to ganglioside-containing lipid membranes. *Biochem. J.* **439,** 67–77 (2011).
81. Lambert, M. P. *et al.* Diffusible, nonfibrillar ligands derived from Aβ1-42 are potent central nervous system neurotoxins. *Proc. Natl. Acad. Sci.* **95,** 6448–6453 (1998).
82. Picone, P. *et al.* Biological and biophysics aspects of metformin-induced effects: Cortex mitochondrial dysfunction and promotion of toxic amyloid pre-fibrillar aggregates. *Aging (Albany. NY).* **8,** 1718–1734 (2016).

83. Conway, K. A. *et al.* Acceleration of oligomerization, not fibrillization, is a shared property of both alpha -synuclein mutations linked to early-onset Parkinson's disease: Implications for pathogenesis and therapy. *Proc. Natl. Acad. Sci.* **97,** 571–576 (2000).
84. Cajavec, B. & Bernard, S. Aggregation in Huntington's Disease. *Genome Informatics* **16,** 262–271 (2005).
85. Hicks, D. A., Nalivaeva, N. N. & Turner, A. J. Lipid rafts and Alzheimer's disease: Protein-lipid interactions and perturbation of signaling. *Front. Physiol.* **3 JUN,** (2012).
86. Wolozin, B. A fluid connection: cholesterol and Abeta. *Proc. Natl. Acad. Sci. U. S. A.* **98,** 5371–3 (2001).
87. Esch, F. S. *et al.* Cleavage of amyloid β peptide during constitutive processing of its precursor. *Science (80-.).* **248,** 1122–1124 (1990).
88. Seubert, P. *et al.* Secretion of β-amyloid precursor protein cleaved at the amino terminus of the β-amyloid peptide. *Nature* **361,** 260 (1993).
89. Galván, Y., Mori, H., Takio, K., Ogawara, M. & Selkoe, D. J. Mass spectrometry of purified amyloid beta protein in Alzheimer's disease. *J. Biol. Chem.* **267,** 17082–17086 (1992).
90. Naslund, J. *et al.* Relative abundance of Alzheimer A beta amyloid peptide variants in Alzheimer disease and normal aging. *Proc. Natl. Acad. Sci.* **91,** 8378–8382 (1994).
91. Meisl, G. *et al.* Differences in nucleation behavior underlie the contrasting aggregation kinetics of the Aβ40 and Aβ42 peptides. *Proc. Natl. Acad. Sci.* **111,** 9384–9389 (2014).
92. Kodali, R. & Wetzel, R. Polymorphism in the intermediates and products of amyloid assembly. *Curr. Opin. Struct. Biol.* **17,** 48–57 (2007).
93. Schmidt, M. *et al.* Comparison of Alzheimer Aβ(1–40) and Aβ(1–42) amyloid fibrils reveals similar protofilament structures. *Proc. Natl. Acad. Sci.* **106,** 19813 LP-19818 (2009).
94. Esbjörner, E. K. *et al.* Direct observations of amyloid β Self-assembly in live cells provide insights into differences in the kinetics of Aβ(1-40) and Aβ(1-42) aggregation. *Chem. Biol.* **21,** 732–742 (2014).
95. Cohen, S. I. A. *et al.* Proliferation of amyloid-β42 aggregates occurs through a secondary nucleation mechanism. *Proc. Natl. Acad. Sci. U. S. A.* **110,** 9758–63 (2013).
96. Sunde, M. *et al.* Common Core Structure of Amyloid Fibrils by Synchrotron X-ray Diffraction. (1997).
97. Dobson, C. M. The structural basis of protein folding and its links with human disease. *Philos. Trans. R. Soc. London. Ser. B Biol. Sci.* **356,** 133 LP-145 (2001).
98. Chiti, F. *et al.* Designing conditions for in vitro formation of amyloid protofilaments and fibrils. *Proc. Natl. Acad. Sci.* **96,** 3590–3594 (1999).
99. Navarra, G. *et al.* Heat- and pH-induced BSA conformational changes, hydrogel formation and application as 3D cell scaffold. *Arch. Biochem. Biophys.* **606,** 134–142 (2016).
100. Guijarro, J. I., Sunde, M., Jones, J. A., Campbell, I. D. & Dobson, C. M. Amyloid fibril formation by an SH3 domain. *Proc. Natl. Acad. Sci.* **95,** 4224–4228 (1998).
101. Litvinovich, S. V *et al.* Formation of amyloid-like fibrils by self-association of a partially unfolded fibronectin type III module11Edited by R. Huber. *J. Mol. Biol.* **280,** 245–258 (1998).
102. Giovanna, M. *et al.* Trifluoroethanol modulates α-synuclein amyloid-like aggregate formation, stability and dissolution. *Biophys. Chem.* **216,** 23–30 (2016).

103. Santangelo, M. G., Militello, V., Foderà, V. & Vetri, V. Back to the oligomeric state: pH-induced dissolution of concanavalin A amyloid-like fibrils into non-native oligomers. *Rsc Adv.* **6,** 75082–75091 (2016).
104. SUNDE, M. & BLAKE, C. in *Advances in Protein Chemistry Volume 50* **50,** 123–159 (Elsevier, 1997).
105. Dobson, C. M. Protein misfolding, evolution and disease. *Trends Biochem. Sci.* **24,** 329–332 (1999).
106. Zewail, A. H. *Physical biology: from atoms to medicine*. (Imperial college press, 2008).
107. Paz, D. *et al.* De novo designed peptide-based amyloid fibrils. (2002).
108. Broome, B. M. & Hecht, M. H. Nature Disfavors Sequences of Alternating Polar and Non-polar Amino Acids : Implications for Amyloidogenesis. 961–968 (2000). doi:10.1006/jmbi.2000.3514
109. Brange, J. & Langkjœr, L. in *Stability and Characterization of Protein and Peptide Drugs* 315–350 (Springer, 1993).
110. Brange, J., Andersen, L., Laursen, E. D., Meyn, G. & Rasmussen, E. Toward Understanding Insulin Fibrillation. *J. Pharm. Sci.* **86,** 517–525 (1997).
111. F. Sanger. F. Sanger, Biochem. J., 39 (1945) 507. **39,** (1944).
112. Ryle, A. P., Sanger, F., Smith, L. F. & Kitai, R. The disulphide bonds of insulin. *Biochem. J.* **60,** 541–556 (1955).
113. Tah, B. *et al.* Quantum-mechanical DFT calculation supported Raman spectroscopic study of some amino acids in bovine insulin. *Spectrochim. Acta - Part A Mol. Biomol. Spectrosc.* **129,** 345–351 (2014).
114. Brogden, R. N. & Heel, R. C. Human insulin. *Drugs* **34,** 350–371 (1987).
115. Heinemann, L., Heise, T., Jorgensen, L. N. & Starke, A. A. R. Action Profile of the Rapid Acting Insulin Analogue: Human Insulin B28Asp. *Diabet. Med.* **10,** 535–539
116. Chien, Y. W. Human Insulin: Basic Sciences to Therapeutic Uses. *Drug Dev. Ind. Pharm.* **22,** 753–789 (1996).
117. Dische, F. E. *et al.* Insulin as an amyloid-fibril protein at sites of repeated insulin injections in a diabetic patient. *Diabetologia* **31,** 158–161 (1988).
118. Brange, J. *Galenics of insulin: the physico-chemical and pharmaceutical aspects of insulin and insulin preparations*. (Springer Science & Business Media, 2012).
119. Chiti, F. *et al.* Designing conditions for in vitro formation of amyloid protofilaments and fibrils. *Proc. Natl. Acad. Sci.* **96,** 3590–3594 (1999).
120. Relini, A. *et al.* Monitoring the process of HypF fibrillization and liposome permeabilization by protofibrils. *J. Mol. Biol.* **338,** 943–957 (2004).
121. Vetri, V. *et al.* Amyloid fibrils formation and amorphous aggregation in concanavalin A. *Biophys. Chem.* **125,** 184–190 (2007).
122. Nielsen, L., Frokjaer, S., Brange, J., Uversky, V. N. & Fink, A. L. Probing the Mechanism of Insulin Fibril Formation with Insulin Mutants. *Biochemistry* **40,** 8397–8409 (2001).
123. Burke, M. J. & Rougvie, M. A. Cross-β protein structures. I. Insulin fibrils. *Biochemistry* **11,** 2435–2439 (1972).
124. Nielsen, L. *et al.* Effect of Environmental Factors on the Kinetics of Insulin Fibril Formation: Elucidation of the Molecular Mechanism. *Biochemistry* **40,** 6036–6046 (2001).
125. Klunk, W. E., Pettergrew, J. W. & Abraham, D. J. Quatitative Evaluation of Congo Red Binding with a Beta-pleated to. *J. Histochem. Cytochem.* **37,** 1273–1281 (1989).
126. Smith, M. I., Sharp, J. S. & Roberts, C. J. Nucleation and growth of insulin fibrils in bulk solution and at hydrophobic polystyrene surfaces. *Biophys. J.* **93,** 2143–2151

(2007).

127. Knowles, T. P. J. *et al.* Kinetics and thermodynamics of amyloid formation from direct measurements of fluctuations in fibril mass. *Proc. Natl. Acad. Sci.* **104,** 10016–10021 (2007).

128. Foderà, V., Librizzi, F., Groenning, M., Van De Weert, M. & Leone, M. Secondary nucleation and accessible surface in insulin amyloid fibril formation. *J. Phys. Chem. B* **112,** 3853–3858 (2008).

129. Librizzi, F., Foderà, V., Vetri, V., Lo Presti, C. & Leone, M. Effects of confinement on insulin amyloid fibrils formation. *Eur. Biophys. J.* **36,** 711–715 (2007).

130. Nayak, A., Sorci, M., Krueger, S. & Belfort, G. A universal pathway for amyloid nucleus and precursor formation for insulin. *Proteins Struct. Funct. Bioinforma.* **74,** 556–565 (2009).

131. Vestergaard, B. *et al.* A Helical Structural Nucleus Is the Primary Elongating Unit of Insulin Amyloid Fibrils. *PLoS Biol.* **5,** e134 (2007).

132. van Maarschalkerweerd, A., Vetri, V., Langkilde, A. E., Foderà, V. & Vestergaard, B. Protein/Lipid Coaggregates are Formed During α-Synuclein-Induced Disruption of Lipid Bilayers. *Biomacromolecules* **15,** 3643–3654 (2014).

133. Yang, X., Askarova, S. & Lee, J. C. M. Membrane biophysics and mechanics in Alzheimer's disease. *Mol. Neurobiol.* **41,** 138–148 (2010).

134. Lambert, M. P. *et al.* Diffusible, nonfibrillar ligands derived from Aβ1–42 are potent central nervous system neurotoxins. *Proc. Natl. Acad. Sci.* **95,** 6448–6453 (1998).

135. Conway, K. A. *et al.* Acceleration of oligomerization, not fibrillization, is a shared property of both α-synuclein mutations linked to early-onset Parkinson's disease: implications for pathogenesis and therapy. *Proc. Natl. Acad. Sci.* **97,** 571–576 (2000).

136. Nucifora, L. G. *et al.* Identification of novel potentially toxic oligomers formed in vitro from mammalian-derived expanded huntingtin exon-1 protein. *J. Biol. Chem.* **287,** 16017–16028 (2012).

137. Kim, H.-Y. *et al.* Structural properties of pore-forming oligomers of α-synuclein. *J. Am. Chem. Soc.* **131,** 17482–17489 (2009).

138. Azimov, R. & Kagan, B. L. in *Electrophysiology of Unconventional Channels and Pores* (ed. Delcour, A. H.) 343–360 (Springer International Publishing, 2015). doi:10.1007/978-3-319-20149-8_14

139. Lin, H. A. I., Bhatia, R. & Lal, R. Amyloid β protein forms ion channels: implications for Alzheimer's disease pathophysiology. *FASEB J.* **15,** 2433–2444 (2001).

140. Zhu, D. *et al.* Role of membrane biophysics in Alzheimer's-related cell pathways. *Front. Neurosci.* **9,** 186 (2015).

141. Domanov, Y. A. & Kinnunen, P. K. J. Islet amyloid polypeptide forms rigid lipid–protein amyloid fibrils on supported phospholipid bilayers. *J. Mol. Biol.* **376,** 42–54 (2008).

142. Kapitza, H. G. Microscopy from the very beginning. *Carl Zeiss Oberkochen* 1–48 (1997). doi:10.1111/j.1750-8606.2012.00246.x

143. Abbe, E. Beiträge zur Theorie des Mikroskops und der mikroskopischen Wahrnehmung. *Arch. für mikroskopische Anat.* **9,** 413–418 (1873).

144. Jablonski, A. Efficiency of anti-Stokes fluorescence in dyes. *Nature* **131,** 839 (1933).

145. Wilson, T., Shepparu, C. J. R. & Löschke, K. Theory and practice of scanning optical microscopy. Academic Press, London 1984, 213 Seiten, 138 Abbildungen, Preis $ 39.50 ISBN 0-12-757760-2. *Cryst. Res. Technol.* **20,** 1608–1608 (1985).

146. Hell, S. W. & Wichmann, J. Breaking the diffraction resolution limit by stimulated

emission: stimulated-emission-depletion fluorescence microscopy. *Opt. Lett.* **19,** 780 (1994).

147. Esplandiu, M. J. Scanning probe microscopies for analytical studies at the nanometer scale. **3,** 33–46 (2005).
148. Mellors, R. C. & Silver, R. A microfluorometric scanner for the differential detection of cells: Application to exfoliative cytology. *Science (80-.).* **114,** 356–360 (1951).
149. Minsky, M. Microscopy apparatus US patent 3013467. *USP Off. Ed. US* (1961).
150. Yeats, R. M., Yeats, M. F., Sheppard, C. J. R. & Wilson, T. The theory of the direct-view confocal microscope. *J. Microsc.* **124,** 107–117 (1981).
151. Földes-Papp, Z., Demel, U. & Tilz, G. P. Laser scanning confocal fluorescence microscopy: An overview. *Int. Immunopharmacol.* **3,** 1715–1729 (2003).
152. Benda, A., Aitken, H., Davies, D. S., Whan, R. & Goldsbury, C. STED imaging of tau filaments in Alzheimer's disease cortical grey matter. *J. Struct. Biol.* **195,** 345–352 (2016).
153. Huang, B., Babcock, H. & Zhuang, X. Breaking the diffraction barrier: Super-resolution imaging of cells. *Cell* **143,** 1047–1058 (2010).
154. Betzig E, Hell SW, Moerner WE (2014) The Nobel Prize in Chemistry 2014. In: Nobelprize.org. http://www.nobelprize.org/nobel_prizes/chemistry/laureates/2014/. Accessed 24 Jan 2015.
155. Dickson, R. M., Cubitt, A. B., Tsien, R. Y. & Moerner, W. E. On/off blinking and switching behaviour of single molecules of green fluorescent protein. *Nature* **388,** 355–358 (1997).
156. Betzig, E. *et al.* Imaging Intracellular Fluorescent Proteins at Nanometer Resolution. *Science (80-.).* **313,** 1642–1645 (2006).
157. Mahou, P., Curry, N., Pinotsi, D., Schierle, K. & Clemens, F. Simulated Emission Depletion microscopy to study amyloid fibril formation. **9331,** 1–10 (2015).
158. Jensen, E. & Crossman, D. J. Technical review: Types of imaging-direct STORM. *Anat. Rec.* **297,** 2227–2231 (2014).
159. Chacko, J. V., Zanacchi, F. C. & Diaspro, A. Probing cytoskeletal structures by coupling optical superresolution and AFM techniques for a correlative approach. *Cytoskeleton* **70,** 729–740 (2013).
160. Van De Linde, S. *et al.* Direct stochastic optical reconstruction microscopy with standard fluorescent probes. *Nat. Protoc.* **6,** 991–1009 (2011).
161. Lee, S.-H., Shin, J. Y., Lee, A. & Bustamante, C. Counting single photoactivatable fluorescent molecules by photoactivated localization microscopy (PALM). *Proc. Natl. Acad. Sci.* (2012).
162. Hell, S. W., Dyba, M. & Jakobs, S. Concepts for nanoscale resolution in fluorescence microscopy. *Curr. Opin. Neurobiol.* **14,** 599–609 (2004).
163. Gustafsson, M. G. L. Surpassing the lateral resolution limit by a factor of two using structured illumination microscopy. *J. Microsc.* **198,** 82–87 (2000).
164. Heintzmann, R. & Cremer, C. G. Laterally modulated excitation microscopy: improvement of resolution by using a diffraction grating. in *Optical Biopsies and Microscopic Techniques III* **3568,** 185–197 (International Society for Optics and Photonics, 1999).
165. Hell, S. W. *et al.* The 2015 super-resolution microscopy roadmap. *J. Phys. D. Appl. Phys.* **48,** (2015).
166. Vicidomini, G. *et al.* Gated CW-STED microscopy: A versatile tool for biological nanometer scale investigation. *Methods* **66,** 124–130 (2014).

167. Lichtman, J. W. & Conchello, J.-A. Fluorescence microscopy. *Nat. Methods* **2,** 910 (2005).
168. Diaspro, A., Chirico, G., Usai, C., Ramoino, P. & Dobrucki, J. Photobleaching. *Handb. Biol. Confocal Microsc.* 690–702 (2006). doi:doi: 10.1007/978-0-387-45524-2_39
169. Hell, S. W. Toward fluorescence nanoscopy. *Nat. Biotechnol.* **21,** 1347–1355 (2003).
170. Willig, K. I., Harke, B., Medda, R. & Hell, S. W. STED microscopy with continuous wave beams. *Nat. Methods* **4,** 915–918 (2007).
171. Vicidomini, G. *et al.* Sharper low-power STED nanoscopy by time gating. *Nat. Methods* **8,** 571–575 (2011).
172. Binnig, G., Rohrer, H., Gerber, C. & Weibel, E. Surface Studies by Scanning Tunneling Microscopy. *Phys. Rev. Lett.* **49,** 57–61 (1982).
173. Binnig, G., Quate, C. F. & Gerber, C. Atomic Force Microscope. *Phys. Rev. Lett.* **56,** 930–933 (1986).
174. Moreno-Flores, S. & Toca-Herrera, J. L. *Hybridizing surface probe microscopies: Toward a full description of the meso-and nanoworlds*. (CRC Press, 2012).
175. Meyer, G. & Amer, N. M. Novel optical approach to atomic force microscopy. *Appl. Phys. Lett.* **53,** 1045–1047 (1988).
176. Meyer, G. & Amer, N. M. Novel optical approach to atomic force microscopy [Appl. Phys. Lett. 5 3, 1045 (1988)]. *Appl. Phys. Lett.* **53,** 2400–2402 (1988).
177. Hutter, J. L., Bechhoefer, J., Hutter, J. L. & Bechhoefer, J. Calibration of atomicforce microscope tips microscope tips. **1868,** (2012).
178. Park, S., Costa, K. D. & Ateshian, G. A. Microscale frictional response of bovine articular cartilage from atomic force microscopy. *J. Biomech.* **37,** 1679–1687 (2004).
179. Martínez, N. F. & García, R. Measuring phase shifts and energy dissipation with amplitude modulation atomic force microscopy. *Nanotechnology* **17,** S167 (2006).
180. Melcher, J. *et al.* Origins of phase contrast in the atomic force microscope in liquids. *Proc. Natl. Acad. Sci.* **106,** 13655–13660 (2009).
181. Cappella, B. & Dietler, G. Force-distance curves by atomic force microscopy. *Surf. Sci. Rep.* **34,** 1–104 (1999).
182. Bizzarri, A. R. & Cannistraro, S. The application of atomic force spectroscopy to the study of biological complexes undergoing a biorecognition process. *Chem. Soc. Rev.* **39,** 734–749 (2010).
183. Zlatanova, J., Lindsay, S. M. & Leuba, S. H. Single molecule force spectroscopy in biology using the atomic force microscope. *Prog. Biophys. Mol. Biol.* **74,** 37–61 (2000).
184. Krotil, H. *et al.* Pulsed force mode: a new method for the investigation of surface properties. *Surf. Interface Anal.* **27,** 336–340 (1999).
185. Diaspro, A. & van Zandvoort, M. A. M. J. *Super-resolution Imaging in Biomedicine*. (CRC press, 2016).
186. Dufrêne, Y. F. *et al.* Imaging modes of atomic force microscopy for application in molecular and cell biology. *Nat. Nanotechnol.* **12,** 295–307 (2017).
187. Kronlage, C., Schäfer-Herte, M., Böning, D., Oberleithner, H. & Fels, J. Feeling for Filaments: Quantification of the Cortical Actin Web in Live Vascular Endothelium. *Biophys. J.* **109,** 687–698 (2015).
188. Moreno Flores, S. & Toca-Herrera, J. L. The new future of scanning probe microscopy: Combining atomic force microscopy with other surface-sensitive techniques, optical microscopy and fluorescence techniques. *Nanoscale* **1,** 40–49 (2009).

189. Brown, A. E. X., Hategan, A., Safer, D., Goldman, Y. E. & Discher, D. E. Cross-correlated TIRF/AFM reveals asymmetric distribution of force-generating heads along self-assembled, ‘synthetic’ myosin filaments. *Biophys. J.* **96,** 1952–1960 (2009).
190. Harke, B., Chacko, J. V., Haschke, H., Canale, C. & Diaspro, A. A novel nanoscopic tool by combining AFM with STED microscopy. *Opt. Nanoscopy* **1,** 1–6 (2012).
191. Chacko, J. V., Canale, C., Harke, B. & Diaspro, A. Sub-Diffraction Nano Manipulation Using STED AFM. *PLoS One* **8,** (2013).
192. Chacko, J. V., Harke, B., Canale, C. & Diaspro, A. Cellular level nanomanipulation using atomic force microscope aided with superresolution imaging. *J. Biomed. Opt.* **19,** 105003 (2014).
193. Whittingham, J. L. *et al.* Insulin at pH 2: Structural analysis of the conditions promoting insulin fibre formation. *J. Mol. Biol.* **318,** 479–490 (2002).
194. Snyder, S. W. *et al.* Amyloid-beta aggregation: selective inhibition of aggregation in mixtures of amyloid with different chain lengths. *Biophys. J.* **67,** 1216–1228 (1994).
195. Gaetano, S. Di *et al.* Recombinant amyloidogenic domain of ApoA-I: Analysis of its fibrillogenic potential. *Biochem. Biophys. Res. Commun.* **351,** 223–228 (2006).
196. Carrotta, R. *et al.* Inhibiting effect of αs1-casein on Aβ1–40 fibrillogenesis. *Biochim. Biophys. Acta - Gen. Subj.* **1820,** 124–132 (2012).
197. Bianchini, P. *et al.* STED nanoscopy: a glimpse into the future. *Cell Tissue Res.* **360,** 143–150 (2015).
198. Bolte, S. & Cordelières, F. P. A guided tour into subcellular colocalization analysis in light microscopy. *J. Microsc.* **224,** 213–32 (2006).
199. Manders, E. M. M., Verbeek, F. J. & Aten, J. A. Measurement of co-localization of objects in dual-colour confocal images. *J. Microsc.* **169,** 375–382 (1993).
200. Costes, S. V. *et al.* Automatic and quantitative measurement of protein-protein colocalization in live cells. *Biophys. J.* **86,** 3993–4003 (2004).
201. D’Amico, M. *et al.* Thioflavin T promotes Aβ (1–40) amyloid fibrils formation. *J. Phys. Chem. Lett.* **3,** 1596–1601 (2012).
202. Manno, M. *et al.* Kinetics of Different Processes in Human Insulin Amyloid Formation. *J. Mol. Biol.* **366,** 258–274 (2007).
203. Xue, W.-F., Homans, S. W. & Radford, S. E. Systematic analysis of nucleation-dependent polymerization reveals new insights into the mechanism of amyloid self-assembly. *Proc. Natl. Acad. Sci.* **105,** 8926–8931 (2008).
204. Mangione, M. R. *et al.* Hsp60, amateur chaperone in amyloid-beta fibrillogenesis. *Biochim. Biophys. Acta - Gen. Subj.* **1860,** 2474–2483 (2016).
205. Calamai, M. *et al.* Reversal of Protein Aggregation Provides Evidence for Multiple Aggregated States. *J. Mol. Biol.* **346,** 603–616 (2005).
206. Kad, N. M. *et al.* Hierarchical Assembly of β2-Microglobulin Amyloid In Vitro Revealed by Atomic Force Microscopy. *J. Mol. Biol.* **330,** 785–797 (2003).
207. Morris, V. J., Kirby, A. R. & Gunning, A. P. *Atomic force microscopy for biologists*. (World Scientific, 1999).
208. Mahou, P. *et al.* Stimulated emission depletion microscopy to study amyloid fibril formation. *Proc. SPIE* **9331,** 93310U (2015).
209. Kaminski Schierle, G. S., Sauer, M. & Kaminski, C. F. Probing Amyloid Aggregation and Morphology In Situ by Multiparameter Imaging and Super-Resolution Fluorescence Microscopy. *Bio-nanoimaging Protein Misfolding Aggreg.* 105–120 (2013). doi:10.1016/B978-0-12-394431-3.00010-9
210. Kaminski, C. F., Pinotsi, D., Michel, C. H. & Schierle, G. S. K. Nanoscale imaging of

neurotoxic proteins. *SPIE Nanosci. Eng.* **9169,** 91690N----91690N (2014).

211. Fornasiero, E. F. & Opazo, F. Super-resolution imaging for cell biologists. *BioEssays* **37,** 436–451 (2015).
212. Apetri, M. M. *et al.* Direct observation of α-synuclein amyloid aggregates in endocytic vesicles of neuroblastoma cells. *PLoS One* **11,** 1–13 (2016).
213. Luitz, M. P. *et al.* Covalent dye attachment influences the dynamics and conformational properties of flexible peptides. *PLoS One* **12,** 1–18 (2017).
214. Hartmann, A., Krainer, G. & Schlierf, M. Different fluorophore labeling strategies and designs affect millisecond kinetics of DNA hairpins. *Molecules* **19,** 13735–13754 (2014).
215. van Ham, T. J. *et al.* Towards Multiparametric Fluorescent Imaging of Amyloid Formation: Studies of a YFP Model of α-Synuclein Aggregation. *J. Mol. Biol.* **395,** 627–642 (2010).
216. ATTO-TEC. Fluorescent Labels and Dyes. *Fluoresc. Labels Dye. Cat.* **49,** 1–45 (2007).
217. Kaminski Schierle, G. S. *et al.* In Situ Measurements of the Formation and Morphology of Intracellular β-Amyloid Fibrils by Super-Resolution Fluorescence Imaging. *J. Am. Chem. Soc.* **133,** 12902–12905 (2011).
218. Braga, P. C. & Ricci, D. *Atomic force microscopy: biomedical methods and applications*. **242,** (Springer Science & Business Media, 2004).
219. Raposo, M., Ferreira, Q. & Ribeiro, P. A Guide for Atomic Force Microscopy Analysis of Soft Condensed Matter. *Mod. Res. Educ. Top. Microsc.* **1,** (2007).
220. Braga, P. C. & Ricci, D. *Atomic force microscopy in biomedical research: methods and protocols*. (Springer, 2011).
221. Bolder, S. G., Sagis, L. M. C., Venema, P. & Van Linden, E. Der. Thioflavin T and birefringence assays to determine the conversion of proteins into fibrils. *Langmuir* **23,** 4144–4147 (2007).
222. Chan, F. T. S., Pinotsi, D., Kaminski Schierle, G. S. & Kaminski, C. F. *Structure-Specific Intrinsic Fluorescence of Protein Amyloids Used to Study their Kinetics of Aggregation*. *Bio-nanoimaging: Protein Misfolding and Aggregation* (Elsevier, 2013). doi:10.1016/B978-0-12-394431-3.00013-4
223. Canale, C., Relini, A. & Gliozzi, A. in *Atomic Force Microscopy in Biomedical Research: Methods and Protocols* (eds. Braga, P. C. & Ricci, D.) 81–95 (Humana Press, 2011). doi:10.1007/978-1-61779-105-5_6
224. Gremer, L. *et al.* Fibril structure of amyloid- b (1 – 42) by cryo – electron microscopy. **119,** 116–119 (2017).
225. Young, L. J., Kaminski Schierle, G. S. & Kaminski, C. F. Imaging Aβ(1–42) fibril elongation reveals strongly polarised growth and growth incompetent states. *Phys. Chem. Chem. Phys.* **19,** 27987–27996 (2017).
226. Schedin-Weiss, S., Caesar, I., Winblad, B., Blom, H. & Tjernberg, L. O. Super-resolution microscopy reveals γ-secretase at both sides of the neuronal synapse. *Acta Neuropathol. Commun.* **4,** 29 (2016).
227. Ries, J. *et al.* Superresolution imaging of amyloid fibrils with binding-activated probes. *ACS Chem. Neurosci.* **4,** 1057–1061 (2013).
228. Pinotsi, D. *et al.* Direct observation of heterogeneous amyloid fibril growth kinetics via two-color super-resolution microscopy. *Nano Lett.* **14,** 339–345 (2014).
229. Ahn, M. *et al.* Analysis of the Native Structure, Stability and Aggregation of Biotinylated Human Lysozyme. *PLoS One* **7,** (2012).
230. Ahmed, S. Nanoscopy of cell architecture: The actin-membrane interface.

Bioarchitecture **1,** 32–38 (2011).

231. Young, L. J., Kaminski Schierle, G. S. & Kaminski, C. Imaging Aβ(1–42) fibril elongation reveals strongly polarised growth and growth incompetent states. *Phys. Chem. Chem. Phys.* **19,** 27987–27996 (2017).
232. Pinotsi, D. *et al.* kinetics via two-color super-resolution microscopy Direct observation of heterogeneous amyloid fibril growth kinetics via two-color super-resolution microscopy. 1–9 (2013).
233. Vestergaard, M. *et al.* Detection of Alzheimer ' s amyloid beta aggregation by capturing molecular trails of individual assemblies. *Biochem. Biophys. Res. Commun.* **377,** 725–728 (2008).
234. O`Brien JS, S. E. L. Lipid composition of the normal human brain. *J. Lipid Res.* **6,** 537–544 (1965).
235. Ashrafuzzaman, M. & Tuszynski, J. A. *Membrane biophysics*. (Springer Science & Business Media, 2012).
236. Kartal, A. *et al.* Analyses of the energy sources used by Turkish referees during ninety minutes soccer match. *Life Sci. J.* **10,** 562–567 (2013).
237. Boesze-battaglia, K. Cell membrane lipid composition and distribution : Implications for cell function and lessons learned from photoreceptors and platelets CELL MEMBRANE LIPID COMPOSITION AND DISTRIBUTION : IMPLICATIONS. **2936,** 2927–2936 (2016).
238. Vance, J. E. & Vance, D. E. *Biochemistry of lipids, lipoproteins and membranes*. (Elsevier, 2008).
239. Singer, S. J. & Nicolson, G. L. The Fluid Mosaic Model of the Structure of Cell Membranes. *Science (80-.).* **175,** 720 LP-731 (1972).
240. Simons, K. & Ikonen, E. Functional rafts in cell membranes. *Nature* **387,** 569–572 (1997).
241. Mayor, S. & Rao, M. Rafts: Scale-dependent, active lipid organization at the cell surface. *Traffic* **5,** 231–240 (2004).
242. Simons, K. & Meers, G. Perspectives in Biochemistry Lipid Sorting in Epithelial Cells. *Biochem. Soc. Trans.* **27,** 6197–6202 (1988).
243. London, E. & Brown, D. A. Insolubility of lipids in Triton X-100: Physical origin and relationship to sphingolipid/cholesterol membrane domains (rafts). *Biochim. Biophys. Acta - Biomembr.* **1508,** 182–195 (2000).
244. Simons, K. & Toomre, D. Lipid rafts and signal transduction. *Nat. Rev. Mol. Cell Biol.* **1,** 31–9 (2000).
245. Pike, L. J. Rafts defined: a report on the Keystone symposium on lipid rafts and cell function. *J. Lipid Res.* **47,** 1597–1598 (2006).
246. Lingwood, D. & Simons, K. Lipid Rafts As a Membrane-Organizing Principle. *Science (80-.).* **327,** 46 LP-50 (2010).
247. Seghezza, S., Dante, S., Diaspro, A. & Canale, C. High resolution nanomechanical characterization of multi-domain model membranes by fast Force Volume. *J. Mol. Recognit.* **28,** 742–750 (2015).
248. Chiantia, S., Kahya, N., Ries, J. & Schwille, P. Effects of ceramide on liquid-ordered domains investigated by simultaneous AFM and FCS. *Biophys. J.* **90,** 4500–4508 (2006).
249. Chiantia, S. *et al.* Role of ceramide in membrane protein organization investigated by combined AFM and FCS. *Biochim. Biophys. Acta - Biomembr.* **1778,** 1356–1364 (2008).

250. Schengrund, C.-L. Lipid rafts: keys to neurodegeneration. *Brain Res. Bull.* **82,** 7–17 (2010).
251. BHATIA, R., LIN, H. A. I. & LAL, R. Fresh and globular amyloid β protein (1–42) induces rapid cellular degeneration: evidence for AβP channel-mediated cellular toxicity. *FASEB J.* **14,** 1233–1243 (2000).
252. Al-Habori, M. Macromolecular crowding and its role as intracellular signalling of cell volume regulation. *Int. J. Biochem. Cell Biol.* **33,** 844–864 (2001).
253. Nilsberth, C. *et al.* The'Arctic'APP mutation (E693G) causes Alzheimer's disease by enhanced Aβ protofibril formation. *Nat. Neurosci.* **4,** 887 (2001).
254. Lashuel, H. A., Hartley, D., Petre, B. M., Walz, T. & Lansbury Jr, P. T. Neurodegenerative disease: amyloid pores from pathogenic mutations. *Nature* **418,** 291 (2002).
255. Novelli, F. *et al.* Supporting information for : Intense THz reveals coupled protein-hydration dielectric response in native and aggregated human lysozyme solutions. 3–8
256. Kourie, J. I. & Henry, C. L. Ion channel formation and membrane-linked pathologies of misfolded hydrophobic proteins: the role of dangerous unchaperoned molecules. *Clin. Exp. Pharmacol. Physiol.* **29,** 741–753 (2002).
257. Hirakura, Y. & Kagan, B. L. Pore formation by beta-2-microglobulin: a mechanism for the pathogenesis of dialysis associated amyloidosis. *Amyloid* **8,** 94–100 (2001).
258. Volles, M. J. & Lansbury, P. T. Vesicle permeabilization by protofibrillar α-synuclein is sensitive to Parkinson's disease-linked mutations and occurs by a pore-like mechanism. *Biochemistry* **41,** 4595–4602 (2002).
259. Dante, S., Hauß, T. & Dencher, N. A. Cholesterol inhibits the insertion of the Alzheimer's peptide Aβ(25–35) in lipid bilayers. *Eur. Biophys. J.* **35,** 523–531 (2006).
260. Kayed, R. *et al.* Permeabilization of lipid bilayers is a common conformation-dependent activity of soluble amyloid oligomers in protein misfolding diseases. *J. Biol. Chem.* **279,** 46363–46366 (2004).
261. Durell, S. R., Guy, H. R., Arispe, N., Rojas, E. & Pollard, H. B. Theoretical models of the ion channel structure of amyloid beta-protein. *Biophys. J.* **67,** 2137–2145 (1994).
262. Kim, H. *et al.* Structural Properties of Pore-Forming Oligomers of α-Synuclein. *J. Am. Chem. Soc.* **131,** 17482–17489 (2009).
263. Kagan, B. L., Azimov, R. & Azimova, R. Amyloid peptide channels. *J. Membr. Biol.* **202,** 1–10 (2004).
264. Chi, E. Y. *et al.* Amyloid-beta fibrillogenesis seeded by interface-induced peptide misfolding and self-assembly. *Biophys. J.* **98,** 2299–2308 (2010).
265. Okada, T., Ikeda, K., Wakabayashi, M., Ogawa, M. & Matsuzaki, K. Formation of Toxic Aβ(1-40) Fibrils on GM1 Ganglioside-Containing Membranes Mimicking Lipid Rafts: Polymorphisms in Aβ(1-40) Fibrils. *J. Mol. Biol.* **382,** 1066–1074 (2008).
266. Laurén, J., Gimbel, D. A., Nygaard, H. B., Gilbert, J. W. & Strittmatter, S. M. Cellular prion protein mediates impairment of synaptic plasticity by amyloid-β oligomers. *Nature* **457,** 1128 (2009).
267. Renner, M. *et al.* Deleterious Effects of Amyloid β Oligomers Acting as an Extracellular Scaffold for mGluR5. *Neuron* **66,** 739–754 (2010).
268. Kremer, J. J., Pallitto, M. M., Sklansky, D. J. & Murphy, R. M. Correlation of β-Amyloid Aggregate Size and Hydrophobicity with Decreased Bilayer Fluidity of Model Membranes. *Biochemistry* **39,** 10309–10318 (2000).
269. Yip, C. M. & McLaurin, J. Amyloid-β peptide assembly: A critical step in fibrillogenesis

and membrane disruption. *Biophys. J.* **80,** 1359–1371 (2001).

270. Ambroggio, E. E. *et al.* Surface behavior and lipid interaction of Alzheimer β-amyloid peptide 1-42: A membrane-disrupting peptide. *Biophys. J.* **88,** 2706–2713 (2005).
271. Kawasaki, T. Structure and Function of Serum Mannan-binding Protein. *Nippon Ishinkin Gakkai Zasshi* **33,** 105–112 (1992).
272. Diao, J. *et al.* Native α-synuclein induces clustering of synaptic-vesicle mimics via binding to phospholipids and synaptobrevin-2/VAMP2. *Elife* **2013,** 1–17 (2013).
273. Burré, J. The synaptic function of α-synuclein. *J. Parkinsons. Dis.* **5,** 699–713 (2015).
274. Ibáñez, P. *et al.* Causal relation between α-synuclein gene duplication and familial Parkinson's disease. *Lancet* **364,** 1169–1171 (2004).
275. Ahn, B. H. *et al.* α-synuclein interacts with phospholipase D isozymes and inhibits pervanadate-induced phospholipase d activation in human embryonic kidney-293 cells. *J. Biol. Chem.* **277,** 12334–12342 (2002).
276. Rodriguez, J. A. *et al.* Structure of the toxic core of α-synuclein from invisible crystals. *Nature* **525,** 486 (2015).
277. Rajagopalan, S. & Andersen, J. K. Alpha synuclein aggregation: Is it the toxic gain of function responsible for neurodegeneration in Parkinson's disease? *Mech. Ageing Dev.* **122,** 1499–1510 (2001).
278. Ahn, M., Kim, S. B., Kang, M., Ryu, Y. & Doohun Kim, T. Chaperone-like activities of α-synuclein: α-Synuclein assists enzyme activities of esterases. *Biochem. Biophys. Res. Commun.* **346,** 1142–1149 (2006).
279. Hoyer, W. *et al.* Dependence of α-synuclein aggregate morphology on solution conditions. *J. Mol. Biol.* **322,** 383–393 (2002).
280. Gaspar, R., Pallbo, J., Weininger, U., Linse, S. & Sparr, E. Ganglioside lipids accelerate α-synuclein amyloid formation. *Biochim. Biophys. Acta - Proteins Proteomics* **1866,** 1062–1072 (2018).
281. Crane, J. M., Kiessling, V. & Tamm, L. K. Measuring lipid asymmetry in planar supported bilayers by fluorescence interference contrast microscopy. *Langmuir* **21,** 1377–1388 (2005).
282. Van Meer, G., Voelker, D. R. & Feigenson, G. W. Membrane lipids: where they are and how they behave. *Nat. Rev. Mol. cell Biol.* **9,** 112 (2008).
283. Mingeot-Leclercq, M.-P., Deleu, M., Brasseur, R. & Dufrêne, Y. F. Atomic force microscopy of supported lipid bilayers. *Nat. Protoc.* **3,** 1654 (2008).
284. Milhiet, P. E., Giocondi, M.-C. & Le Grimellec, C. AFM imaging of lipid domains in model membranes. *Sci. World J.* **3,** 59–74 (2003).
285. Hane, F., Drolle, E., Gaikwad, R., Faught, E. & Leonenko, Z. Amyloid-β aggregation on model lipid membranes: An atomic force microscopy study. *J. Alzheimer's Dis.* **26,** 485–494 (2011).
286. Sheikh, K., Giordani, C., McManus, J. J., Hovgaard, M. B. & Jarvis, S. P. Differing modes of interaction between monomeric Aβ 1–40 peptides and model lipid membranes: An AFM study. *Chem. Phys. Lipids* **165,** 142–150 (2012).
287. Sennvik, K. *A study of b-secretase cleaved Alzheimer amyloid precursor protein*. (Institutionen för klinisk neurovetenskap, arbetsterapi och äldrevårdsforskning (NEUROTEC)/Department of Clinical Neuroscience, Occupational Therapy and Elderly Care Research (NEUROTEC), 2002).
288. Ivanova, M. I., Sievers, S. A., Sawaya, M. R., Wall, J. S. & Eisenberg, D. Molecular basis for insulin fibril assembly. *Proc. Natl. Acad. Sci.* **106,** 18990 LP-18995 (2009).
289. JPK. NanoWizard ® AFM Handbook JPK Instruments NanoWizard ® Handbook

Version 2.2a 1. (2012).

290. Lashuel, H. A., Hartley, D., Petre, B. M., Walz, T. & Lansbury Jr, P. T. Amyloid pores from pathogenic mutations. *Nature* **418,** 291 (2002).